Study of lunar surface chemistry using Swept Charge Devices

by

P. Subramania Athiray
ISRO Satellite Centre, Bangalore
Indian Institute of Astrophysics, Bangalore

A thesis submitted in partial fulfillment for the degree of Doctor of Philosophy to the

Department of Physics
University of Calicut
Calicut, Kerala

May 2015

Certificate

This is to certify that the thesis titled '**Study of lunar surface chemistry using Swept Charge Devices**' is a bonafide record of the work done by P. Subramania Athiray under our joint supervision and that no part of it has been included any where previously for the award of any degree, either in this university or any other institution.

Dr. P. Sreekumar,
Director,
Indian Insitute of Astrophysics,
Bangalore.

Dr. B. R. S. Babu,
Professor,
Department of Physics,
University of Calicut, Kerala.

Declaration of Authorship

I hereby declare that the thesis titled **'Study of lunar surface chemistry using Swept Charge Devices'** is an authentic record of the research work carried out by me under the supervision of Dr. P. Sreekumar, IIA & ISRO Satellite Centre and Prof. B. R. S. Babu, Department of Physics, University of Calicut. No part of this work has formed the basis for award of any other degree or diploma in any university or institution.

P. Subramania Athiray

May 2015

Abstract

The study of origin and evolution of the Moon have generated scientific curiosity for a long time. With the improved technology, with larger telescopes and better scientific instruments the lunar surface got revealed and created more research interests. The surface exploration of Moon gained momentum soon after the samples brought back from the Apollo and Luna missions. Since then, various orbiting remote-sensing experiments explored the lunar surface at multi-wavelengths. This thesis deals with one such study of understanding the chemical composition of the lunar surface using x-rays. This provides a unique opportunity to sample the top few micron thick layer of the lunar surface which undergoes severe modifications and mixing due to different physical/chemical processes.

Context : Since the Apollo era, there have been very few successful observations of the x-ray studies of the lunar surface. Spectral resolution of some of the instruments was badly affected due to charged particles. Chandrayaan-1 X-ray Spectrometer (C1XS) onboard Chandrayaan-1 was launched on October 2008 to study surface elemental abundances with a spatial resolution of 25 km on the lunar surface. C1XS was designed to map the abundances of major rock-forming elements viz., Mg, Al, Si, Ca, Ti and Fe on the lunar surface using the X-ray fluorescence (XRF) technique. C1XS was the first remote sensing x-ray experiment to spectrally resolve the x-ray lines of all major rock-forming elements from the Moon simultaneously under different solar flare conditions. It used 'swept charge devices (SCD)', a variant of x-ray CCDs as detectors.

Description : In this thesis, we present a summary of entire C1XS observations. Steps involved in data selection, spectral analysis procedures viz., x-ray background estimation and modeling incident solar x-ray spectrum for certain flare observations are described in detail. We describe the spectral observations of all major rock-forming elements as seen by C1XS. The first spectral evidence of Sodium (Na) from the Moon as observed by C1XS is demonstrated in the thesis. Elemental abundances are derived from the observed x-ray line intensities.

My thesis work addresses the development of XRF inversion algorithm *x2abundance* for remote-sensing measurements to convert XRF line intensities to abundances with uncertainties. Validation of *x2abundance* using laboratory XRF experiments with metal alloys and lunar analogue rocks are discussed in detail in Chapter 2.

In Chapter 3, we show the spectral analysis of C1XS data, where we extract the XRF line fluxes of major-rock forming elements. We demonstrate the first direct evidence of x-ray signature of Na from the Moon. We determine the abundances of lunar surface elements including Na using *x2abundance*. Results from C1XS abundance analysis exploring the lunar surface geochemistry are discussed in detail in this chapter.

However, global geochemistry of the Moon could not be completely studied by C1XS due to lack of solar x-ray activity and limited mission life-time. Chandrayaan-2 Large Area Soft x-ray Spectrometer (CLASS) is being developed for Chandrayaan-2 to answer the questions raised by C1XS results and complete global mapping with enhanced sensitivity using new generation SCDs (CCD-236).

In fourth chapter, we describe a detailed physical model developed to simulate x-ray photon interaction in SCDs. This Monte Carlo simulation aims at modeling device level interactions to better understand the spectral redistribution function of SCDs. Algorithm of the model, implementation and comparison with C1XS ground calibration data are presented here. This model will be used during the ground calibration of CLASS experiment.

In the last chapter, we summarize the major findings from this thesis work. We discuss the scientific importance of the discovery of Na on the lunar surface. A description on science cases for future lunar surface studies is presented here. Further, to carry out better scientific investigations in future, we propose a few design aspects which can potentially improve the surface exploration of the Moon/airless planetary bodies in x-rays.

Acknowledgements

I would like to thank :

Dr. P. Sreekumar, for all his guidance and support, through not only this research work but my graduate studies as a whole. His continued motivation and encouragement helped me to move forward through the frustrations of research and led me to tackle scientific problems in creative ways. I am much indebted to him for patiently listening and giving solutions to many of my confused personal problems in life.

Prof. B. R. S. Babu, my thesis co-guide at University of Calicut for all the help, support and advice. Special thanks to him for the help in making pellets for rock samples.

Dr. Shyama Narendranath who has been always there to help and support since my early phase of research in ISRO as a project trainee. Special thanks for her collaboration, consistent support and encouragement at various instances.

Dr. Manju Sudhakar, for the collaborative work on Geant4 x-ray fluorescence simulation, which is included in this thesis work. Sincere thanks to her for monitoring the progress of my research and loading me with positive energy.

Mr. Chandra Babu, Mr. Kumar, Mr. Manjunath Olekar, Ms. Mahalakshmi and members of Environment Test Facility, ISAC for their help and assistance to complete XRF experiments. Special thanks to Dr. S. K. Dash, ISAC for his help in EDX studies.

Prof. S. Sanjeevi, from Anna University, for the pulverized Anorthosite sample.

Dr. P. K. Gupta, Dr. G. S. Lodha, Dr. S. K. Deb, Dr. M. K. Tiwari and team members of BL-16 at Raja Ramanna Centre for Advanced Technology, Indore for all their help and support. Special thanks to Dr. Jason and his team at the Open University, UK for all the discussions on SCDs.

My sincere thanks to the Director, Indian Institute of Astrophysics (IIA) for the timely assistance of fellowship, accommodation and availing the facilities at IIA to complete of my PhD. I record my sincere gratitude to the Chair and members of the board of graduate studies and management of IIA for all their help and support. I thank the Head, Department of Physics, University of Calicut and all other faculty members as well as office staff at the department for all the help during this thesis work. I thank the Director, ISAC for the fellowship. Special thanks to Computer & Information Group, ISAC and members of ISAC Library for their help.

I'm thankful to Dr. Anuj & Mr. Ravi BT, who stood with me at various tough instances in the past five years. Tons of thanks to Ravi BT, without his support and encouraging words would not have crossed many scary situations in the past five years. My special thanks to Dr. Debbijoy Bhattacharya and Dr. Sreejith, my seniors, who have always been a good friends for any help and support. Our discussions on science and gossips will remain verdant in my mind.

I'm thankful to Dr. Seetha, Dr. Sankar, Dr. Ramadevi, Dr. Radhakrishna, Dr. Girish, Ms. Vaishali, Ms. Lalita, Dr. Ashoka, Mr. Umapathy, Dr. Anil Agarwal and Ms. Padmavathy for their support and encouragement. I'm thankful to my batch mates Ms. Uma, Ms. Rakhee, Ms. Radhika, Dr. Lalitha and Mr. Vignesh for all the help and motivation. Many thanks to Mr. Nirmal kumar, who is like my brother, with whom I can share all happiness, sorrows and helped me to get over many difficult situations. Special thanks to Mr. Santosh Bharadwaj for his timely help. I thank all my family members and friends at ISRO and IIA for their continued support and motivation as I made my way through graduate school.

I acknowledge the financial help I received from Mr. Krishna Kumar, senior manager, HP and his friends to attend SPIE 2012 international conference. I thank LPI, USRA and NASA for the career development award to attend the LPSC 2014 conference. Participation in these conferences has helped me a lot in completing this thesis.

My sincere gratitude to Mr. Thyagarajan, Ms. Banu, Dr. Viswanathan, Ms. Sudharshana, Chitappa & Chitti for their motivation and belief in my capabilities. Profound thanks to Mr. Srinivasan & Ms. Rama (my in-laws) for their undaunted confidence in me.

I would not have been what I am today, without my parents Mr. Panchapakesan & Ms. Savithri, my brother Mr. Vaidhyanatha Athrey and my patti Ms. Nagalakshmi. I owe every bit my life to their support and unconditional love towards me.

I am ever grateful to my wife Ms. Vaishnavi, who stands beside me, bearing my frustrations and made my life brighter. Completion of this thesis would have been a day dream without her love, support and sacrifice, for which I can't compensate. I can never thank her enough; but this is a start.

I thank my adorable little princess Ms. Avyaktha, whom I miss with my heart and soul.

Contents

List of Figures

List of Tables

Abbreviations

C1XS	**C**handrayaan-1 **X**-ray **S**pectrometer
CLASS	**C**handrayaan-2 **L**arge **A**rea **S**oft x-ray **S**pectrometer
CCD	**C**harge **C**oupled **D**evice
ESA	**E**uropean **S**pace **A**gency
FAS	**F**erroan **A**northosite **S**uite
FOV	**F**ield **O**f **V**iew
FWHM	**F**ull **W**idth at **H**alf **M**aximum
LMO	**L**unar **m**agma **O**cean
LP	**L**unar **P**rospector
LRO	**L**unar **R**econnaissance **O**rbiter
MI	**M**ultiband **I**mager
PIXE	**P**article **I**nduced **X**-ray **E**mission
SCD	**S**wept **C**harge **D**evice
SP	**S**pectral **P**rofiler
SRF	**S**prectral **R**edistribution **F**unction
XRF	**X**-**R**ay **F**luorescence

Chapter 1

Introduction

Scientific evidences lead to the insight that the Universe originated from the Big Bang $\approx$ 13.8 billion years ago, and primarily composed of H, D, He & Li. The rest of the elements are synthesized in stars through innumerable nuclear reactions. These elements are ejected out during the explosive end stages of stars which fill the interstellar medium. It is from these 'cosmic recycling bins' of dust and dense molecular clouds that the birth of next generation stars and planetary systems occur via gravitational collapse. Our solar system with the Sun, eight planets, numerous satellites, dwarf planets, asteroids and comets originated nearly 4.6 billion years ago, from one such collapse. Since their formation, these objects evolved continuously under different physical and chemical environments. Various models of planetary formation and evolution have been developed based on studies of planetary surfaces, planetary atmospheres, meteorites and comets. Further supporting evidences are obtained from the astronomical observations of gas disks (both circumstellar disks & protoplanetary disks) and star forming regions. However, the picture is still far from complete. In spite of all materials originating from the gas and dust in the disk around the young Sun, we see a wide diversity among the planets and satellites in terms of their composition, atmosphere and magnetosphere. Refractory group elements ie., metals & silicates - with relatively high equilibrium condensation temperatures, coalesced to form metal & rocky-rich entities in the inner solar system, whilst the outer solar system was formed with metal-poor large gaseous planets. A detailed study of solar system objects will reveal the inventory of elements and

geochemical processes that occurred in the past during the evolution. Remotely sensing the spectral signatures of planets help in understanding these processes. Further, the exploration of solar system objects is considered as a yardstick to understand the increasing list of exo-planetary systems discovered from various dedicated missions like Kepler, CoRoT and many other ground-based observations.

Though, with the advent of technology, our journey in the exploration of solar system has matured from flyby space missions to orbiting and landing space missions, remote sensing of planetary bodies is still carried out across the complete electromagnetic spectrum using different sensors as well as particle detectors (charged and neutral). These studies helped us in further understanding of the physical and chemical makeup of planetary bodies however, it has also raised many new questions about the formation and evolution.

1.1 Study of Moon - Scientific rationale

The Moon being our nearest celestial object has been the central source of interest for several decades. The surface of the Moon is of prime scientific importance as it is very ancient; more than 3 billion years old. The lunar surface preserves record of early geological history of its formation which all the inner or terrestrial planets have lost during their evolution. Space technology and exploration has seen a big boom since the launch of lunar flyby missions by the Soviet Union and the United States of America during 1950-1960s. Several space missions were sent to the Moon by multiple space agencies across the globe which opened up a new view of our Moon. It is believed that the Moon formed from a molten magma was chemically homogeneous at the time of formation [*Longstaff*, 2014; *Elkins-Tanton*, 2006]. Later, elemental fractionation occurred, when the mantle was developed with high dense materials deep inside the Moon and low dense materials formed the outer crust.

The regions on the Moon that appear dark to naked eye were once thought to be lakes filled with water and hence named as ‘Maria’ (Latin origin). Today, we know that they are lava deposits with high Fe & Ti content which absorb more light radiation and hence

they appear dark. The Maria regions are less cratered smooth surfaces with basalt compositions and occupy only 15% of the Moon's surface. The bright regions are called 'the highland terrane', which are heavily cratered and ancient. They form the lunar crust with high Al & Ca content whose high reflectivity makes it bright.

Meteoritic impacts cover the lunar crust with fine pulverized bedrock and soil which is called 'Lunar regolith'. Frequent impacts in the early phase of the Moon resulted in an increase in the thickness of regolith from a few centimeter to a meter. As a result many small impacts that occurred later on the Moon altered only the top layers of regolith. Hence, surface compositions can exhibit variations and could possibly contain material of extra-lunar origin, rocks that emplace from the interior of the Moon during major impacts. Samples brought back from nine locations near the equatorial region of the Moon through manned and robotic missions viz., Apollo and Luna, were analyzed in laboratories for deriving chemical compositions. Global database of lunar meteorites which are considered to be of lunar origin based on isotope ratios is constantly getting updated every year. compositions. However, the area sampled is a tiny fraction of the entire area of the Moon. Remote sensing experiments provide the best opportunity to study the global compositional diversity of the Moon.

1.1.1 Lunar surface : Status of current understanding

Surface composition and morphological features cause differences in the lunar albedo. The highly reflective highlands ages about 4.56-4.29 by; while the alkali suites show younger ages 4.37-3.80 by [*Jaumann et al.*, 2012]. One of the major hypothesis based on the Apollo samples were that the highland rocks are considered to be ferroan anorthosites and are depleted in volatile elements such as sodium. The concept of a dry Moon with depletion of volatile elements was changed completely by the indication of water observations over polar regions by Clementine and Lunar Prospector [*Nozette et al.*, 1996; *Feldman et al.*, 1998]. Strong absorption features around $\approx$ 2.9 μm attributed to hydrated (OH^{-}/H_2O bearing) minerals were detected recently by M^3 instrument onboard Chandrayaan-1 [*Pieters et al.*, 2009]. These observations likely indicate hydration processes on the lunar surface through interaction of solar-wind protons on the

oxygen-rich lunar rocks produced during micrometeorite impacts. Direct and indirect evidences of sodic-rich lithologies are found from Chandrayaan-1 (C1XS) [*Athiray et al.*, 2014] and LRO (Diviner) [*Greenhagen et al.*, 2010; *Kusuma et al.*, 2012]. Recent results from China's Chang'E-2 (CE-2) x-ray spectrometer shows the surface elemental abundances in the Oceanus Procellarum region which exhibit differences from the earlier Lunar Prospector GRS results. Also the derived abundances of Fe from CE-2 are larger than the averages of lunar mare samples brought back from Apollo and Luna missions [*Ban et al.*, 2014].

The heterogeneity in the lunar crustal chemical composition and distinct variations between nearside and farside geochemistry shows the complexity involved in the evolution of the Moon. In order to understand the geochemical history of the Moon completely, further studies on compositional diversity with sophisticated instruments are needed. The Chandrayaan-1 X-ray Spectrometer (C1XS) was designed to provide global abundance maps of major rock-forming elements on the lunar surface through X-ray Fluorescence (XRF) remote sensing technique. In this thesis we deal with the following:

- Spectral analysis of C1XS data and determination of lunar surface chemistry.
- Development and validation of XRF inversion algorithm to convert the XRF line flux to elemental abundances, for C1XS analysis using laboratory experiments.
- Development and validation of charge transport model for the Swept Charge Devices, x-ray sensors used in C1XS and to be used in the upcoming Chandrayaan-2 Large Area Soft x-ray Spectrometer (CLASS) for global mapping of surface chemistry.

We start this chapter by explaining various theories on the origin of the Moon. We outline different scientific techniques by which the surface of the Moon has been studied so far and describe the importance of surface chemistry. Current status on lunar elemental mapping and its scientific significance are discussed. At the end of this chapter, we present a detailed discussion on the fundamentals of XRF spectroscopic analysis which will be relevant for the following chapter.

1.2 Theories on the formation of the Moon

The Earth-Moon system is very peculiar in many aspects in our solar system. To date the Moon is the only big natural rocky satellite in the solar system. The moons of Mars viz., Phobos & Deimos are thought to be captured asteroids. Satellites of outer planets are mostly ice-rock mixtures. The Earth-Moon system has the largest satellite-planet mass ratio as given in Table 1.1. Compared to all other planets, the Earth-Moon system is spinning rapidly and hence has high angular momentum (3.5×10^{-41} rad g cm^{-2} s^{-1}). The orbit of Moon is neither in the plane of Earth's equator nor in the ecliptic plane, but inclined at 5°to the latter. The observed moment of inertia (0.3931 ± 0.0002 kg m^2) [*Hartmann & Davis*, 1975] clearly suggests absence of a dense core at the center of the Moon. Geochemical analysis of lunar samples show similarities in the isotopic abundance ratios of Oxygen (O^{16}, O^{17}, O^{18}) between the Earth and the Moon (see Fig. 1.1). Isotope ratios of other elements viz., Tungsten [*Touboul et al.*, 2007], Silicon [*Fitoussi & Bourdon*, 2012], Chromium [*Lugmair & Shukolyukov*, 1998] on the Moon also match well with the Earth's composition. Hence, a good model for lunar origin should explain the following :

- Age of the Moon as measured precisely from the lunar returned samples.
- Low FeO content as reflected in the average density of the Moon.
- Angular momentum of the Earth-Moon system
- Lack of volatiles and enrichment in refractory elements (such as Al & Ca) as measured in the returned samples.
- Isotopic compositions as that of the Earth.

During pre-Apollo era, various theories were proposed by planetary scientists for the formation of the Moon [*Wood*, 1986]: **(i)** *The Moon was formed along with the Earth from the same accretion disk of dust called* **Co-accretion hypothesis (ii)** *The early wandering Moon was captured by the Earth's gravity known as* **Capture hypothesis (iii)** *Due to fast rotation of proto-Earth, blobs of material were thrown out into space which condensed*

TABLE 1.1: Mass ratios of satellite and their host planet for some solar system bodies (Combined masses of all known satellites are included)

Name of the Planet	Satellite-planet mass ratio
Earth	0.0123
Mars	2.0×10^{-8}
Jupiter	0.00021
Saturn	0.00025
Uranus	0.00011
Neptune	0.00021

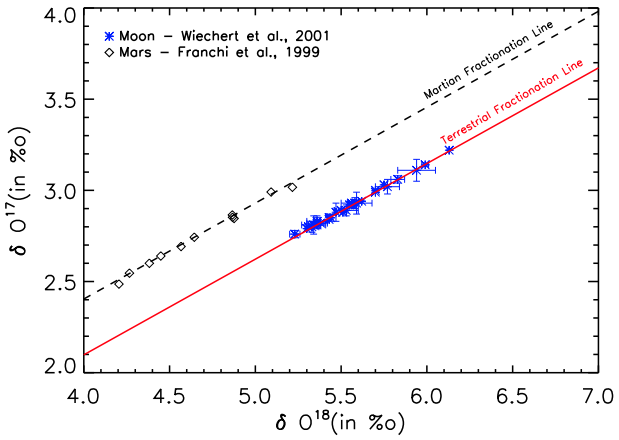

FIGURE 1.1: Plot showing the three oxygen isotope plots of lunar rocks and its indistinguishable match with Earth's composition [*Wiechert et al.*, 2001]. Composition of Martian meteorites [*Franchi et al.*, 1999] are also shown for comparison.

into the Moon called **Fission hypothesis**. All these hypothesis have some limitations. Some could not match the age of the Moon determined precisely from the Apollo rocks and some could not explain the large angular momentum of the Earth-Moon system. Presently, the most accepted model for the formation of the Moon is the theory of **Giant Impact Hypothesis** formulated by [*Hartmann & Davis*, 1975] and further developed by [*Cameron & Ward*, 1976].

1.2.1 Giant Impact Hypothesis

Giant impact hypothesis suggests an oblique collision of a large Mars-sized object, Theia (with masses $\approx$ 0.10 - 0.15 $M_{\oplus}$) on the proto-Earth at a velocity of $\approx$ 5 km s^{-1} [*Canup*, 2004a]. As a result, huge amount of material from the Earth's mantle and the impactor

were ejected into space. The spewed material coalesced under the action of gravity to form the Moon. Large amount of energy was liberated due to the collision which melted the Moon completely: This is called the Lunar Magma Ocean (LMO) phase. Our understanding of the lunar surface is based on the LMO theory [*Taylor*, 1982; *Warren*, 1985] where elemental fractionation occurred during the cooling phase of the magma and is supported by the results of analysis of lunar samples with ferroan anorthosites collected from a small area on the nearside highland region of the Moon. Key points of this theory which support some of the distinct features of the Moon are :

- The impact kinetic energy could have caused depletion of almost all volatile elements on the Moon.
- The angular momentum of the Earth-Moon system is an outcome of the giant energetic collision which occurred $\approx$ 4.5 b.y. ago.
- Magma with more mafic minerals (high Mg & Fe content) formed the mantle which is enriched in higher density minerals like pyroxene and olivine.
- Low density Al-rich minerals (plagioclase feldspar) crystallized to form the topmost layer of the Moon at the end stages of cooling of the magma ocean.

This hypothesis successfully explains the basic differences in the chemical composition of the highland and mare regions on the Moon. The highland crust was formed during the end stages of global magma ocean with flotation of the melt and crystallization of plagioclase feldspar. Later volcanic intrusions from deep layers of the Moon produced Mare basalt regions which exhibit mantle composition.

Making of the Moon from a single giant-impact scenario has been supported by numerous three-dimensional Smoothed Particle Hydrodynamics (SPH) numerical simulations [*Benz et al.*, 1986, 1987, 1989; *Melosh & Kipp*, 1989; *Cameron & Benz*, 1991; *Canup & Asphaug*, 2001]. The impact scenario was well modeled with an assumption of a non-rotating impactor and proto-Earth target by *Canup* [2004b]; while later SPH simulations explored the effects of pre-impact rotation on the formation of the Moon [*Canup*, 2008]. However, numerical simulations of standard impact model predicts the lunar disc to be

predominantly made up of the impactor material ($> 60\%$), which was formed elsewhere in the solar system. Unlike in lunar samples, the isotope ratios of O in Martian meteorites and Chondrite samples do not match with Earth's isotopic compositions (see Fig. 1.1). This shows that in general the elemental isotopic compositions vary across the solar system. If the Moon thus formed from Theia, as predicted by the numerical simulations, the isotopic compositions of the Moon and the Earth are expected to be different. As the standard giant impact could not reconcile the isotopic similarities, other new models are proposed recently using extensive numerical simulations which are aimed to reduce this discrepancy. A short note on those models are summarized in the following section.

1.2.2 Recent models on formation of the Moon

- In *Pahlevan & Stevenson* [2007] model, an impact was proposed along with turbulent mixing and diffusion in the vaporized molten disk and the proto-Earth to produce a homogeneous Earth-Moon system. However, this model requires a large timescale to achieve equilibrium between the proto-Earth and the debris disk, by which the disk would collapse.

- Another model by *Ćuk & Stewart* [2012], proposes collision of a fast rotating early Earth (2-3 hrs a day) with an impactor of ≈ 0.005 $M_{\oplus}$, smaller than what was used in the standard giant impact. Instabilities that arise due to impact on the fast rotating proto-Earth would fling out enough material from the Earth's mantle to form a chemically similar Moon as shown in Fig. 1.2(b). However, the resultant Earth-Moon system will be left with a larger angular momentum than what has been observed. In order to shed the excess angular momentum, the impact has to be followed by evection resonance, where the Moon transfers the angular momentum to the Sun in multiple orbits around the Earth.

- A model by *Canup* [2012] suggests a low velocity collision of an Earth-sized large impactor (larger than the Mars-sized one used in standard impact model) with the proto-Earth. As a result of complete mixing, it forms the Moon with isotopic compositional similarities as that of the Earth. This scenario is shown in Fig. 1.2(c)

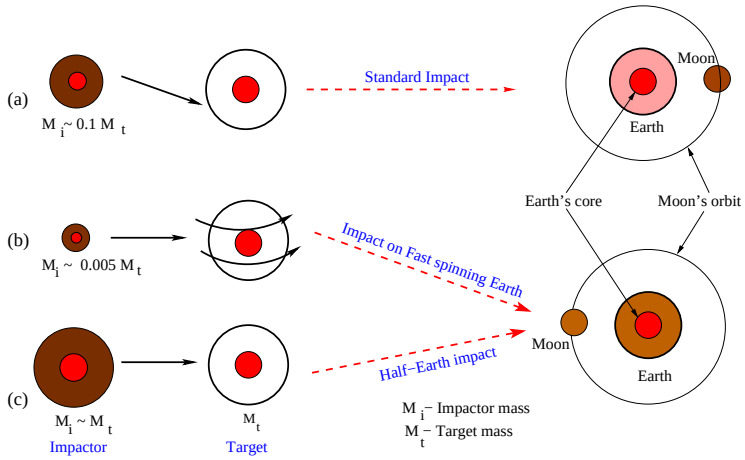

FIGURE 1.2: Different impact models for the formation of the Moon. (a) Standard giant impact which produce chemically dissimilar Earth-Moon system (b) Impact on a rapidly rotating Earth model by *Ćuk & Stewart* [2012] (c) Collision of Earth-sized object on proto-Earth model by *Canup* [2012].

Both the models by *Ćuk & Stewart* [2012] and *Canup* [2012] produce a chemically similar Moon as that of the Earth and also reproduce the angular momentum of the Earth-Moon system. However, assumptions in the chemistry of impactor could have serious implications to reflect the compositional variations [*Canup*, 2013].

Rocks of Theia found in Apollo samples - Recent results : A set of fresh Apollo samples were analyzed very recently using advanced mass spectrometric analysis methods for isotopic compositions [*Pack & Herwartz*, 2014]. Surprisingly, the isotope ratios of O viz., $\frac{O^{17}}{O^{16}}$ and $\frac{O^{18}}{O^{16}}$ (which were known to be indistinguishable with respect to the Earth [*Wiechert et al.*, 2001]) in the Apollo samples differ significantly from the Earth by 12 ppm. The result ratifies the formation of the Moon via a giant impact. Further, the composition of Theia is also speculated to be of Enstatite chondrite [1] [*Herwartz et al.*, 2014].

As seen from the above, results from precise chemical analysis of lunar samples provide valuable input for the models that address the origin of the Moon. New results from these precise measurements clearly show the chemical heterogeneity of the Moon. However, the lunar returned samples do not provide a global picture of the Moon as they

[1] A rare form of meteorite classified as E-chondrite which are known to have formed under reduced conditions (poor FeO content) in comparison to other chondrites [*Lodders & Fegley*, 2011]

reflect limited sampling regions. Thus, the study of global lunar surface geochemistry using remote sensing techniques is required to test various theories of Moon formation. Geochemical and mineralogical studies of the lunar surface in multi-wavelengths can better constrain the theories and models of lunar evolution.

1.3 Role of lunar surface chemistry studies

The study of lunar surface chemistry can address some of the outstanding questions which are listed below :

- How did the Moon evolve?
- What was the true chemical composition of the Moon and how are the elements distributed on the lunar surface?
- Was it homogeneous initially?
- What is the thermal history of the Moon?
- What geochemical processes differentiate Moon's crust from its inner layers?
- What causes the chemical heterogeneity?

Space-based remote sensing measurements can enrich our knowledge with a global view of lunar surface chemistry compared to localized findings from landing sites. Even after more than five decades of lunar space exploration, many scientific questions regarding the formation and evolution of the Moon remain unanswered. From decades of lunar studies, today we know that global elemental fractionation occurred in the Moon with the crust, mantle and core having distinct chemical compositions. Concentration of major-elements ($>$ 1 wt%), minor-elements ($<$ 1 wt%), trace-elements (in ppm and ppb) and isotopic ratios are available for variety of lunar-returned materials. On the Moon, most of the elements are present in the form of minerals and rocks. Minerals result from geological processes on crystalline solids. Common minerals observed on the

lunar surface are given in Table 1.2. Investigations of recent observations by Moon Mineralogical Mapper (M^3) payload on Chandrayaan-1 found Mg-rich Spinel on the lunar surface [*Pieters et al.*, 2011]. Lunar rocks are igneous (directly cooled from molten state of magma) in nature and are assemblages of different minerals which can be classified as follows :

TABLE 1.2: List of common minerals on the Moon

Plagioclase	**Pyroxene**	**Olivine**	**Ilmenite**
Anorthite: $CaAl_2Si_2O_8$	Orthopyroxene: $(Mg,Fe)_2Si_2O_6$	Fayalite: Fe_2SiO_4	$FeTiO_3$
Albite: $NaAlSi_3O_8$	Clinopyroxene: $(Ca,Mg,Fe)_2Si_2O_6$	Forsterite: Mg_2SiO_4	

- **Ferroan Anorthosite suites (FAS)** : These rocks contain $>$ 90% plagioclase mineral content. They are quantified by 'Anorthite number (An#)' defined as $\frac{Ca}{Ca+Na+K}$ in moles. Global mineral maps from Clementine revealed the distribution of anorthite rocks on the Moon with an average spatial resolution of 200 m [*Lucey*, 2004]. Global distribution of Pure Anorthosite (PAN)[2] rocks on the lunar surface was mapped by Kaguya with a spatial resolution of 20m (visible) and 62 (IR) [*Ohtake et al.*, 2009]. These results support the LMO theory. However, these instruments did not possess broad wavelength range to measure the complete diversity in plagioclase.

- **Magnesian suite** : Mg suite rocks are characterized with Magnesian number (Mg#) defined as $\frac{Mg}{Mg+Fe}$ in moles. They appear to have been produced from a magma which is rich in incompatible elements (ie., elements left behind without fitting into the any crystal structure of major minerals). These rocks are believed to be later intrusions into the highland crust. Global distribution of An# and Mg# is essential in understanding the crustal compositional variations of the Moon.

- **Alkali suites** : These rocks are less abundant but show distinction due to their high alkali content. However the distribution and their origin are still not known completely.

[2] characterized with high anorthite content (An_{93} and above)

- **KREEP basalts** (**P**otassium, **R**are **E**arth **E**lements, **P**hosphorous) : Basalts formed from igneous melts which are enriched in incompatible trace elements.

The present lunar surface has been bombarded by many impacts with bodies ranging from few mm to km-sized meteorites which have reworked the top crust. Thus the study of lunar surface chemistry with the following global measurements can help to better understand the geochemical evolution of the Moon.

- Global map of the plagioclase feldspar using Anorthite number (An#) - to study diversity of plagioclase feldspar for surface processes and thermal evolution.
- Global mapping of Mg suite rocks to understand the process of volcanic intrusions of partial melted magma
- Global mapping of the concentration of lunar volatiles

These measurements can be used as test cases to validate the predictions of the existing LMO theory. In the following section, we present various techniques that are used in space-based remote sensing experiments to decipher the surface chemistry of the Moon.

1.4 Remote sensing surface chemistry mapping techniques

1.4.1 Mineral mapping

Methods to study lunar chemical elements is generally grouped according to their associations with major types of minerals as different elements undergo various geochemical processes.

Reflectance spectroscopy: Surface mineralogy is performed using the visible & near-IR (0.4 μm - 3 μm), mid-IR (7 μm - 25 μm) and UV (0.001 μm - 0.4 μm) wavelength bands which measure the spectral reflectance. The reflected solar radiation contains absorption features which identifies minerals present on the surface. Electronic transitions between the split orbital energy levels in transition elements (Ni, Cr, Co, Fe, etc) lead

to diagnostic absorption features centered at different wavelengths which distinguish the minerals and hence used for mapping. Absorption features can also arise from transitions between vibrational levels of asymmetric molecules (for example water-bearing minerals at $\approx$ 3.10 μm).

Thermal IR spectroscopy: Lunar observations at mid-IR wavelengths mostly arise from thermal emission radiation processes. In silicate minerals, when the refractive index approaches unity (same as the refractive index of vacuum ie., 1), reflectance minimum occurs between 7.5 μm and 9 μm which is called the 'Christiansen Feature' [*Pieters*, 1999]. Reflectance minimum means maximum emission (Emission = 1 - Reflectance) and hence the emitted mid-IR radiation peaks around 8 μm. Ca-rich feldspathic anorthite exhibit CF positions around 7.84 μm whereas plagioclase with Na component shift towards lower CF values $\leq$ 7.8 μm [*Donaldson Hanna et al.*, 2014]. This helps in identifying the diversity of mineral plagioclase. Ultramafic minerals viz., pyroxene and olivine exhibit intermediate CF (around 8.2 μm) and long CF values (around 8.9 μm).

Diversity in the chemical composition of the Moon is mostly addressed using these proxy lunar mineral maps. List of successful remote sensing experiments which provided high resolution global lunar mineral maps are listed in Table 1.3.

TABLE 1.3: List of successful lunar missions which provided global mineral maps of the Moon

Mission name	**Instrument name**	**Wavelength range (in μm)**
Clementine	UV-VIS camera	0.3 - 1.0
	Near-IR Camera	0.9 - 3.1
Kaguya	Spectral Profiler	0.5 - 2.6
	Multiband Imager	0.415 - 1.55
Chandrayaan-1	Hyper Spectral Imager	0.4 - 0.95
	Moon Mineralogical Mapper (M^3)	0.7 - 3.0
Lunar Reconnaissance Orbiter	Diviner Radiometer	0.3 - 400

1.4.2 Element mapping

Remote sensing via gamma-ray and x-ray spectroscopy provide the capacity to do direct chemical mapping of the Moon, but are limited by the amount and quality of data.

Gamma-ray spectroscopy : There are two ways by which gamma-rays are produced on the Moon (i) *interaction of high energy cosmic rays with the nuclei of rock-forming elements via inelastic scattering or neutron capture process yielding gamma-rays [*Metzger*, 1993]* (ii) *Natural gamma-ray emission from radioactive elements such as K (^{40}K - 1.46 MeV), U (^{235}U - 1.76 MeV) and Th (^{232}Th - 2.62 MeV) [*Lawrence et al.*, 1998;* Prettyman et al.*, 2006]*. The observed gamma-ray line intensities are proportional to the elemental concentration. Following are the factors that affect conversion of gamma-ray line intensities to elemental abundances :

- The intensity of gamma-ray lines is highly dependent on neutron production as the interaction of cosmic ray protons with nuclei of rock-forming elements yield neutrons which in-turn produce gamma-ray photons. In order to derive precise elemental abundances, gamma-ray spectrometer data needs complementary data from neutron spectrometer. The strong dependency of gamma-ray line intensities on neutron production as well as changes in the lunar subsurface neutron flux [*Yamashita et al.*, 2008] makes the conversion indirect and complex.
- The process of thermal neutron capture gets affected by the amount of solar wind hydrogen implanted on the lunar soil. Increase in thermal neutron capture increases the gamma-ray line flux and hence affects the abundances.
- Gamma-ray data exhibit a complex and highly uncertain background arising from various sources [*Prettyman et al.*, 2006; *Zhang liyan et al.*, 2012].

X-ray spectroscopy : Sun is the primary source for lunar x-ray excitations. When solar x-ray photons impinge on the Moon they interact via two modes which are :

1. **X-ray Fluorescence**: If the energy of the incident photon is greater than the binding energy of an atomic shell, an electron will be ejected by the photoelectric

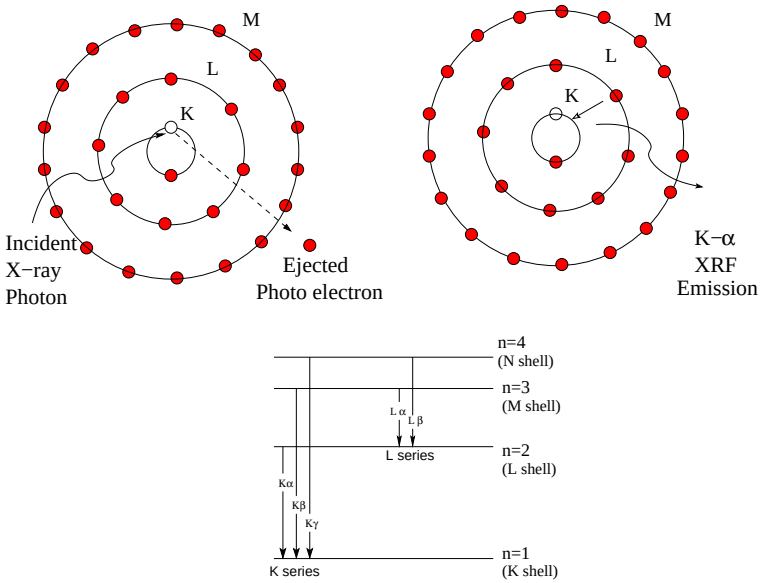

FIGURE 1.3: Principle of X-ray Fluorescence (XRF)

effect. The vacancy thus created is then filled by an electron from a higher shell. This electron transition results in the emission of an x-ray photon called x-ray fluorescence, of energy characteristic of the atom. A sketch of XRF principle is shown in Fig. 1.3. Since the atomic energy levels of each element in the periodic table are distinct and quantized, the XRF emission from atoms can be used to directly identify the presence of elements.

2. **X-ray Scattering**: Interaction of incident x-ray photons with bound atomic electrons without any transfer of energy to the electron is called Rayleigh or Coherent scattering. Incoherent or Compton scattering occurs at high x-ray energies (100s of keV) where the incident photon loses energy to a free electron of the atom during interaction. Soft x-ray photons (1 - 10 keV) from solar corona interact with major rock-forming elements on the Moon primarily via XRF and coherent scattering. While the scattered flux depend weakly on the target composition, the scattered x-rays do not directly provide information on lunar chemistry.

    - **Particle Induced X-ray Emission (PIXE)**: Apart from solar x-rays, cosmic ray charged particles and energetic charged particles from the Sun during eruptive events can interact with the surface elements on the Moon and create vacancy similar to the x-ray excitation process. As an outcome of filling the

inner shell electron vacancy, characteristic x-rays are emitted. This process is efficient only during periods of high flux of charged particles with a narrow energy range in the MeV region (say 1 - 4 MeV for protons) which is due to their high absorption cross-sections. XRS onboard MESSENGER spacecraft observed PIXE from the surface of Mercury during dark side observations and derived the elemental compositions [*Starr et al.*, 2012].

1.4.3 Scientific importance of elemental mapping

- Elemental mapping of the Moon provides the compositional differences in the major crustal terrains which is important in understanding early lunar crust and mantle evolution. Mare regions represent lunar mantle compositions from a depth of 200 - 500 km, whereas highlands represent the end phase of flotation and crystallization of plagioclase. Global elemental maps for mare and highland regions can better constrain and validate models of lunar origin and evolution.

- Determination of Mg and Fe abundances and their relative proportion is important as they form primary major rock-forming minerals. Global mapping of Mg# as mentioned in sec.(1.3), is a vital parameter to understand the evolution of the early lunar crust. Pristine lunar minerals/rocks will exhibit high Mg# in comparison to evolved rocks. Earlier attempts to map Mg# using Clementine multispectral and Lunar Prospector Gamma-ray Spectrometer (LP GRS) data, did not answer many scientific questions due to lack of precision.

- Studying the variation of plagioclase on lunar surface by mapping An# can uncover the end stages of magma ocean. Global measurement of moderately volatile elements, which can be locked in minerals (for eg., intermediate plagioclase will contain the moderately volatile sodium), can address the effect of thermal cooling and secondary processing on the lunar surface. Studying various possible reservoirs of sodium on the surface can address the volatile inventory on the Moon.

1.5 Status of lunar surface element mapping

Since Apollo, several lunar missions carried x-ray and gamma-ray experiments to map elemental abundances. Unfortunately, even today a unified cross-calibrated elemental map does not exist.

1.5.1 Gamma-ray elemental maps

Lunar Prospector - Global abundance maps of Fe, Ti and other radio-active elements are available as a direct measure from the Gamma Ray Spectrometer (GRS) onboard Lunar Prospector (LP). Using data from GRS along with neutron spectrometer data onboard LP, global abundance maps of light weight rock-forming elements are obtained indirectly [*Prettyman et al.*, 2006]. However, at certain regions on the Moon, the abundance of Fe determined from GRS does not agree with Clementine spectral reflectance measurements [*Lawrence et al.*, 2002].
Kaguya - Global maps of certain radioactive elements are made available from Kaguya GRS. Recently, global distribution of Ca abundance on the Moon has been obtained from the GRS data onboard Kaguya [*Yamashita et al.*, 2012]. However, it is to be noted that Kaguya did not carry neutron spectrometer to assist GRS data.

Furthermore, the accuracy of abundances from GRS data is limited by the highly uncertain background and quality of fundamental nuclear data [*Yamashita et al.*, 2008; *Zhang liyan et al.*, 2012]. Also, in order to derive reliable elemental abundances, gamma-ray data demand complementary information from a neutron spectrometer.

1.5.2 X-ray elemental maps

Apollo 15 & 16 - X-ray spectrometer (XRS) on Apollo 15 & 16 covered only 10% [*Clark*, 1979] of the area on the equatorial region on the nearside of the Moon and estimated relative abundances, with respect to Si. They used gas-filled proportional counter detectors and detected only Mg, Al, Si from the Moon. The results clearly showed distinct

compositional variations between mare and Highland regions based on Mg/Si and Al/Si ratios.

SMART-1 - D-CIXS (Demonstration of a Compact Imaging X-ray Spectrometer) experiment [*Grande et al.,* 2003] onboard SMART-1 used solid state x-ray detectors and measured various elements from Ca up to Fe during bright solar flares for the first time. However, enroute to the Moon the detectors suffered severe radiation damage which constrained meaningful quantitative analysis.

Kaguya - XRS onboard Kaguya [*Shirai et al.*, 2008; *Okada et al.*, 2009] which used solid state x-ray detectors and carried standard calibration samples to determine surface elemental chemistry, also suffered from radiation damage which degraded the spectral capability of the detectors significantly.

Thus, there are no measured absolute elemental abundances from any earlier x-ray experiments.

Chandrayaan-1 - C1XS [*Howe et al.*, 2009; *Grande et al.*, 2009] onboard Chandrayaan-1 was equipped with Al doors which protected its solid state x-ray detectors from radiation damage due to charged particles enroute to the Moon. Unlike the SMART-1 mission, Chandrayaan-1 spent significantly less time in the Earth's radiation belt enroute to the Moon. It reached and observed the Moon without losing much of its high spectral capability. Due to lack of intense solar flares and limited mission life, it could not produce global elemental maps of the Moon. Nevertheless, simultaneous observation of major rock-forming elements were carried out during a few flares that occurred during its operational phase. Also, for the first time this study showed the direct detection of x-ray signature of Sodium (Na) from the lunar surface. Details of remote sensing XRF studies are explained in the following section.

1.6 Remote sensing using XRF spectroscopy

Remote sensing XRF spectroscopy has a long history in studying the chemical composition of the lunar surface (for example, *Apollo 15 (1971), Apollo 16 (1972), Smart-1 (2003), Kaguya (2007), Change-1 (2007) and Chandrayaan-1 (2008) for the Moon, Near*

Earth Asteroid Rendezvous (NEAR) (1996) for the asteroid Eros, HAYABUSA (2003) for the asteroid 25143 Itokawa).

1.6.1 Solar x-rays

Surface temperature of the Sun is $\approx$ 6000 K, which implies that the resulting black-body emission is most intense at visible wavelengths and the flux of quiescent x-rays emitted from the photosphere is low. The solar corona is hot (a few million degrees) and can act as a low-intensity source of x-rays. At times, the Sun releases energy explosively, when magnetic configurations rearrange in the chromosphere and/or corona in order to reduce the energy stored in magnetic fields. The excess energy released often leads to the acceleration of charged particles. Accelerated electrons from the outer layer of the Sun strike the cool gas atoms in its photosphere and emit radiation in x-rays via primarily bremsstrahlung process. These events are referred to as "solar flares", where the emission of x-rays increases suddenly, reaches a maximum and decays over a time scale of a few minutes to some hours. Solar flares are classified based on the amount of peak x-ray flux reaching the Earth as measured by the x-ray detectors (1 - 8 Å) in GOES [3] spacecrafts. They are termed as A, B, C, M and X class with increasing intensity (see Table 1.4 for details), each class being ten times more intense than the previous. XRF

TABLE 1.4: Classification of solar flares based on the soft x-ray flux (1 - 8 Å band) received by the GOES satellite

Class	**X-ray Flux (W/m^2)**
A	$< 10^{-8}$
B	10^{-7} to 10^{-6}
C	10^{-6} to 10^{-5}
M	10^{-5} to 10^{-4}
X	$> 10^{-4}$

remote sensing provides an unambiguous and unique identification of signals from the major elements (>1 wt%). Interaction of soft x-rays (1 - 10 keV) are limited only to the top few tens of microns of the lunar surface in contrast to centimeter-depth observations

[3] Geostationary Operational Environmental Satellite operated by NASA for space-weather monitoring

by gamma-rays. Thus, x-ray remote sensing offers the best opportunity to study the composition of lunar regolith which can be different from the bulk lunar composition. It also provides an independent measure of elemental abundances which can be compared with abundances derived from other spectral techniques.

1.6.2 Quantitative XRF analysis

In quantitative analysis, the measured XRF line intensities are converted to corresponding elemental abundances. However, conversion of the XRF line intensities to elemental abundances is not straight forward as the observed line intensity depends on many factors which are explained below:

- The incident spectrum $I_o(E)$: XRF line intensities of different elements vary significantly with respect to the x-ray spectrum exciting the surface. For example, during weak flares with fewer x-ray photons at high energies, XRF lines of high atomic number elements say Ti, Fe from the lunar surface may not be seen/strongly detected in the observed spectrum. Hence a hard, intense input spectrum across the energy range of 1 - 10 keV, exciting all the elements on the surface is the ideal condition.

- Matrix effects M(S,E): Planetary surfaces are intrinsically compositionally inhomogeneous. The presence of an element on the surface can either enhance or reduce the x-ray line flux of other element(s), thus influencing the relative spectral intensities of XRF lines. This is called the *Matrix effect* (see Fig. 1.4).

- Particle size : In regions where the mean particle size forming the surface is larger than the mean penetration depth of x-rays, particle size affects the XRF line intensity.

- Geometry of observation: Incident angle (ϕ) - Angle between incidence angle of solar x-rays and lunar surface normal, Phase angle(θ) - Angle between the Sun, Moon and detector. Observational geometry keeps on changing due to orbital motion of the spacecraft around the Moon.

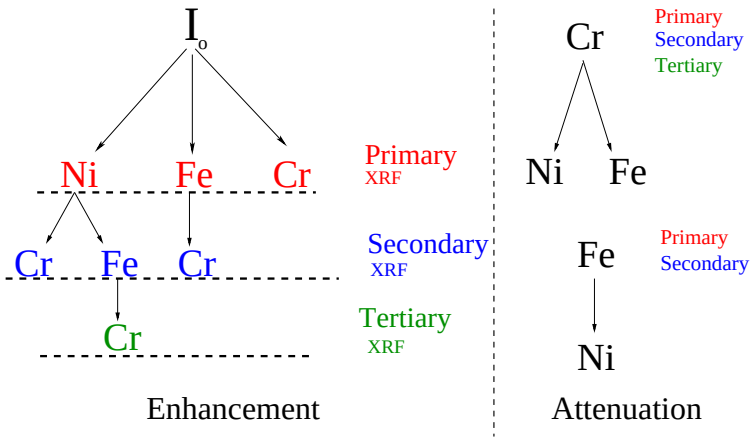

Symbol	Atomic No.	Kα (keV)	Kβ (keV)
Ni	28	7.477	8.264
Fe	26	6.403	7.057
Cr	24	5.414	5.946

FIGURE 1.4: Illustration of the *Matrix effect* in a 3-element sample (Ni, Fe, Cr). *Enhancement :* Incident x-ray photons (I_o) excite all the three elements and produce its respective fluorescence (both K_α and K_β) called **Primary XRF**. Primary Ni XRF lines can excite the lower atomic number elements Fe and Cr. Similarly Fe primary XRF lines can excite Cr which are all collectively termed as **Secondary XRF**. Secondary Fe XRF lines produced by primary Ni XRF lines in turn produces **Tertiary XRF** of Cr. *Attenuation :* XRF lines of Cr can be attenuated by the presence of Ni & Fe atoms, as it does not posses enough energy to excite their K-shell electrons and hence does not help in x-ray identification of elements. Similarly, the line intensity of Fe can be attenuated when it encounters a Ni atom enroute to the detector.

- X-ray background B(E): Background spectrum of x-ray detector needs to be characterized as the XRF lines ride over the background spectrum.

All the aforesaid dependencies are to be taken into consideration to derive precise elemental abundances from XRF line intensities. Further complexities involved in space-based XRF studies along with an algorithm developed for remote sensing XRF studies to derive elemental abundances from C1XS data are explained in Chapter 2.

1.7 Summary

Remote sensing XRF technique provides direct estimation of major elemental abundances on the lunar surface. As explained in this chapter, global elemental abundances are derived from the conversion of measured XRF line intensities, which is quite complex for remote sensing XRF studies. We have developed an XRF inversion code, *x2abundance* for C1XS analysis. In this thesis, we present the algorithm of *x2abundance* and its validation through laboratory XRF experiments. Comprehensive analysis of entire C1XS observations during solar flare periods, to derive lunar surface elemental abundances are presented. We report the first direct observation and estimation of sodium (Na) abundance from the Moon. The derived Na abundance is larger than what was expected. With an eye towards improving capability to do full global mapping, we present the charge transport model for SCD and its validation using C1XS ground calibration data. This model will be very helpful to understand the device level interaction and simulate spectral response at low energy x-rays to meet the scientific objectives of the upcoming experiment CLASS onboard Chandrayaan-2.

Chapter 2

XRF Inversion code for remote sensing application

In chapter 1, we introduced lunar surface chemistry and explained how x-ray spectroscopy can be used for lunar surfaced studies. In this chapter we describe the algorithm and development of a XRF inversion code named 'x2abundance' to convert the observed x-ray line intensities from remote sensing observations into elemental abundances. The code is used to determine lunar surface elemental abundances from C1XS observations. Various XRF experiments (both laboratory and simulation) performed on different samples for the validation of x2abundance are also explained in this chapter.

2.1 Comparison of laboratory and space-based XRF experiments

XRF spectroscopy is a well-established, non-destructive multi-elemental analysis technique where abundances are derived from the observed XRF line intensities. Multiple dependencies of x-ray line intensities, as explained in chapter 1, complicate the conversion of line intensities to elemental abundances. Numerous algorithms are available for quantification of laboratory-based XRF experiments [*Jenkins et al.*, 1995]. However,

space-based XRF experiments suffer from several additional constraints which are listed below :

- Unlike laboratory experiments where the energy spectrum of incident x-ray photons exciting sample is known and stable, x-rays from solar flares are unpredictable, extremely dynamic and exhibit spectral variability in short-intervals of time (seconds). Hence the observed XRF spectral line intensities can also exhibit large time-dependent variations independent of changes in the chemical composition of ground pixels.
- *Matrix effect* explained in earlier chapter (refer Sec. 1.6.2) becomes very complex.
- Unlike laboratory samples, the size distribution of soil particles is not well characterized on planetary surfaces.
- Geometry of the experiment (viz., angle of incidence, observation angle, spot-size, location of spot-size, etc) can be fixed and known to a greater accuracy in laboratory experiments which is not the case for space-based XRF experiments due to continuous motion of the spacecraft in the orbit and changing relative position of the Sun.
- Unlike laboratory experiments where sources contributing to the x-ray background are well characterized and fully accounted for. In space experiments, modeling of x-ray background is difficult since background varies significantly with time and orbital phase. This is discussed further in chapter 3.

Hence it is essential to develop an algorithm which can account for some of these effects to derive accurate elemental composition from remote-sensing x-ray observations. Using the analytical equations of the Fundamental Parameter (FP) approach [*Criss & Birks*, 1968; *Rousseau & Boivin*, 1998], we have developed an XRF inversion algorithm for the analysis of data from C1XS. The codes are written in Interactive Data Language (IDL).

2.2 Quantification methods

Standard methods for laboratory XRF experiments in deducing the composition of a sample are well known [*Jenkins et al.*, 1995]. Among the XRF quantification methods, the fundamental parameter (FP) approach is unique. It is considered as 'standard-less' approach in deriving the sample composition. It uses the knowledge of incident spectrum I_o(E) exciting the sample and relies on fundamental equations describing the characteristic x-ray intensity of atoms in a flat and homogeneous sample. Uncertainties in the fundamental data, such as mass absorption coefficient (μ_E), fluorescent yield (ω) and jump-ratios of different elements, together determine the accuracy of this approach. The first analytical formulation of XRF emission incorporating the matrix effects was given by *Sherman* [1955] and further modified by *Shiraiwa & Fujino* [1966]. The need for matrix correction was clearly demonstrated by the experiments with ternary alloys [*Shiraiwa & Fujino*, 1967].

The earliest space-based XRF experiments invoked the concept of flux ratios through which the relative abundances of Mg and Al with respect to Si (reference element) were estimated. In the Apollo 15 and 16 experiments [*Adler et al.*, 1972, 1973b,a], the abundance of Si was considered to be invariant throughout the lunar surface and Al/Si and Mg/Si ratios were estimated. This approach demands a precise knowledge of the reference element and yields only relative abundances. The veracity of derived abundances thus depends on the assumed uniformity of the reference element. Analysis of XRS data from NASA's Near-Earth Asteroid Rendezvous (NEAR) - Shoemaker mission used calibration curves (ie., photon count ratios vs elemental concentration ratios) obtained for some of the measured meteorite compositions for different solar spectra and observing conditions [*Nittler et al.*, 2001]. Furthermore, the effect of heterogeneity was also considered in deriving the surface elemental composition of asteroid Eros. *Weider et al.* [2012] assumed a fixed Si abundance and modeled the abundances of other elements relative to it wherein they used the algorithm developed by [*SMART-1 Team et al.*, 2009; *Swinyard et al.*, 2010] for D-CIXS. Also, iterations were performed around the initial rock composition with each line emission optimized one at a time. In contrast, in our

method, XRF computations are performed where the weight percentages of all the observed elements are allowed to vary together over a large range. No assumptions on the weight percentage of elements are made except for the unobserved/weakly detected lines. Hence the derived abundances are expected to better reflect the true composition.

2.3 XRF inversion algorithm *x2abundance*

We now describe the formulation of the XRF inversion algorithm *x2abundance* which converts the observed XRF line intensities to elemental abundances. The algorithm uses analytical expressions of FP method which assumes a thick, homogeneous and flat sample. Expressions of *Shiraiwa & Fujino* [1966], given in Eqns. (2.1, 2.2 and 2.3) are used for the computation of XRF line intensities from the sample. Various steps involved in *x2abundance* in deriving the elemental abundances are explained below. The sequence of execution of some of the important steps in the program is summarized in Fig. 2.1. As the major elemental chemistry of the lunar surface involves elements whose XRF line energies are in the range of (0.1 - 10 keV), only elements with K-shell atomic binding energies less than 10 keV, are considered for computation. Using fundamental atomic data such as mass absorption coefficient, fluorescence yield, etc., the code computes intensity of XRF lines analytically for a given matrix (M_j), incident spectrum ($I_o(E)$) and observational geometry.

$$I_1(ip) = \frac{1}{sin\ \psi}\int_{E_{be}^i}^{E_{max}} \frac{Q_{ip}(E)I_o(E)dE}{\mu(E)cosec\ \phi + \mu(E_i)cosec\ \psi} \tag{2.1}$$

$$\begin{aligned} I_2(ip) &= \frac{1}{2sin\ \psi}\sum\nolimits_{jq}\int_{E_{be}^j}^{E_{max}} \frac{Q_{jq}(E)Q_{ip}(jq)I_o(E)}{\mu(E)cosec\ \phi + \mu(E_i)cosec\ \psi} \\ &\times\left\{\frac{sin\ \psi}{\mu(ip)}log\left[1+\frac{\mu(ip)cosec\ \psi}{\mu(jq)}\right] + \frac{sin\ \phi}{\mu E}log\left[1+\frac{\mu Ecosec\ \phi}{\mu)(jq)}\right]\right\}dE \end{aligned} \tag{2.2}$$

$$
\begin{aligned}
I_3(ip) \;=\; & \frac{1}{4sin\ \psi}\int_{E_{be}^{k}}^{E_{max}} \sum_{kr}\sum_{jq} \frac{Q_{kr}(E)Q_{jq}(kr)Q_{ip}(jq)I_o(E)}{A(E)+D(ip)} \\
& \times\Bigg[\frac{1}{A^2(E)}\ log\ \frac{B(kr)+A(E)}{B(kr)}\ log\ \frac{C(jq)+A(E)}{C(jq)} \\
& +\frac{1}{A(E)D(ip)}\ log\ \frac{B(kr)+A(E)}{B(kr)}\ log\ \frac{C(jq)+D(ip)}{C(jq)} \\
& +\frac{1}{D^2(ip)}\ log\ \frac{B(kr)+D(ip)}{B(kr)}\ log\ \frac{C(jq)+C(ip)}{C(jq)} \\
& +\left(\frac{1}{A(E)}+\frac{1}{D(ip)}\right)\left(\frac{1}{C(jq)}\ log\ \frac{B(kr)+D(ip)}{B(kr)}+\frac{1}{B(kr)}\ log\ \frac{B(kr)+C(jq)}{C(jq)}\right) \\
& -\frac{1}{A(E)}\int_{0}^{B(kr)/C(jq)} \frac{1}{A(E)t+B(kr)}\ log\ \frac{1+t}{t}\ dt \\
& -\frac{1}{D(ip)}\int_{0}^{C(jq)/B(kr)} \frac{1}{D(ip)t+C(jq)}\ log\ \frac{1+t}{t}\ dt\Bigg] dE
\end{aligned}
\tag{2.3}
$$

$$
\begin{aligned}
A(E) &= \frac{1}{sin\ \phi}\mu(E) && ; \quad Q_{kr}(E) = \mu_k(E)W_k\omega_k R_r^k K_k \\
B(kr) &= \mu(kr) && ; \quad Q_{jq}(kr) = \mu_j(kr)W_j\omega_j R_q^j K_j \\
C(jq) &= \mu(jq) && ; \quad Q_{ip}(jq) = \mu_i(jq)W_i\omega_i R_p^i K_i \\
D(ip) &= \frac{1}{sin\ \psi}\mu(ip) && ; \quad Q_{ip}(E) = \mu_i(E)W_i\omega_i R_p^i K_i
\end{aligned}
$$

where μ - mass absorption coefficient (cm^2/g); ϕ - incident angle; ψ - emission angle; Q - fluorescence probability for measured line from an element; W - weight fraction; ω - fluorescence yield; K - K-edge jump ratio; R - K-α transition probability.

2.3.1 X-ray Line flux and flux-fraction

We define a Flux-fraction (FF_i) for each element as the ratio of its line flux to the sum of line flux of all elements seen in the spectrum which is represented as:

$$
(FF_i)_T = \frac{(F_i)_T}{\sum_{i=1}^{n}(F_i)_T} \tag{2.4}
$$

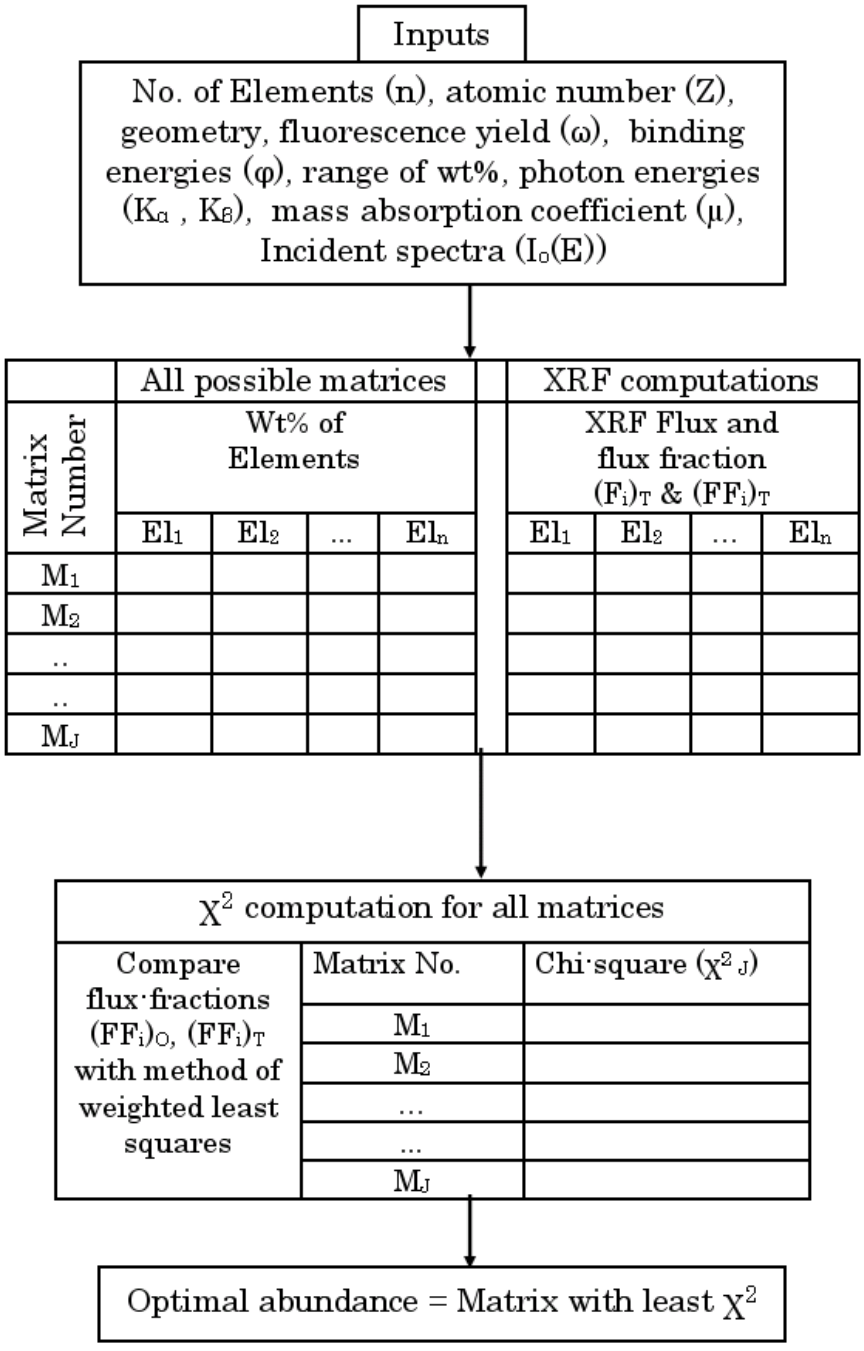

FIGURE 2.1: Important steps involved in the execution sequence of *x2abundance*

where i runs from 1 to number of elements 'n' in the sample, $(F_i)_T$ - computed x-ray line flux of i^{th} element, $(FF_i)_T$ - computed flux fraction of i^{th} element. Spectral fits to the observed XRF data provide the observed line flux $(F_i)_O$. Similar to Eq. (2.4), we also define the observed flux fraction of elements $(FF_i)_O$ using $(F_i)_O$. The error in the observed flux fraction $\sigma_{(FF_i)_O}$ in each element is computed by propagating errors in the observed x-ray line flux of each element $\sigma_{(F_i)_O}$ using error propagation techniques [*Bevington & Robinson*, 2003].

2.3.2 Matrix generation & XRF computation

Qualitative analysis of XRF spectrum identifies the list of elements present in the sample. A set of observed elements with different weight percentages is referred to here as the 'matrix'. We generate different sets of possible combinations of weight percentages (wt%) for the set of elements under consideration. In each matrix, the sum of percentages of weights are maintained at 100% [ie., for a matrix M_j ($\sum W_i$ =100% where W_i is the percentage of weight of each element)]. For samples with large number of elements, suitable constraints on the range of elemental weight percentages based on an a-priori knowledge helps in reducing the number of matrices and hence the number of iterations. For example, if the abundance of an element is known to be more than 60% in a four element sample, its weight percentages will be allowed to vary between 60% and 99%. The remaining three elements put together can vary only between 1% and 40% which reduces the number of possible matrices and hence limits computation. The program computes line flux $(F_i)_T$ and flux-fraction $(FF_i)_T$ for all elements in each matrix (M_j). Table 2.1 lists the fundamental parameters used in *x2abundance* along with the relevant references.

2.3.3 Deriving abundances

To derive elemental abundances, the observed flux-fractions $(\mathrm{FF}_i)_O$ are compared with the computed flux-fractions $(\mathrm{FF}_i)_T$ for all elements in each matrix. Of the generated matrices spanning a range of weight percentage combinations of elements, the best

TABLE 2.1: List of fundamental parameters used in *x2abundance*.

Parameter	Reference
Mass absorption coefficient (μ)	NIST [a] database
Fluorescence yield (ω)	[*Markowicz*, 2002] (Appendix VI)
Jump ratios	[*Markowicz*, 2002] (Chapter 1 (Eq. 51))
K line transition probability	[*Markowicz*, 2002] (Chapter 1 (Eq. 23))

[a] www.nist.gov/pml/data/xracoef/index.cfm

suite matrix is selected by the method of Weighted Least Squares [*Press et al.*, 1988]. A χ_j^2 value is defined as:

$$\chi_j^2 = \sum_{i=1}^{n} \frac{[(FF_i)_O - (FF_i)_T]^2}{[\sigma_{(FF_i)_O}]^2} \tag{2.5}$$

The matrix with abundance values, yielding the lowest (χ_j^2) value is chosen as the best fit to the true abundance.

2.3.4 Deriving abundance errors

Uncertainties in the observed flux-fraction of elements $\sigma_{(FF_i)_O}$ are used to estimate the uncertainties in predicted elemental abundances. The computed flux-fraction of each element $(FF_i)_T$ corresponding to the matrix with the lowest χ_j^2 is allowed to vary within the observed error limits ($2 \times \sigma_{(FF_i)_O}$). The matrices corresponding to the upper and lower limits of flux-fractions give the 2σ error in the predicted abundances. If the error in the predicted abundance of an element is less than the wt% step size, then the step size is considered as the error in the abundance of that element.

2.4 XRF experiments

The algorithm described in sec.(2.3) takes into account some of the dependency factors of XRF intensity in deriving the elemental abundances. In order to validate the inversion algorithm and understand the effect of dependency factors in determining the elemental abundances, we performed two modes of controlled XRF experiments :

1. Laboratory XRF experiments
2. Geant4 XRF Simulations

2.4.1 Laboratory experiments to address *x2abundance* validation

Metal alloys (Fe & Ni based) and lunar analogue rocks were employed as samples for laboratory experiments. Samples were chosen to contain major elements with characteristic x-ray energies up to 10 keV. Composition of standard metal alloys (Fe & Ni based) are readily available with high accuracy and can be used under atmospheric conditions to observe statistically significant XRF spectrum. To investigate matrix effect and test the robustness of inversion algorithm, we conducted experiments on metal alloys as well as on lunar analogue rocks ($10 < Z < 30$) which needed vacuum environment. Continuum spectrum from a x-ray tube and mono-energetic spectrum from a synchrotron x-ray beam (Indus 2 - beamline 16) were used for sample excitation. Further details of the experiments are summarized in Table 2.2. True composition of all the samples were obtained from Energy Dispersive X-ray analysis (EDX) facility at ISRO Satellite Centre (ISAC) using an Oxford Instruments INCA Penta FETx3 system on a scanning electron microscope. Accelerated electrons are allowed to hit the sample to give out characteristic x-rays which are detected using a cryo-cooled high sensitive x-ray detector. Measurements are made under high vacuum conditions and the system can measure elements up to C whose K-α is around 0.4 keV. Before carrying out EDX analysis on actual samples, calibration was carried out on standard samples (Co, Cu, Ni etc.,) provided by the manufacturer. EDX estimates the true abundances to within 0.5%.

2.4.1.1 Experiment setup

Geometry of the experimental setup used in the present studies is shown in Fig. 2.2 with the incident and emission angles defined. Lunar analogue samples were irradiated using a high intensity mono-energetic synchrotron x-ray beam at the Indus 2 synchrotron facility. A collimated x-ray beam of energy 8 keV and size $\approx$ 1mm $\times$ 1mm was used for sample excitation with the detector kept at a distance of $\approx$ 10cm from the sample. In

order to observe low energy x-rays from low Z elements like Mg, Al etc., measurements were carried out inside a vacuum chamber made out of stainless steel (SS-304) with base pressure of $\approx 10^{-2}$ mbar. Metal alloy samples were irradiated using an x-ray generator (MiniX) with Ag anode operated at 10 kV and 15 μA. The thick target bremsstrahlung [*Kramers*, 1923] x-ray spectrum (I_o(E)) with Ag 'L' emission lines and continuum exciting metal alloys, measured by Si-PIN detector is shown in Fig. 2.3. However, it may be pointed out that the distribution of x-rays from solar flares, exciting the lunar surface is mostly represented by a thermal continuum along with many emission lines that dominate at soft x-rays ($<$ 8 keV), which also exhibit spectral variability in time. Under such circumstances, the effect of surface roughness and grain size coupled with observational geometry on XRF line strength becomes important, which are not currently addressed in this work.

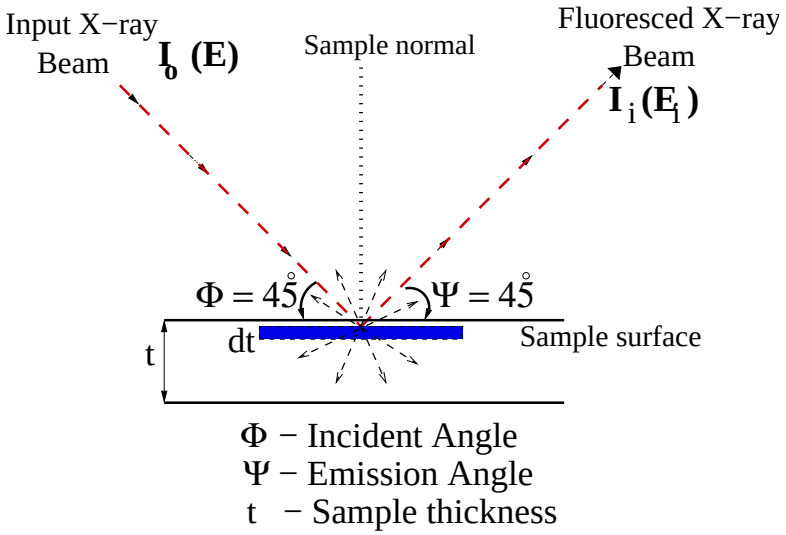

FIGURE 2.2: Schematic view of laboratory XRF experiment

2.4.1.2 Sample description

Table 2.3 lists the samples used in the laboratory experiment along with the major elements seen in their XRF spectra. A brief description on the samples used is given below:

TABLE 2.2: Laboratory XRF experiment details

Sample category	**Experiment station**	**Input x-ray Source**	**Input x-ray Energy**	**Detector**
Metal Alloys	Environment Test Facility (ETF) at ISAC	Amptek Mini-X	2 - 10keV continuum	Amptek Si-PIN XR-100CR
Lunar Analogue rocks	XRF -μ probe beam-line (BL-16) at RRCAT, Indore	Synchrotron x-ray beam	Mono-energetic 8 keV	Amptek Si-PIN XR-100CR

TABLE 2.3: Details of samples used for validation of x2abundance

S.No.	Laboratory samples with major elements	Geant4 samples with major elements
1	Indian 10 rupee coin *(Ni, Cu)*	Basalt *(Fe, Ti, Ca, Si, Al, Mg, O)*
2	British 1$\mathcal{L}$ coin *(Ni, Cu, Zn)*	Icelandic Basalt *(Fe, Ti, Ca, Si, Al, Mg, Na, O)*
3	Inconel 600 *(Cr, Fe, Ni)*	User defined sample1 *(Fe, Ti, Ca, Si, Al, Mg, O)*
4	Incoloy DS *(Cr, Fe, Ni)*	User defined sample2 *(Fe, Ca, Si, Al, Mg, Na, O)*
5	Cast Monel *(Mn, Fe, Ni, Cu)*	
6	Monel 400 *(Mn, Fe, Ni, Cu)*	
7	Lunar simulant (JSC-1A) *(O, Na, Mg, Al, Si, Ca, Ti, Fe)*	
8	Sittampundi pulverized rock *(O, Al, Si, Ca, Ti, Fe)*	

Metal alloys : Standard alloys of Nickel containing major elements between Cr to Zn whose characteristic x-ray peaks fall between $\approx$ 5.4 and 10.0 keV were used.

Lunar analogue rocks : Two samples which closely represent the composition of lunar mare and highland region were used.

- Lunar Simulant (JSC-1A) : JSC-1A is a lunar mare regolith simulant released by NASA for research studies mined from a commercial cinder quarry at Merriam

Crater (35° 20' N, 111° 17' W). [1] The volcanic ash deposit of Merriam crater is basaltic in composition, similar to the soil from Maria terrain of the Moon, which are believe to be the partial melts of lunar interior erupted on the surface. The mined ash was processed to produce the simulant with mean grain size of $\approx$ 190 μm. A complete characterization of lunar simulant (JSC-1A) is reported in *Ray et al.* [2010].

- Sittampundi rock : This sample is taken from the anorthositic rocks available at Sittampundi (near Salem, TN), India, which are considered near-equivalent to lunar highland rocks [*Anbazhagan et al.*, 2012] in composition. As mentioned in chapter 1, it is believed that the lunar highland terrane formed as the lighter mineral plagioclase feldspar ($CaAl_2Si_2O_8$) floated and crystallized on the surface during the end stages of the lunar magma ocean phase. Pure calcic-anorthite and labradorite are the dominant minerals in this sample. The sample exhibits a low mafic content and large concentration of Al and Ca. They are pulverized to a grain size of about 100 μm or smaller. Detailed studies on the rocks of this site are reported in [*Anbazhagan et al.*, 2012; *Aarthy et al.*, 2009].

Pellets of these samples were made after crushing them manually and compressing it with a pelletizer. We assume that the pellets are a close representation of flat and homogeneous sample based on the SEM image of the pellets.

2.4.1.3 XRF spectral analysis

The observed XRF spectra of laboratory samples were analyzed using the x-ray spectral analysis package (XSPEC) [*Arnaud*, 1996]. XRF lines of major elements forming the samples are clearly seen in the spectra. The best spectral fit obtained for all the samples is shown in Fig. 2.4(a-b), 2.5(a-b) and 2.6(a-b), where XRF lines were modeled. The observed elements are labeled with respective symbols. X-ray signature of Mg was not seen in the spectrum of JSC-1A due to poor efficiency of the detector system at lower

[1] A volcanic cinder cone located in the San Francisco volcano field near Flagstaff, Arizona.

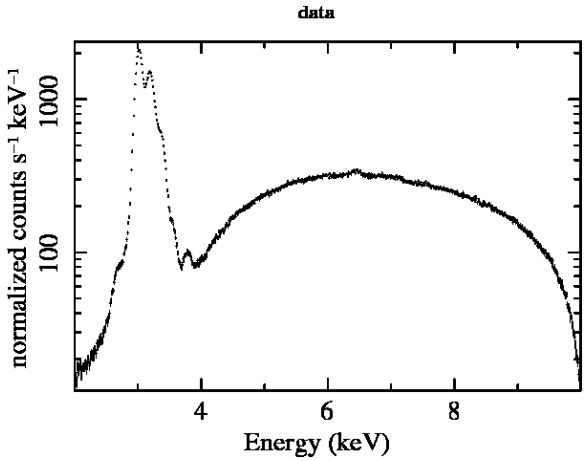

FIGURE 2.3: Incident x-ray spectrum of MiniX (x-ray generator) as measured with a Si-PIN detector (with 1mil thick Be window). Figure shows the x-ray continuum along with L-shell excitation lines of Ag anode (2.98 keV, 3.15 keV, 3.35 keV, 3.5 keV) measured at the sample's position.

energies around 1 keV due to Be window and also a less probability in exciting the relatively lower abundant element, Mg by the 8 keV beam.

Spectral components & corrections : Next to photoelectric absorption process producing XRF line emission, elastic scattering process has the next higher probability of interaction. Rayleigh scattering component was negligible for metal alloy samples as it occurs mostly at low energies [*Fernndez*, 1992], where the incident spectrum (ref. Fig. 2.3) did not have adequate flux. Spectra of lunar analogue samples contain scattered incident x-ray beam (both Rayleigh & Compton scatter) along with XRF lines of stainless steel arising from the vacuum chamber walls. Lines from stainless steel arise due to the interaction of uncollimated scattered 8 keV beam with the walls of the vacuum chamber. XRF spectrum of SS-304 excited by an 8 keV beam was simulated in Geant4 to account for the contamination. Using known composition, both elastic and inelastic scattered components were also simulated in Geant4. Table models[2]) compatible for XSPEC analysis were generated using the XRF spectrum of SS-304 and scatter component spectra (elastic and inelastic). Apart from these components, lunar analogue samples also contain many trace elements (in ppm) which are mostly high Z elements (For JSC-1A ex.

[2]Table Model - A model in XSPEC can also be defined as a two column table (energy versus photon intensity at some specified binning) as opposed to an analytical form. The final model spectrum is calculated by interpolation across the bins.

Ni, Zr, Sr, Ce, Ba etc.,). Emission lines of SS-304 and trace elements were fitted with Gaussian functions along with other spectral components which are all labeled in Fig. 2.4 (trace elements are vertically written).

Apart from these factors, a tiny fraction of contamination was expected due to scattering of these lines from the perspex holder. To account for the contamination by unseen trace elements and perspex scattering, XRF line fluxes were considered to have an intrinsic uncertainty of 2% (a conservative estimate derived from Geant4 simulation with perspex). Observed XRF line fluxes of the samples thus derived were corrected for potential contamination. Flux-fractions were computed using Eq. (2.4) from the observed flux and fed to *x2abundance* along with the respective input spectrum.

2.4.2 Geant4 XRF experiments

Geant4 is a Monte Carlo based toolkit to simulate the interaction of photons and particles through matter [*Agostinelli et al.*, 2003]. It incorporates various physics interactions, event tracking system, user-defined geometries, digitization etc., and covers a wide range of energies of interaction (say 250eV to TeV energies) from optical to γ-rays and charged particles. It allows the user to define the experimental geometry, sample formulation and simulate the fundamental physical processes. Geant4 (ver. 9.4) simulations were performed invoking electromagnetic physics processes which include XRF and x-ray scattering (both elastic & inelastic). Geometry of the experiment was included to emulate the one used in the laboratory experiment, in order to cross validate the results of *x2abundance* from laboratory experiments. XRF simulations were performed on the set of samples listed in Table 2.3. XRF line fluxes of all elements obtained from Geant4 simulation were assumed to have Poisson errors (ie., $\sqrt{Counts}$). Flux-fractions were computed using Eq. (2.4), which along with incident spectrum served as input to *x2abundance*. Results of XRF experiments are summarized in the following section.

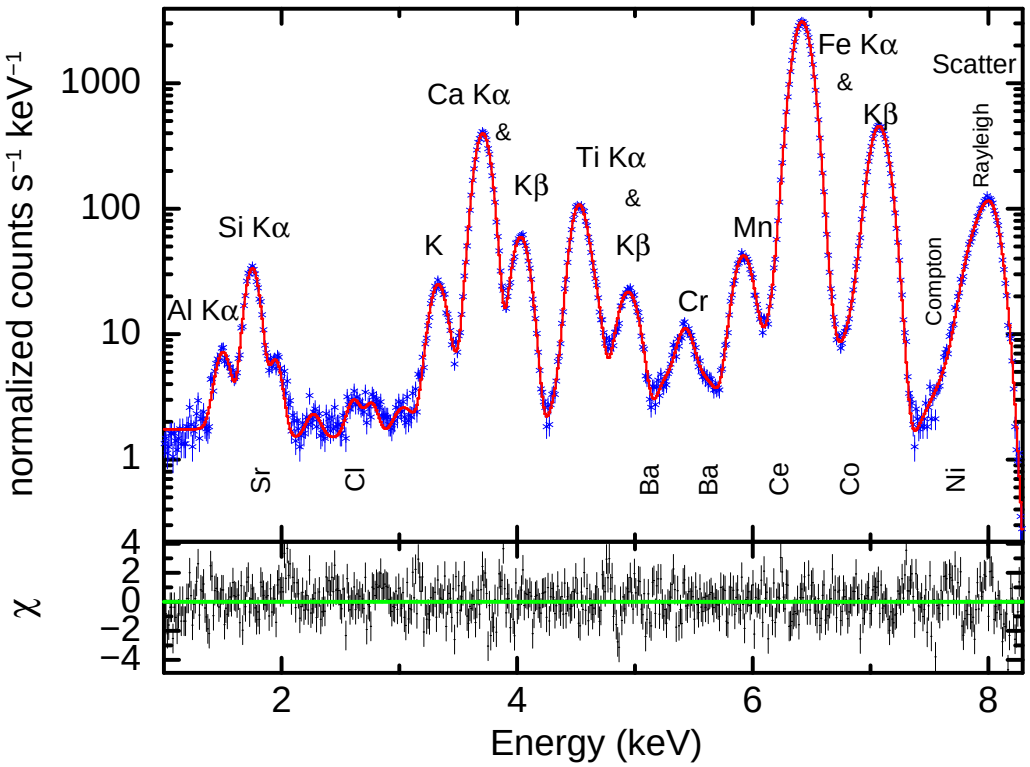

(a) XRF spectrum - Lunar simulant (JSC-1A) - Fit with trace elements

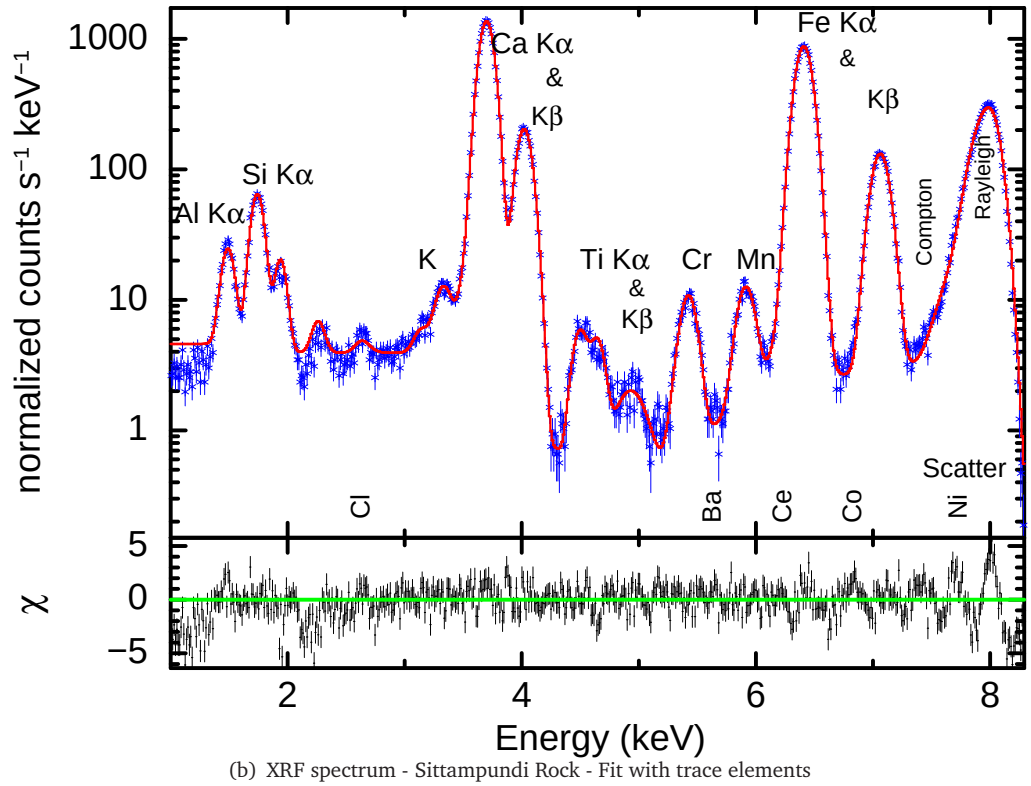

(b) XRF spectrum - Sittampundi Rock - Fit with trace elements

FIGURE 2.4: Best fit for the observed XRF spectra of lunar analogues showing all the components viz., sample XRF lines, SS304 XRF lines & trace elements (marked vertically) (a) JSC-1A & (b) Sittampundi rock sample . Residuals of fit in terms of σ (ref. XSPEC manual) is shown in the bottom panel of each figure.

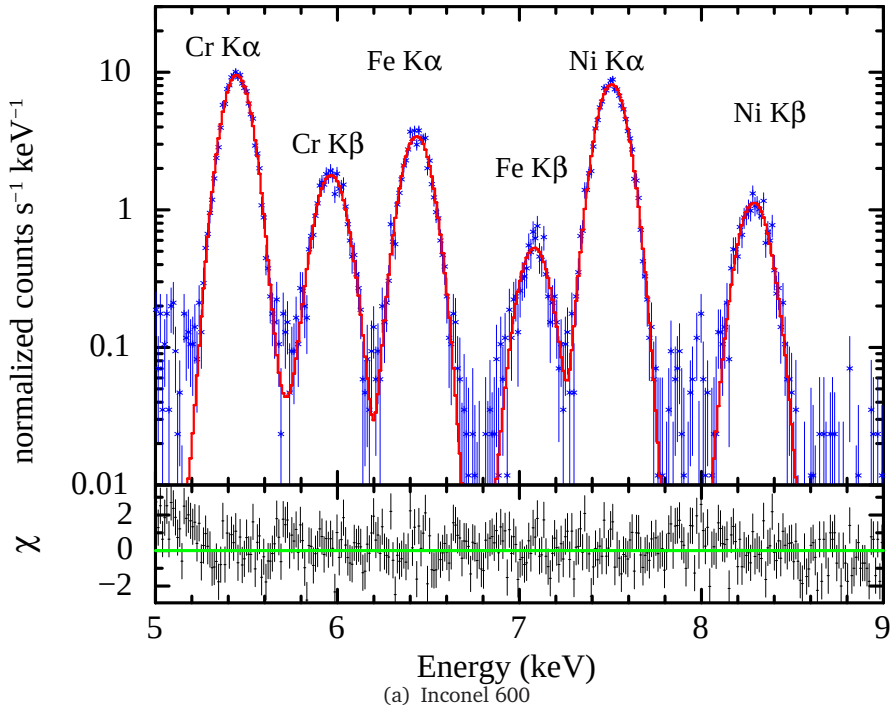

(a) Inconel 600

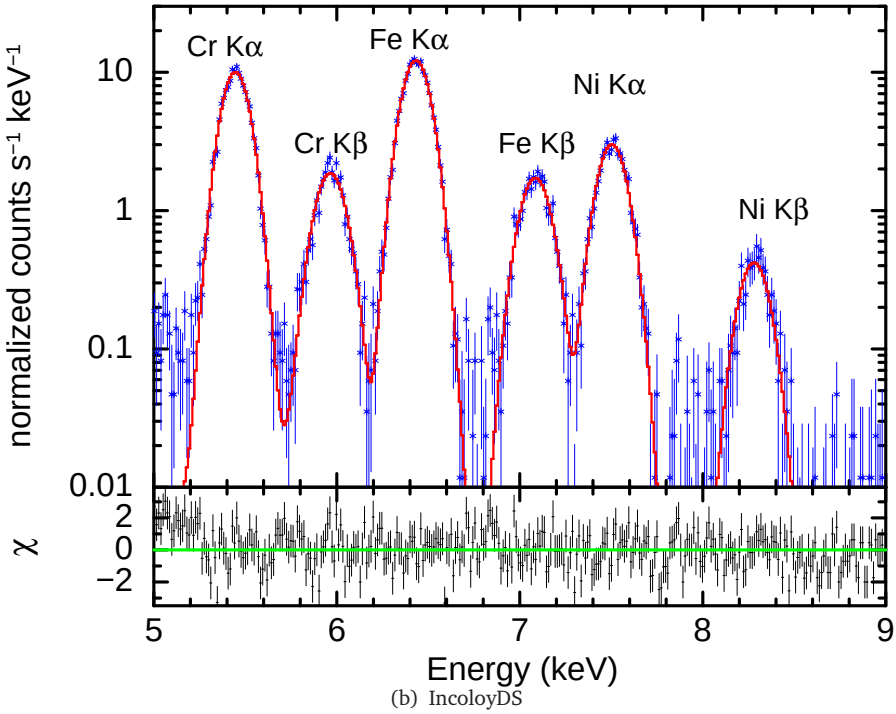

(b) IncoloyDS

FIGURE 2.5: Best fit for the observed XRF spectra of metal alloys used in laboratory experiments. Marked are XRF lines of major elements present in the sample. Residuals of fit in terms of σ (ref. XSPEC manual) is shown in the bottom panel of each figure.

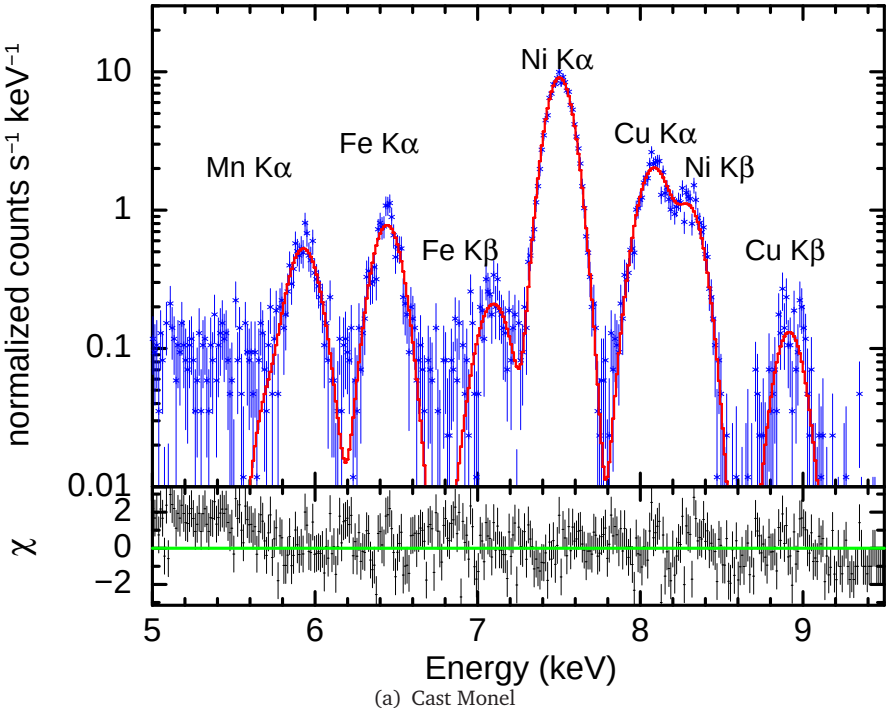

(a) Cast Monel

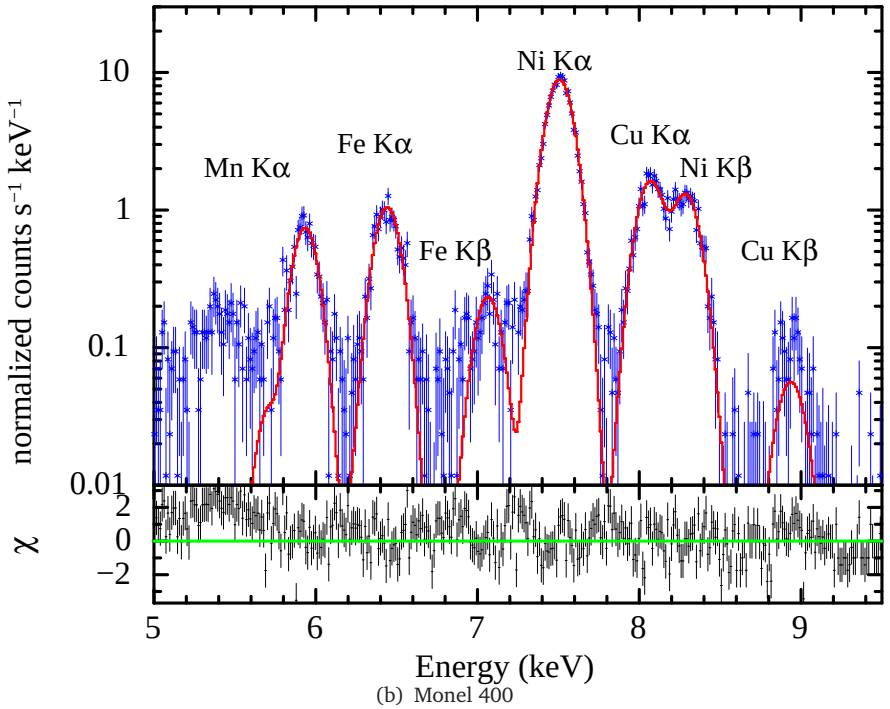

(b) Monel 400

FIGURE 2.6: Best fit for the observed XRF spectra of metal alloys used in laboratory experiments. Marked are XRF lines of major elements present in the sample. Residuals of fit in terms of σ (ref. XSPEC manual) is shown in the bottom panel of each figure.

TABLE 2.4: Comparison of weight percentage (wt%) of major elements of JSC-1A derived by *x2abundance* and EDX measurement values.

Element symbol	**EDX measurement**	*x2abundance* **prediction with trace elements**	*x2abundance* **prediction without trace elements**
Fe	7.5	7 ± 1	7 ± 1
Ti	1.1	$1 + 1$	$1 + 1$
Ca	7.1	7 ± 1	7 ± 1
Si	19.5	18 ± 1	17 ± 1
Al	7.0	9 ± 1	10 ± 1

2.5 Experiment results & Validation

Laboratory experiments : Following the steps enumerated in sec. 2.3.1 - 2.3.4, the inversion algorithm estimated the most suitable composition of each sample. XRF lines of Mg, Na and O could not be seen in the spectrum of JSC-1A due to the low sensitivity of the detector. Hence their values were fixed to priori known weight percentages obtained from EDX measurements (2.6%, 1.5% and 52.7%) respectively. Similarly, for the analysis of Sittampundi sample, abundance of oxygen was kept fixed as 57.0% (EDX measurements). Table 2.4 compares the elemental abundances of lunar simulant (JSC-1A) derived by *x2abundance* along with the measurement using EDX facility at ISAC. Columns (3 & 4) gives the abundances derived for JSC-1A fitted with and without trace elements. For the analysis without trace elements, the predicted abundance can go up to 3σ away from the true value. Inclusion of trace elements in fitting can give abundances which are closer to the true values.

Comparison of elemental abundances predicted by *x2abundance* plotted against true abundances (EDX measurements) along with 2σ residuals are shown in Figs. 2.7(a-b) and 2.8(a). In all the cases, major elemental abundances derived by *x2abundance* with uncertainties agree with the true elemental abundances.

Geant4 experiments : A comparison plot of the predicted abundance vs true abundance of all major elements for certain samples simulated in Geant4 experiment is shown in Fig. 2.8(b). It is evident that the abundances derived from *x2abundance*

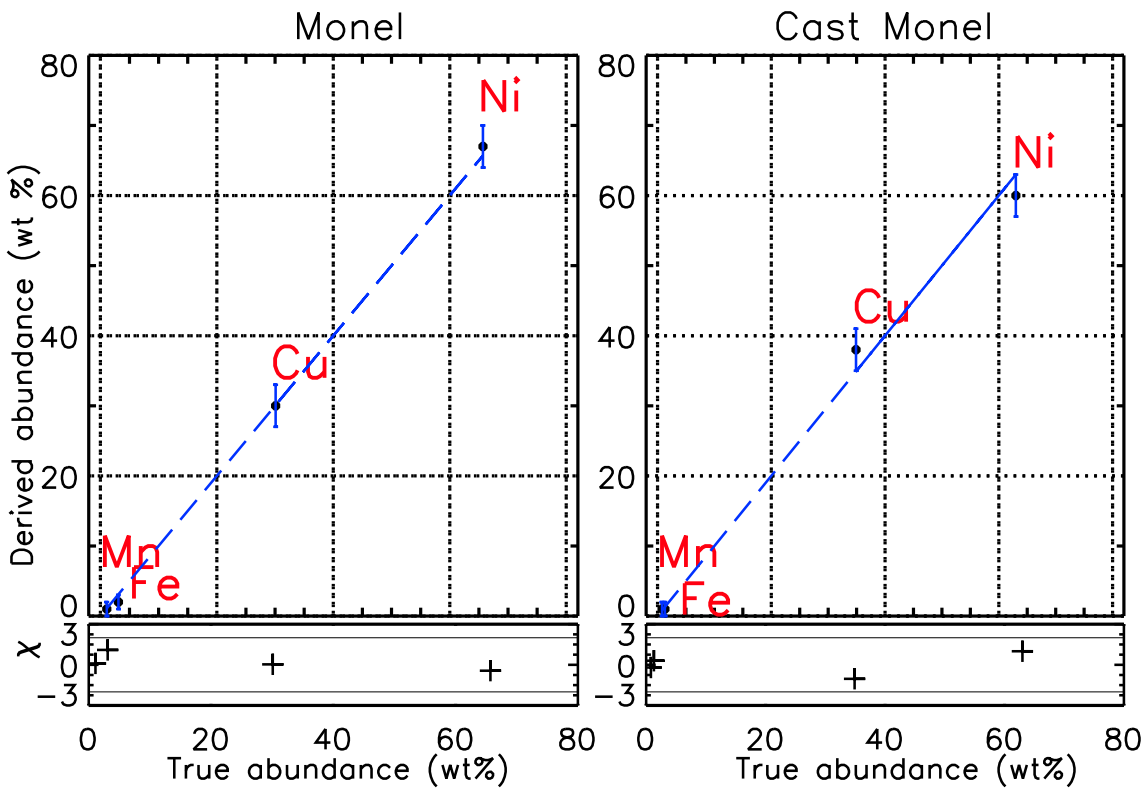

(a) Laboratory experiments - Metal alloys

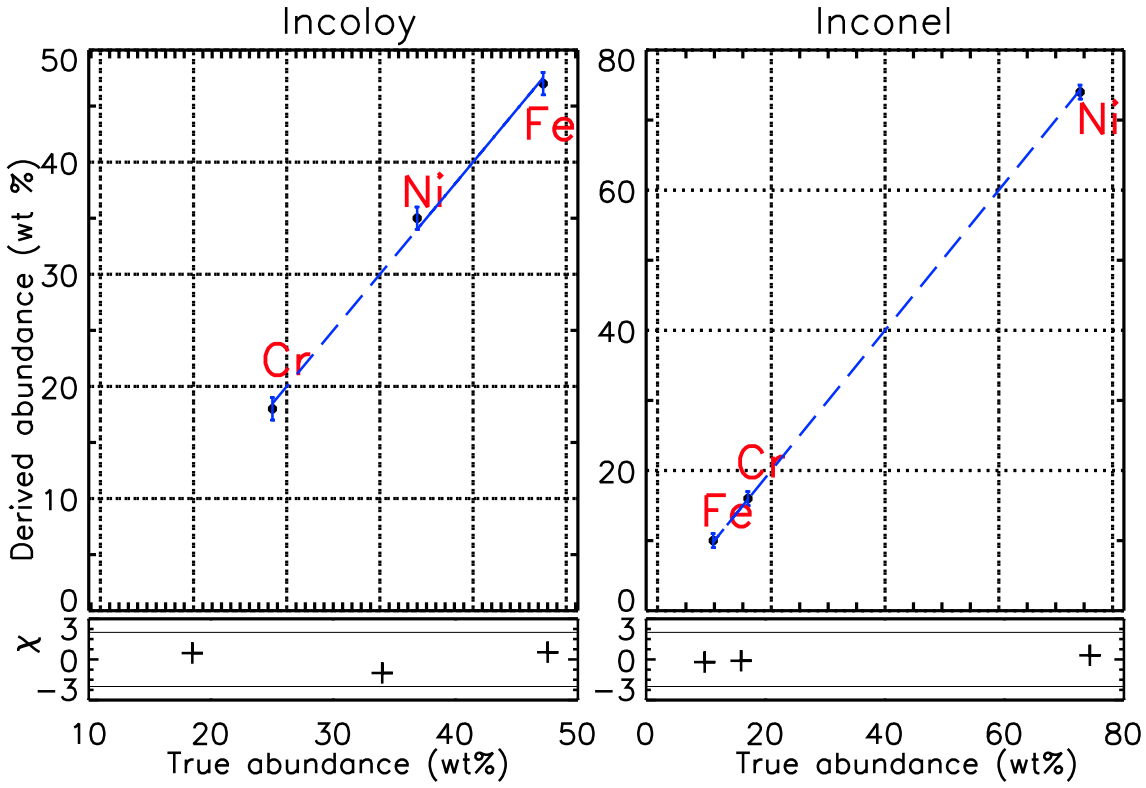

(b) Laboratory experiments - Metal alloys

FIGURE 2.7: Plots showing the deviation of derived abundances with 2σ errors from true abundances based on EDX measurements (for some of the samples in set B). The expected 1:1 relation is represented as dashed line.

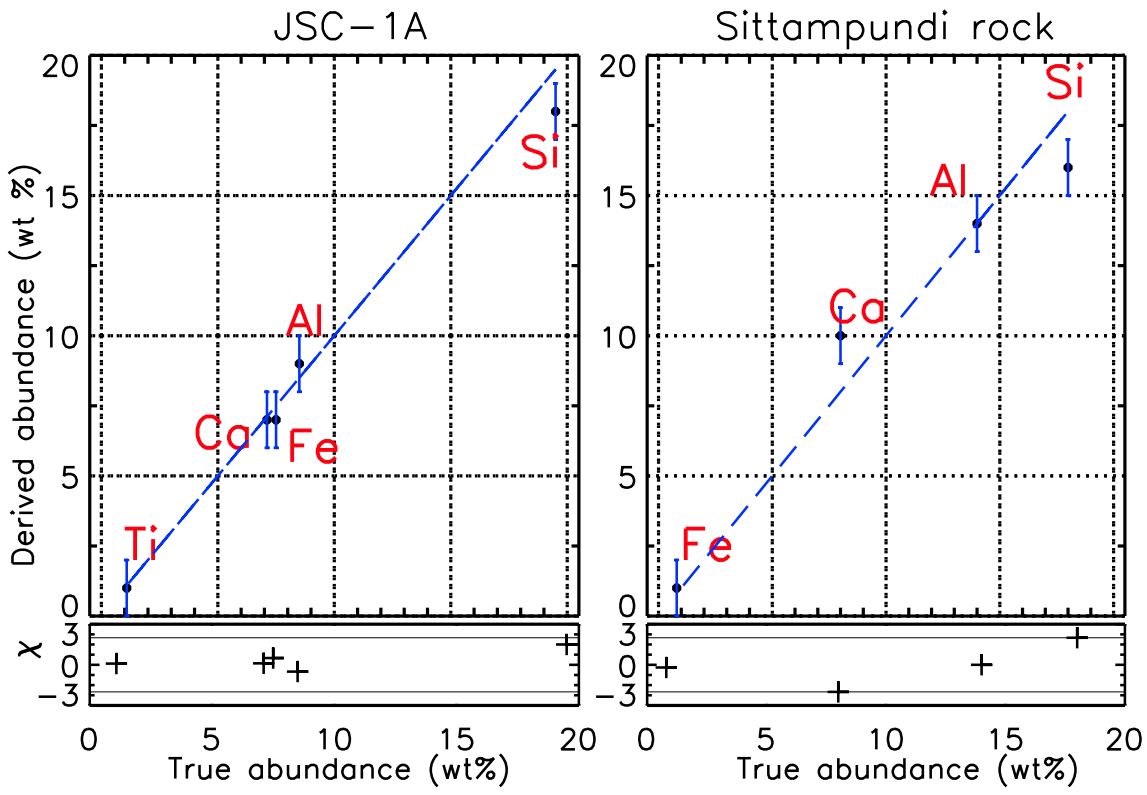

(a) Laboratory experiments - Lunar analogs

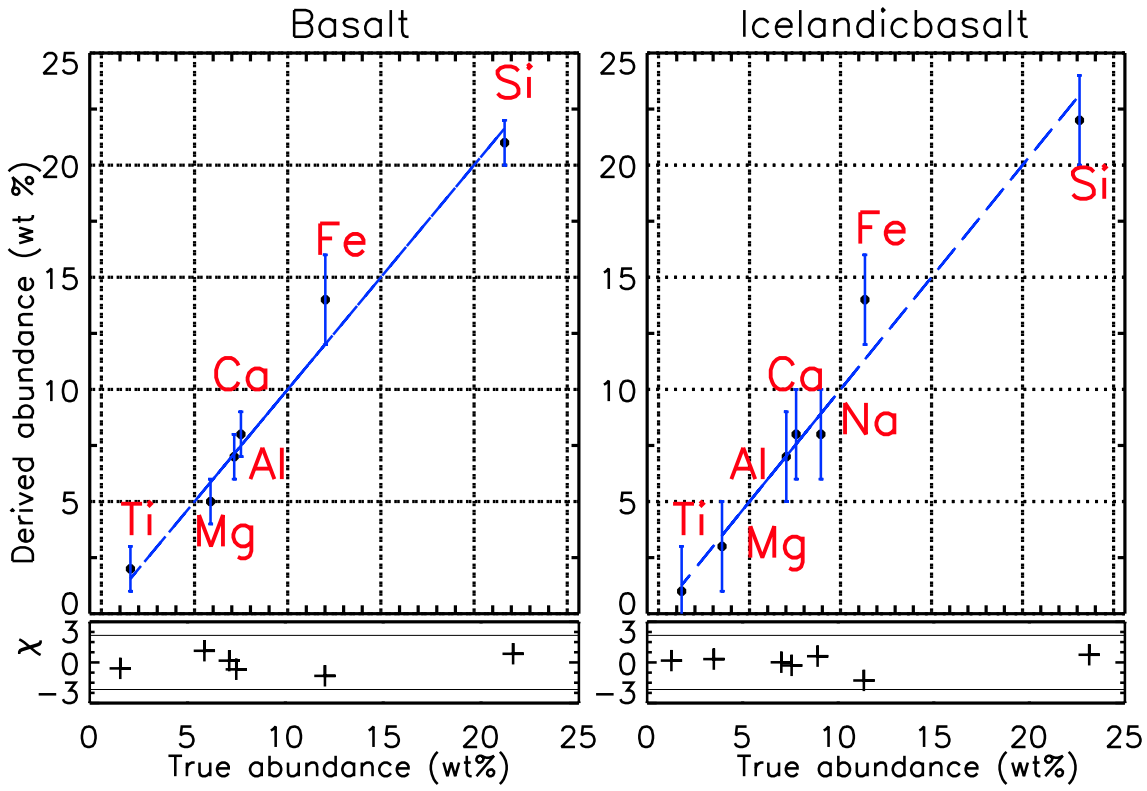

(b) Geant4 experiments

FIGURE 2.8: Comparison plot between the derived abundance(from *x2abundance*) and true abundance (EDX measurements) of laboratory lunar analogue samples. Residuals are plotted in terms of 2σ error bars at the bottom panel. Dashed line represents the expected 1:1 relation.

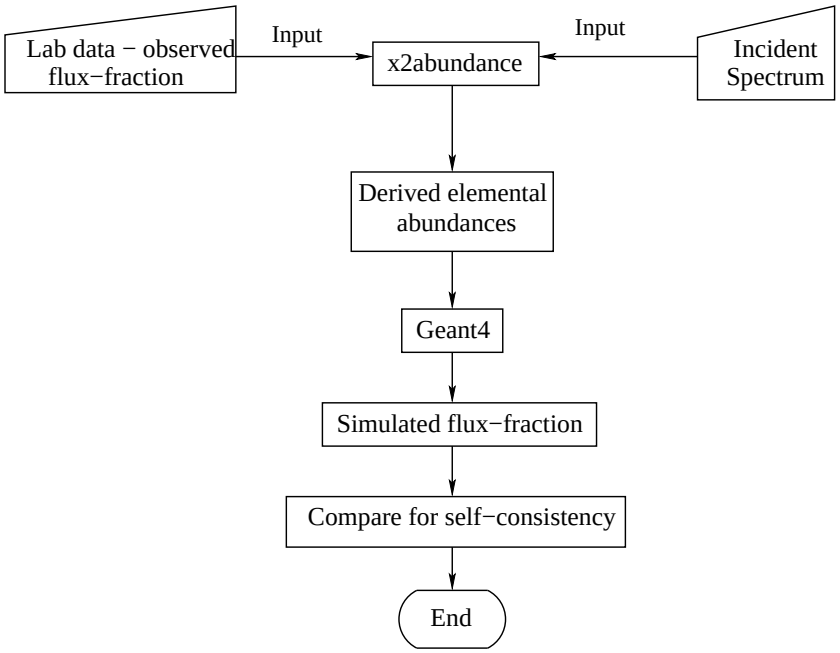

FIGURE 2.9: Steps involved in the cross-validation of *x2abundance*.

matches well with the sample abundances for which Geant4 simulation was performed. The deviations between the two are plotted as residuals (in terms of σ error bars) in the bottom panel.

Cross-validation : We also tested the self-consistency of the inversion process by comparing the measured XRF spectrum with GEANT4 simulated spectrum which used the composition derived by *x2abundance* and convolved with instrument response. Steps involved in the cross-validation are shown in Fig. 2.9. Elemental abundances of Sittampundi sample obtained from *x2abundance* are provided as input for GEANT4 XRF simulation. Fig. 2.10 shows the comparison of simulated flux-fractions plotted against the measured values. The plot also shows the best fit to the data where the slope tending to unity provides a good confidence in the *x2abundance* output. Deviations from the expected slope of unity could be due to unobserved trace elements not modeled in the spectrum.

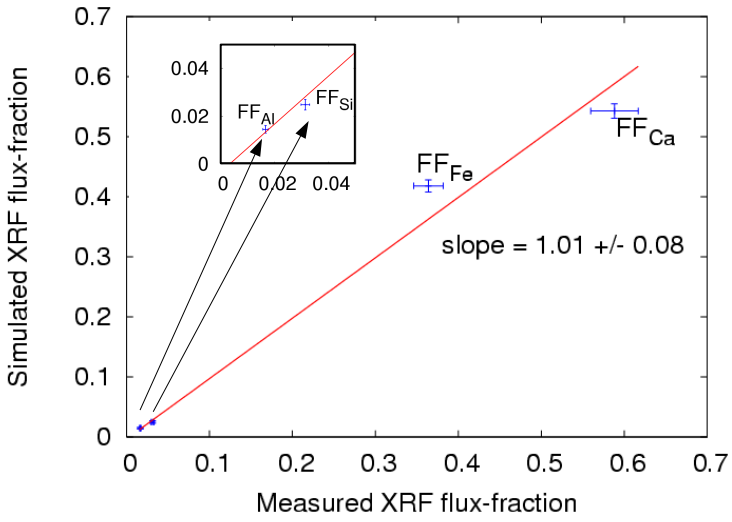

FIGURE 2.10: Comparison of XRF flux-fraction - measured vs simulated - Sittampundi sample. Straight line fit to data which measures a slope of 1.01 is also shown.

2.6 Summary

In this chapter, we have described the complexities involved in the conversion of XRF line fluxes to elemental abundances for space-based XRF studies. Further, we described the formulation of XRF inversion algorithm *x2abundance* in detail, which incorporates some of the major corrections required for the C1XS lunar surface studies. Also, we have successfully demonstrated the validation of *x2abundance* [*Athiray et al.*, 2013a,b] using various XRF experiments whose application on the C1XS lunar data are described in chapter 3. Salient features of the algorithm are listed below:

2.6.1 Highlights of x2abundance

1. Developed for space-based remote sensing XRF studies to convert the observed XRF line intensities to absolute elemental abundances.

2. Invokes the analytical equations of the well-established Fundamental Parameter approach with the assumption of thick, homogeneous and a flat sample.

3. Matrix effects up to tertiary XRF are considered for computation. Other factors affecting the intensity such as incident spectrum and experimental geometry are taken as input parameters.

4. Can derive the elemental abundances with uncertainties for elements with characteristic K-shell x-ray energies between 1-10keV (ie., from Na to Zn).

5. Does not demand any a priori information on the elemental weight percentages provided all the elements are observed in the spectrum (excluding $Z < 10$).

2.6.2 Limitations of x2abundance

1. Assumption of a homogeneous and flat sample surface is not completely true for the case of lunar studies. Hence, our approach gives only a first order correction factor for the mixture of minerals and does not strictly address the heterogeneity in the lunar regolith.

2. It is also assumed that the effect of particle size has negligible effects on XRF intensity over large scales of observation covering large phase angles. The effect is partially eliminated by the use of flux-fractions.

3. Major elements whose x-ray signatures are detected are included in matrix generation. Additional undetected but known-to-be-present elements are included using a-priori knowledge. For example, Oxygen (Z=8) occupies a major fraction in almost all rock samples. In such cases, its weight percentages are frozen to previously published best estimate values.

4. Fundamental parameters for elements with Z<10 are not known to high precision and hence not included in the matrix.

Chapter 3

Lunar surface chemistry from C1XS

This chapter gives an overview of the C1XS experiment. A complete summary of C1XS observations, analysis and results are presented. Detailed explanation on approach to spectral analysis under different flare conditions, estimation of in-orbit x-ray background and solar flare x-ray analysis are included. Application of x2abundance to C1XS analysis and new scientific insights on the surface geochemistry of the Moon from C1XS-derived abundances, are explained in detail. We present the first direct evidence of enhanced Na abundance on the lunar surface and discuss its science implications. At the end, we describe improvements addressed in the design of the x-ray spectrometer planned on Chandrayaan-2.

3.1 Introduction

In chapter 1, we discussed different mapping techniques that are used in deciphering the surface chemistry of the Moon. In particular, how remote sensing studies using XRF spectroscopy can help in direct chemical mapping of the Moon. Also, a comparative summary of earlier space-based lunar XRF experiments is given in chapter 1. Though this technique was deployed during earlier missions since the Apollo era, the Chandrayaan-1 mission was optimally designed to generate maximum coverage and give the most spectroscopically accurate measure of lunar surface elemental abundances. C1XS reached

the Moon without losing much of its high spectral capability. The unusually low solar x-ray activity hampered completion of the primary scientific objective of C1XS of creating global lunar elemental maps using XRF emission lines. An overview of C1XS experiment, XRF observations, data selection methods, analysis and results are discussed in subsequent sections.

3.2 Overview of C1XS

Chandrayaan-1, India's first lunar mission was launched on 22^{nd} October 2008 and was in operation until August 2009. The orbit of Chandrayaan-1 spacecraft was a circular polar orbit around the Moon at an altitude of 100 km in the initial phase (called phase 1) and later raised to 200 km (called phase 2). The C1XS experiment onboard Chandrayaan-1 was designed to map the abundances of major rock-forming elements on the lunar surface. C1XS was a joint collaboration between European Space Agency (ESA) and ISRO; the instrument was built at the Rutherford Appleton Laboratory (RAL), UK, with some design contributions (instrument and thermal) from ISRO and jointly calibrated and operated by RAL and ISRO. The instrument was designed to have an opening angle of 28.6° using collimators which were mounted on top of the detectors. The collimators were made of copper, coated with gold which define the ground pixel (area seen by C1XS on the lunar surface at a given instance) resolution of 25 km FWHM from 100 km altitude. However, spatial resolution for single spectral observation varies from 25 km to few hundreds of kms, depending on spacecraft altitude and co-adding of adjacent pixel data for improved signal to noise ratio. Extended solar minimum that prevailed during the on-orbit time of Chandrayaan-1 (ie., Nov'08 - Aug'09), left C1XS with only a handful of solar flare (a few C-, B- and A-class flares) when simultaneous observations of the lunar surface were made. C1XS is the first well-calibrated x-ray instrument to reach and observe the Moon with good spectral resolution.

3.2.1 X-ray detectors in C1XS

C1XS used an array of 24 Swept Charge Devices (SCDs) [*Lowe et al.*, 2001], each with area of 1 cm^2, to record x-ray emission in the energy range of 0.8 to 20 keV. SCDs are modified version of x-ray CCDs, specially designed for non-imaging, spectroscopic purposes by e2V technologies Ltd., UK. They offer good spectral resolution at benign operating temperatures. On-board, C1XS used only a passive cooling system and the detectors were operated between -10 °C to +5 °C. The SCD provides an 1-dimensional linear output array as a resultant of the continuous diagonal read-out architecture, which are processed to control stored data volume for varying input raw event rates. Extensive ground calibration of SCD was performed using a double crystal monochromator in the RESIK x-ray beam-line at RAL. Further details on ground calibration and determination of detection efficiency of SCD with respect to calibrated Si-PIN detector are explained in detail elsewhere [*Narendranath*, 2011].

3.2.2 Event selection process

The observed x-ray event rates in C1XS vary with changing intensity of a solar flare. In order to control the in-orbit data volume, C1XS had two event processing modes viz., Time-tagged mode (during low and moderate event rate) & Spectral mode (during high event rate) [*Howe et al.*, 2009]. Due to low solar x-ray activity, the observed C1XS event rate was low throughout the mission. Hence events were processed in time-tagged mode where each event was attached with the on-board time and SCD number. This mode was further subdivided into two other modes based on event rates and two threshold logic which are :

1. **Type 11 data - Multi-pixel mode ($\leq$ 51 events/s)**: Out of a group of 3 adjacent samples, if the central one is above threshold 1, then store all the 3 samples.
2. **Type 10 data - Single-pixel mode (51-129 events/s)** : Out of a group of 3 adjacent samples, only the central one is stored if it is above threshold 1 and both the adjacent samples are below threshold 2. Otherwise discard the central sample.

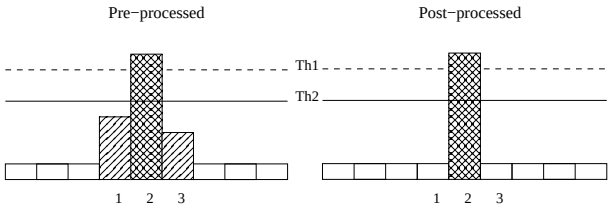

FIGURE 3.1: Representation of 'Single pixel (Type 10 data)' event selection logic used in C1XS with two threshold values *Th1, Th2*.

Spectral mode, in the case of high count rates also follows single-pixel mode logic with two thresholds. Pictorial representation of single-pixel mode event selection logic is shown in Fig. 3.1. Single-pixel mode data alone were considered for spectral analysis since majority of the events during weak flares observed by C1XS belong to this mode. Pulse height distribution of charges collected due to a specific energy x-ray photon event, varies with different selection modes which leads to different spectral shapes. Details of SCD architecture, interaction with x-ray photons, charge formation and transportation and application for lunar spectroscopic purposes are discussed in detail in chapter 4.

3.2.3 X-ray Solar Monitor (XSM)

From chapter 1 and 2, it is clear that accurate measurement of incident solar x-ray spectrum is a prerequisite to derive precise lunar surface elemental abundances. Simultaneous observations of solar x-rays, in the energy range of 1.8 to 20 keV, impinging on the Moon, were obtained from the X-ray Solar Monitor (XSM) [*Alha et al.*, 2009] onboard Chandrayaan-1. XSM was developed by the University of Helsinki in Finland, based on a Si-PIN detector. The detector was designed to have a wide opening angle of 105 $^\circ$ to ensure the Sun to be in its field of view (FOV) always. The detector was operated around -18 $^\circ$C using a Peltier cooler and had an effective area of 0.001cm^2.

3.3 C1XS observations

C1XS was nominally operated only during the sunlit portion of the lunar orbit. The light curve of counts recorded by the C1XS experiment for the entire mission is shown in Fig.

3.2. The plot shows integrated C1XS counts in the energy range 1 keV - 10 keV (red color points in Fig. 3.2) plotted along with GOES [1] soft x-ray flux in the energy range 1.55 keV - 12.4 keV (blue color lines in Fig. 3.2). It is clearly seen that the solar x-ray activity was very minimal during the entire duration and was relatively active in x-rays only in the month of July 2009, in contrast to other times. Due to the overall low solar x-ray activity, C1XS could not produce global elemental maps of the Moon during its short mission life.

Major observations during phase 1 contain a few A-class flares reported by [*Weider et al.*, 2012] which occurred on 12^{th} December 2008 and 10^{th} January 2009. Observations in December 2008, sampled full latitudinal extent of Mare Serenitatis and the January 2009 observation followed a track through Mare Insularum, Mare Cognitum and Mare Nubium. During phase 2, C1XS observed two major C-class (10^{-6} - 10^{-5} W/m^2) flares, a few B-class (10^{-7} - 10^{-6} W/m^2) flares and a few A-class (10^{-8} - 10^{-7} W/m^2) flares. The brightest flare observed by C1XS was a C3 flare which occurred on the 5^{th} July 2009, where x-ray signatures of major rock-forming elements viz., Mg, Al, Si, Ca, Ti & Fe were measured simultaneously. This observation covered some regions on lunar southern nearside highlands at detectors' maximum spatial resolution [*Narendranath et al.*, 2011]. The Copernican-aged impact crater Tycho and its rays were observed during another weak C-class flare (C1) that occurred on 6^{th} July 2009. Other B-class flare observations correspond to various terrains on the nearside of the Moon. In the following sections, we present some of the new results from a more comprehensive analysis of C1XS data for all observations including those during weak solar flares.

3.3.1 Data selection

After careful examination of all data, the following criteria were adopted in choosing good data for spectral analysis from the complete set of C1XS observations for spectral analysis.

[1] Geostationary Orbiting Earth Satellite which monitors the space weather near the Earth from an altitude of 36000km

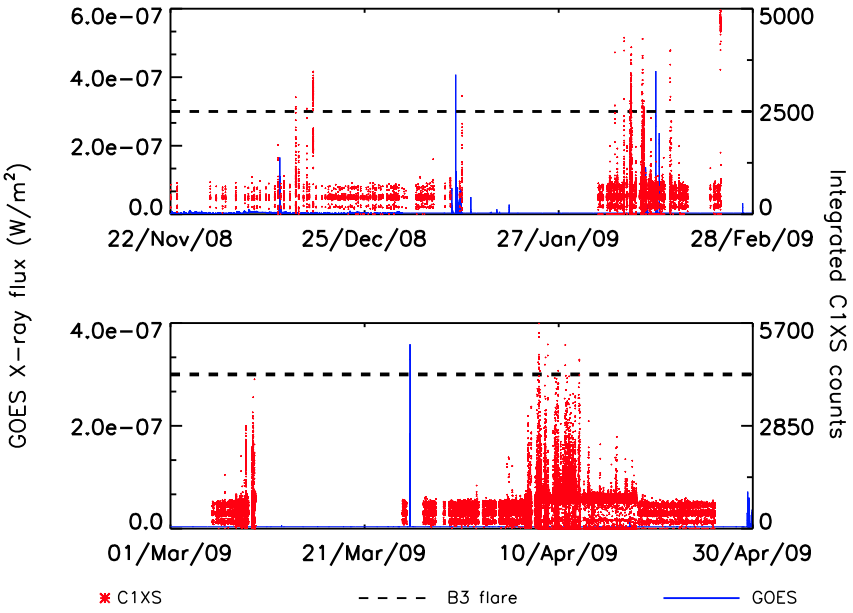

(a) Nov'2008 - Apr'2009

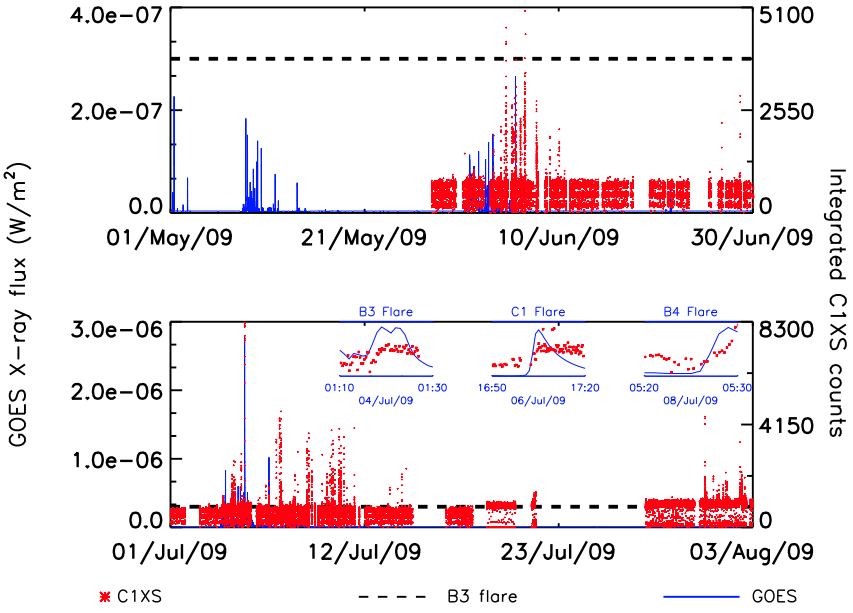

(b) May'2009 - Aug'2009

FIGURE 3.2: The entire mission light curves of C1XS from 22^{nd} Nov.2008 - 3^{rd} Aug.2009. Solar x-ray flux from GOES satellite indicating x-ray activity of the Sun during the life time of the mission is also shown (1 - 8 Å). Useful C1XS observations are during solar flares with intensity B3 (3×10^{-7} W/m^2) and above, which is marked by a dashed line. Red points indicate C1XS integrated counts with a time bin of 16 sec; Blue lines indicate solar X-ray flux with a time bin of 1min. Flare observations discussed in this paper are shown in the inset of Fig. 3.2(b). GOES x-ray data are chosen for the light curve to show very low solar activity during this entire period and to also address potential flares, undetected by XSM which may have resulted in lunar XRF signatures in C1XS. GOES data are available almost all the times and also acts as an independent observation of solar flare from a different location which agrees well with C1XS light curve.

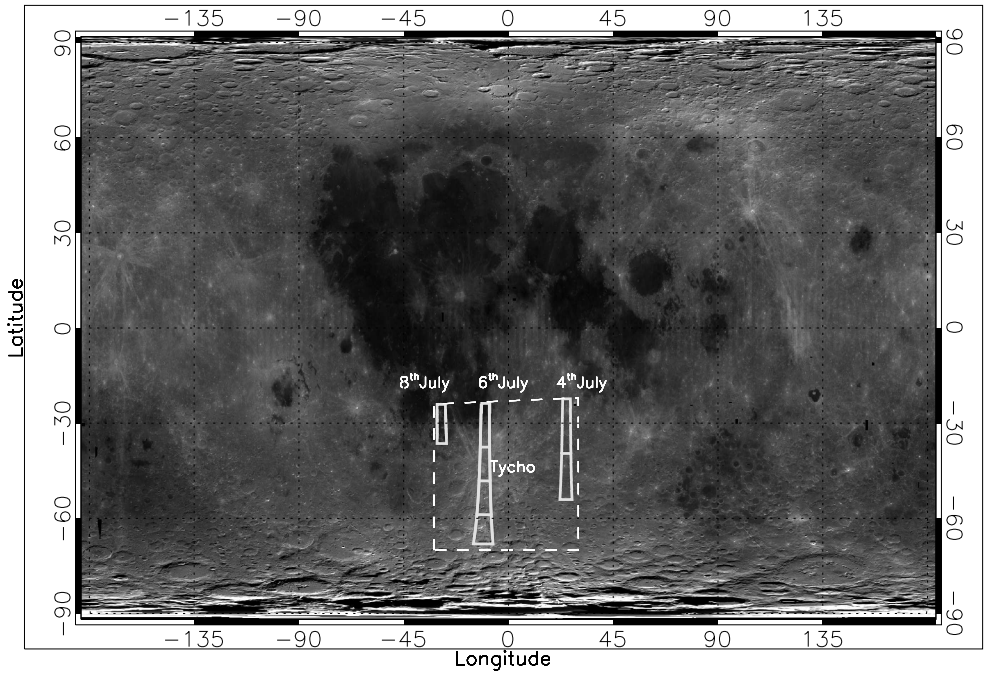

FIGURE 3.3: Ground-track of C1XS observations made on 4^{th}, 6^{th} and 8^{th} July 2009 plotted over the Clementine lunar albedo map (750nm). Elemental abundances from the LP gamma-ray data used for comparison are taken from the region of interest shown as dashed line box which encompass C1XS observed locations

C1. Identification of observation intervals corresponding to solar flares

C2. Within this, selection of good observation intervals where data are not contaminated by enhanced flux of charged particles (as derived from hardening of C1XS spectra)

Interaction of charged particles with spacecraft and detector can increase the background and hence could impact spectral analysis. Also flares below B3 (dashed lines in Fig. 3.2) are not considered for further analysis as lines corresponding to Ca, Ti and Fe are absent, resulting in large errors in the derived abundance values. Results of the biggest flare seen by C1XS (a C3 flare), which occurred on the 5^{th} July 2009 are published in *Narendranath et al.* [2011]. We discuss flare observations made on the 4^{th}, 6^{th} and 8^{th} July 2009 ($<=$ C1 class flares), as shown in the inset of Fig. 3.2(b), which satisfied the aforesaid criteria. The majority of these observations (viz., 4^{th}, 6^{th} and

8^{th} July 2009 $\leq$ C1-class flares) span over lunar southern latitudes which include the relatively young impact crater Tycho and its rays as shown in Fig. 3.3. A summary of good observation intervals chosen for analysis along with the class of flares observed and their respective locations on the Moon are given in Table 3.1.

TABLE 3.1: Selected good observation intervals of C1XS data

Date & time	**Class of solar flare**	**Observed region (Lat, Lon)**	**Groundtrack details**
4^{th} Jul'09		-53.0°,25.0°	Nearside - highland region
	≈B3.5	to	covered some portions over the rays
01:18:00-01:21:59		-23.5°,25.0°	of the relatively young impact crater Tycho
6^{th} Jul'09		-66.2°,-6.3°	Nearside - highland region
	≈C1.1	to	from the crater Cysatus till
17:04:29-17:19:44		-26.3°,-9.5°	near the boundary of Mare Nubium
8^{th} Jul'09		-35.4°,-28.6°	Nearside - Palus Epidemiarum
	≈B4.2	to	from the crater Capuanus to the crater
05:27:31-05:30:20		-25.9°,-28.7°	Campanus which separates Mare Nubium

3.4 Data analysis

C1XS observations can be broadly grouped into three types viz., background observations ie., when enhanced x-ray & particle events are not observed, flare observations with only enhanced x-rays and observations during enhanced flux of charged particles. Light curves depicting these types of observations are shown in Fig. 3.4. Spectral analysis of weak flare observations is severely constrained by low signals, requiring data from multiple ground pixels to be summed. This leads to coarser spatial mapping. Following are the major steps involved in spectral analysis :

1. Build background spectrum appropriate for the observation - B(E)
2. Obtain incident solar x-ray spectrum pertaining to C1XS observations using XSM data - I_0(E) (spectral analysis)
3. Derive scattered spectrum of solar flare, reflected off the lunar surface - I_R(E)

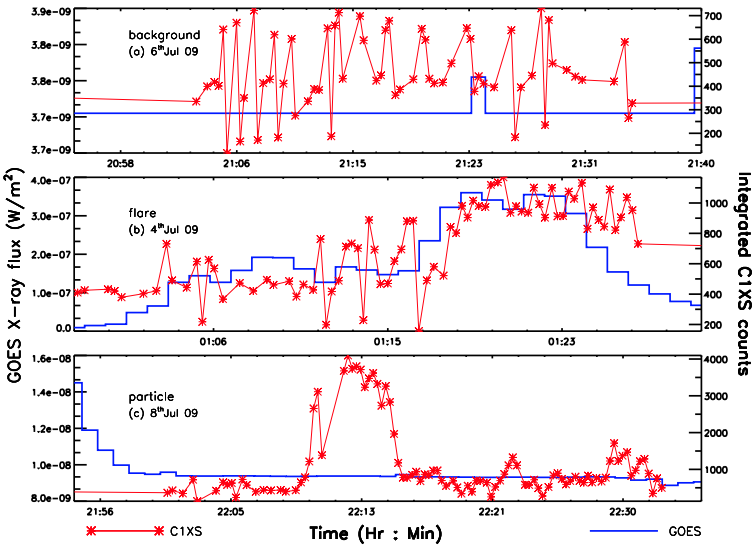

FIGURE 3.4: Light curves showing C1XS integrated counts (0.94 keV - 9.4 keV) (indicated by red points with a time bin of 16 sec) along with x-ray solar flux obtained from GOES (1.55 keV - 12.4 keV) (indicated by blue lines with a time bin of 1 min) (a) background observation - absence of solar flare & low particle flux (b) flare observation showing enhanced solar x-ray flux and C1XS counts (c) particle interaction dominated observation- envisaged as sudden rise in the C1XS counts without commensurate increase in the solar x-ray flux directly measured flux.

4. Derive x-ray line fluxes of different elements from spectral analysis

5. Convert XRF line flux to elemental abundance using *x2abundance* (ref. chapter 2)

3.4.1 Background estimates (B(E))

Background emission arises from various sources [*Hall et al.*, 2008]. Apart from cosmic x-rays, interaction of high energy charged particles around the Moon with the instrument leads to production of secondary charged particles and x-rays which also contributes to the overall observed continuum background. Also energetic charged particles deposit partial charge in the detector which mimic x-ray-like signatures. As the spectrum of charged particles vary dynamically with time, the observed background also exhibits time variations. XRF lines from the Moon are recorded along with this time varying

background. Thus in order to extract XRF elemental line fluxes, understanding and accounting of the background is very important. The Moon encounters two major particle environments in a synodic month (29.6 days) which are :

(a) Solar wind & high energy cosmic ray particles (dominant during $\approx$ 24 days) : Continuous flux of solar wind and galactic cosmic ray protons and electrons with energies ranging from keV to GeV contribute mainly to the observed steady background in C1XS.

(b) Charged particles in the Earth's geotail (dominant during $\approx$ 6 days) : The high pressure solar wind pushes the magnetic field of the Earth and stretches it out into an elongated tail in the anti-solar direction. In a lunar month, the Moon spends $\approx$ 6 days around the full moon phase inside the geotail. The geotail extends up to several hundreds of Earth radii and is primarily composed of energetic electrons with an average energy of 1 keV (increasing to several keV occasionally; [*Prakash*, 1975]). Sporadic release of accelerated charged particles during solar eruptive events can alter the background spectrum significantly. The accelerated charged particles travel with different speeds and reach the Earth and the Moon at different times. Spectral contamination due to sudden bursts of charged particles is clearly identified by huge rise in C1XS counts as observed in the light curve that are uncorrelated with solar x-ray emission (refer Fig. 3.4(c)).

The Moon was coincidentally inside the geotail when flares occurred during the 1^{st} week of July 2009. Data over a complete orbit, without particle contamination and with solar activity less than A-class flare level (ie., $< 1\times10^{-8}$ W/m^2) alone were considered for background estimation. Some of the observations made on the 6^{th} and 8^{th} July 2009 satisfied this condition and the time-averaged background spectrum (B(E)) used for our current analysis is shown in Fig. 3.5. For comparison, spectral hardening due to a sudden burst of charged particles inside the geotail is also shown in Fig. 3.5.

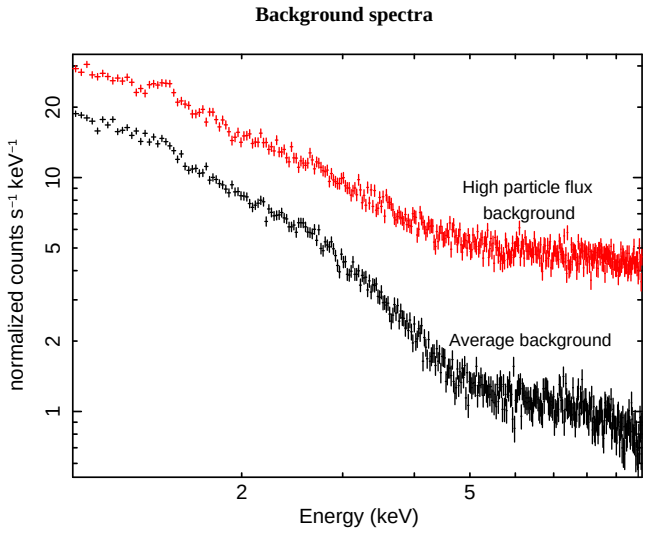

FIGURE 3.5: C1XS average background spectrum inside the geotail measured from multiple orbits during the month of July 2009 used for data analysis along with a spectrum corresponding to high particle flux (red color points).

3.4.2 Incident solar spectrum (I_0(E)) - XSM spectral analysis

The incident solar spectra (I_0(E)) for the observed C1XS timings were obtained from XSM data. Spectral analysis was performed using the solar soft package (SSW) which uses solar models based on CHIANTI5.2 [*Dere et al.*, 1997; *Landi et al.*, 2006] atomic database. XSM data were fitted with single plasma temperature and varying coronal abundances (vtherm and vthermabund in OPSEX which is a model based on atomic database) to match the observed solar x-ray intensity. The best spectral fit to one of the observed XSM spectrum (C1-class flare) is shown in Fig. 3.6 along with its spectral components. The best fit solar spectral model was used in *x2abundance* to compute the lunar XRF line intensities. Further, we calculated the scattered solar component using the solar model as follows:

3.4.3 Scattering of solar X-rays (I_R(E))

Elastic/Rayleigh scattering is the second dominant process of interaction for low energy x-rays next to photoelectric absorption. Interaction via Rayleigh scattering retains the energy of the incident photon after getting scattered by the bound electrons (refer sec.

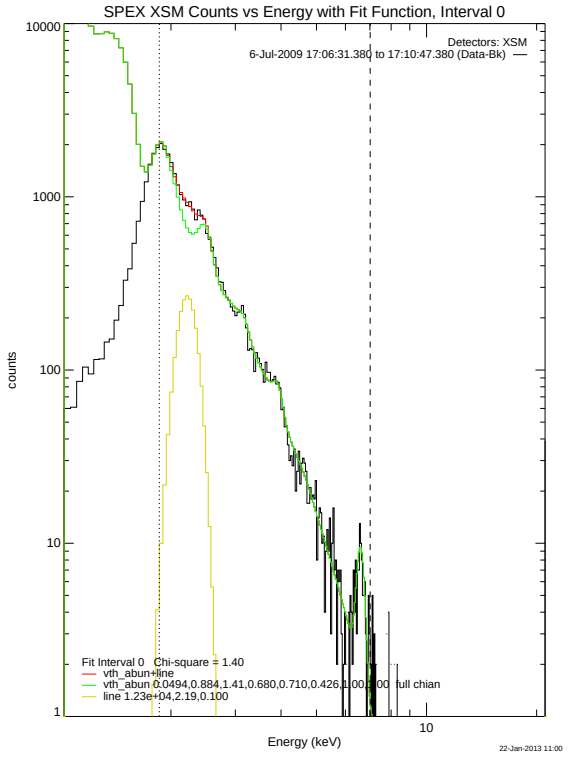

FIGURE 3.6: Best fit to one of the solar spectra observed by the XSM on 6^{th} July 2009, using the CHIANTI database. The observed continuum spectrum along with the ionized solar coronal emission lines are well modeled using *vtherm_abund* in OSPEX (Object Spectral Executive - an interface tool for solar X-ray data analysis in SSW) (Green line). Further, a Gaussian component is fitted at $\approx$ 2.1 keV (Yellow line) for improved fit. Red line represents the combined spectral fit and data points are in Black.

(1.4.2)). The elastic scattering cross section depends on the incident photon energy, atomic number of the element as well as the scattering angle which is given as :

$$\sigma_R = \frac{r_0^2}{2} \int_{\theta_{min}}^{\theta_{max}} (1 + cos^2\theta) \;\; |F(x,Z)|^2 \; 2\pi \; sin\theta d\theta \tag{3.1}$$

where F(x,Z) is the atomic form factor, θ is the angle of scatter. Background-subtracted C1XS spectra contain XRF lines as well as scattered solar x-rays which include both ionized emission lines and broad thermal continuum. In order to model the scatter component, the incident solar spectrum, observational geometry and compositional knowledge of lunar surface are essential. Solar spectrum was obtained from XSM data, observing angles and positional coordinates of C1XS observations were obtained from spacecraft telemetry data. We started with an apirori composition based on broad contextual

knowledge (highland region vs mare region) and modeled the scattered component iteratively. The intensity of elastically scattered spectrum (I_R(E)) from an infinitely thick sample can be computed using :

$$I_R = \int \frac{I_0(E)\ \sigma_R(E)}{\mu(E)[cosec\phi + cosec(\psi)]} dE \tag{3.2}$$

where ϕ & ψ are incident and emission angles. For apriori composition, we adopted *Korotev et al.* [2003] for the average feldspathic terrane composition. The scattered spectrum computed using Eq. (3.2) with apriori composition was used as a component while fitting the C1XS spectrum and XRF line fluxes were derived. Abundances determined from these line fluxes using the inversion algorithm were used in subsequent iterations to re-compute the scattered spectrum which was again used in spectral fitting and line flux determination. Computations were repeated until line fluxes of successive iterations did not vary beyond their error bounds and in general convergence was obtained within two iterations.

3.4.4 Spectral analysis - First confirmed detection of Sodium

Detailed XRF spectral analyses were carried out using x-ray spectral analysis package (XSPEC) [*Arnaud*, 1996], where XRF lines were modeled as Gaussian functions along with an estimated scattered solar spectrum corresponding to a location/time interval (included as table model [2]). The best fits to C1XS spectra with XRF lines marked are shown in Fig. 3.7 and 3.8. Due to excitation by weak solar flares, XRF signatures of Ti & Fe are not visible in most of the observations. It is evident from Fig. 3.7 and 3.8 that C1XS had clearly observed the XRF signature of Na at $\approx$ 1.04 keV in many spectra. Fig. 3.7(b) shows the unfolded C1XS spectrum for an interval during a C1 flare, with the best fit calculated scattered component. Other C1XS reports by [*Narendranath et al.*, 2011] and [*Weider et al.*, 2012] also discussed the detection of Na from the Moon. The former proposed the possibility of high Na content on the lunar surface, while the latter

[2]Table Model - A model in XSPEC can also be defined as a two column table (energy versus photon intensity at some specified binning) as opposed to an analytical form. The final model spectrum is calculated by interpolation across the bins.

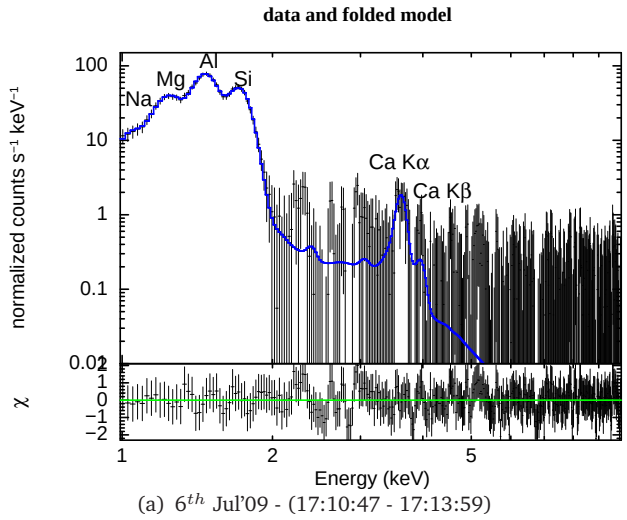

(a) 6^{th} Jul'09 - (17:10:47 - 17:13:59)

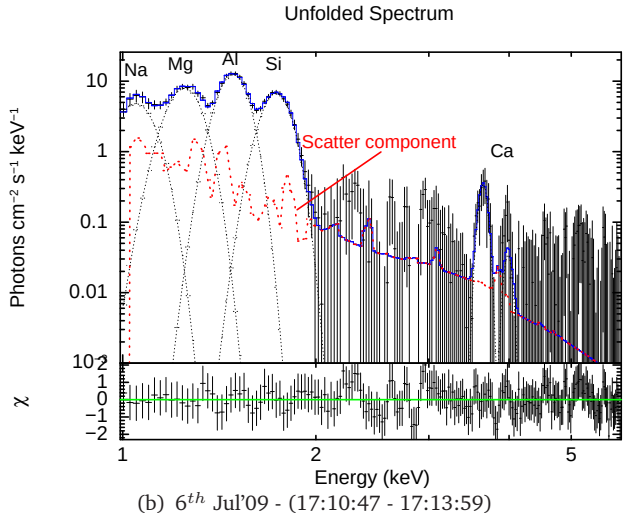

(b) 6^{th} Jul'09 - (17:10:47 - 17:13:59)

FIGURE 3.7: Best fit for the observed XRF spectrum for an interval during a C1 class flare, with all spectral components also shown. Data points are shown with error bars; XRF lines of major elements are marked. Residuals of fit (difference between model and data) in terms of σ are shown in the bottom panel of each figure.

argued that it originated from the scattering of incident solar spectrum. However due to non-availability of good XSM data for the A-class flare observations, a standard solar spectral model using **atomdb** package (version 2.0.0)[3] was used in that analysis. In contrast, here for observations of B- & C-class flares, we modeled the directly observed XSM spectrum and calculated the corresponding scattered solar spectrum, providing greater confidence in the residual signal. To further confirm the signature of Na, we carried out an independent spectral analysis to model the scatter component. It was known

[3] (Harvard Chandra X-rayCenter : http://cxc.harvard.edu/atomdb/features_idl_html)

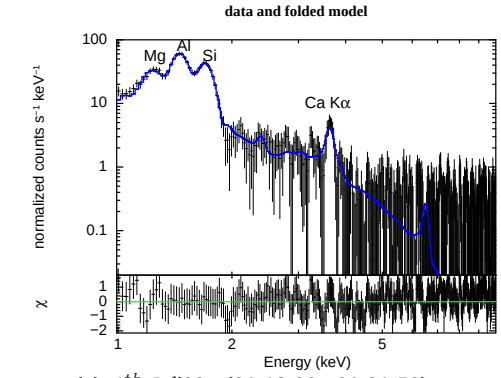

(a) 4^{th} Jul'09 - (01:18:00 - 01:21:59)

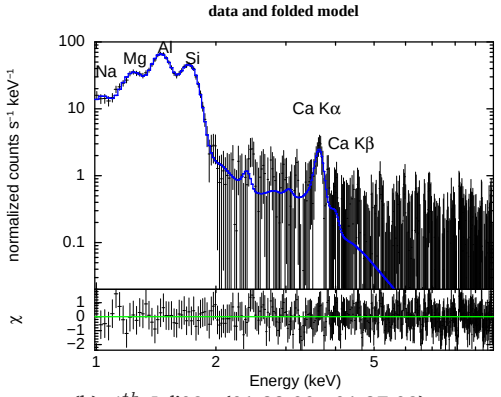

(b) 4^{th} Jul'09 - (01:22:00 - 01:27:09)

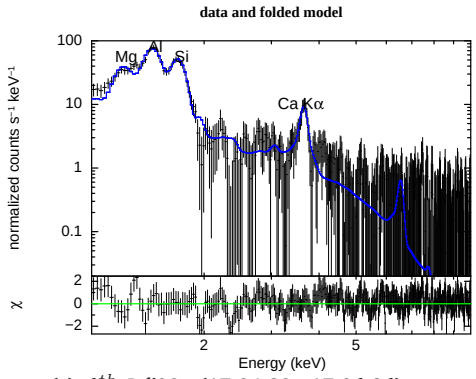

(c) 6^{th} Jul'09 - (17:04:29 - 17:06:26)

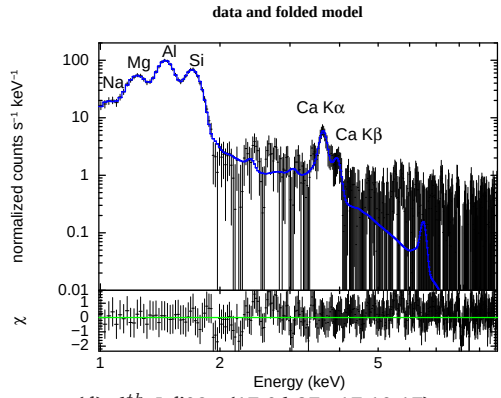

(d) 6^{th} Jul'09 - (17:06:27 - 17:10:17)

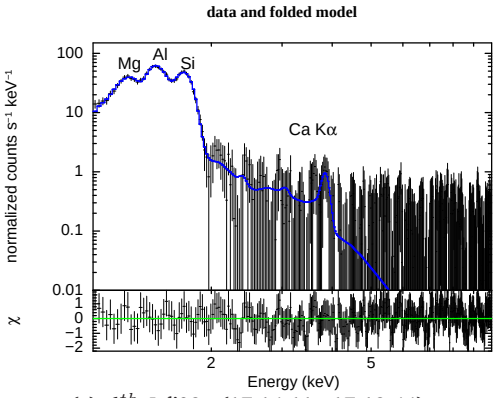

(e) 6^{th} Jul'09 - (17:14:11 - 17:19:44)

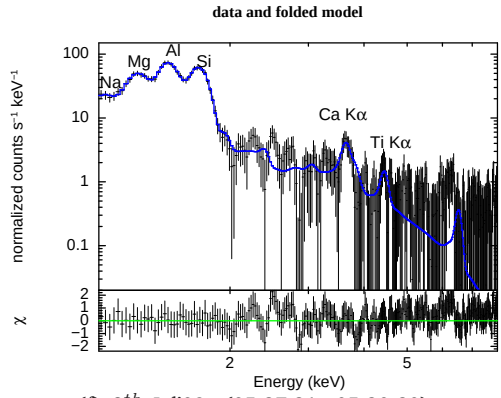

(f) 8^{th} Jul'09 - (05:27:31 - 05:30:20)

FIGURE 3.8: Best fits for different C1XS XRF spectra observed at different times with different solar flare conditions.

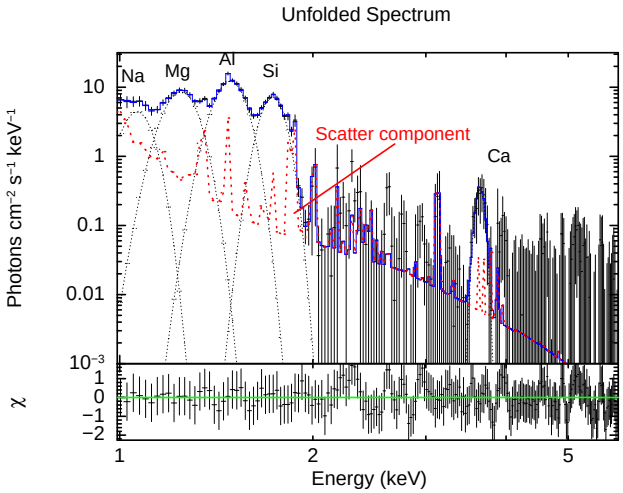

FIGURE 3.9: Best spectral fit to one of the C1 flare XRF data with scatter component modeled using vapec model in XSPEC. This plot also clearly confirm the evidence of Na XRF line from the Moon.

and also confirmed from Fig. 3.7(b), that the spectral profile of scatter component is equivalent to emission from a *collisionally ionized diffuse gas* with solar elemental abundances. Hence we used *vapec* (equivalent to vtherm_abund in OSPEX with which the solar spectrum is modeled) model in XSPEC, which incorporates **atomdb** database, to fit the scatter components (both solar lines and continuum). The best fit to C1 flare C1XS observation using *vapec* model, shown in Fig. 3.9 also ratifies the strong XRF line emission of Na from the Moon. Thus we have confirmed the unambiguous detection of Na by C1XS from the Moon and rule out its origin from the scattered component of solar spectrum. XRF line fluxes of the elements, including Na (wherever observed), determined for different flare observations are compiled in Table 3.2.

3.4.5 Corrections for Al filter

It was noticed that the presence of 0.4 μm thick Al filter in front of the detector could possibly contaminate the spectrum and yield excess counts at Al K-α (1.45 keV). The measured photon detection efficiency of SCD at Al K-α obtained from ground calibration was slightly larger than the nominal efficiency values (ie., scaled down theoretical curve; only at Al K-α, such as discrepancy was noticed) generated for lunar data analysis. As a

TABLE 3.2: X-ray line flux (photons/cm^2/s) from spectral analysis with 1 σ uncertainties. Approximate central co-ordinates of each ground pixel are given in the first column

Lat , Lon	**Date Time in UTC**	**Na Kα**	**Mg Kα**	**Al Kα**	**Si Kα**	**Ca Kα**
-45.2 , 25.0	04/07/09	-	0.54 $\pm$	1.03 $\pm$	0.83 $\pm$	0.08 $\pm$
	01:18:00 - 01:21:59	-	0.06	0.08	0.06	0.01
-30.2 , 25.0	04/07/09	0.72 $\pm$	0.83 $\pm$	1.59 $\pm$	1.06 $\pm$	0.06 $\pm$
	01:22:00 - 01:27:09	0.15	0.07	0.09	0.06	0.01
-63.2 , -10.5	06/07/09	-	0.92 $\pm$	1.54 $\pm$	0.94 $\pm$	0.18 $\pm$
	17:04:29 - 17:06:26	-	0.07	0.07	0.05	0.02
-53.2 , -10.5	06/07/09	0.56 $\pm$	1.26 $\pm$	2.10 $\pm$	1.46 $\pm$	0.12 $\pm$
	17:06:27 - 17:10:17	0.13	0.17	0.11	0.07	0.01
-43.0 , -10.5	06/07/09	0.73 $\pm$	1.30 $\pm$	2.08 $\pm$	1.31 $\pm$	0.04 $\pm$
	17:10:47 - 17:13:59	0.16	0.10	0.13	0.09	0.01
-30.7 , -10.3	06/07/09	-	0.88 $\pm$	1.40 $\pm$	1.08 $\pm$	0.02 $\pm$
	17:14:11 - 17:19:44	-	0.15	0.06	0.05	0.01
-30.0 , -28.7	08/07/09	0.45 $\pm$	0.73 $\pm$	0.92 $\pm$	0.42 $\pm$	0.03 $\pm$
	05:27:31 - 05:30:20	0.22	0.05	0.04	0.02	0.01

consequence, photon flux derived from the observed spectrum showed an enhanced Al line intensity. To account for this enhancement artifact, we used a correction factor (ζ) which is explained here.

- Number of incident photons entering into the detector at an energy (N_{photon}(E)) can be approximated as the number of counts (N_{count}) observed in the detector divided by the detector efficiency at that energy ($\epsilon(E)$) which is represented as :

$$N_{photon}(E) = \frac{N_{count}(E)}{\epsilon(E)} \tag{3.3}$$

- The difference in the measured and calculated values of detection efficiency at Al K-shell energy with respect to calculated value is considered as the correction factor ζ.

$$\zeta = \frac{\epsilon_{measured} - \epsilon_{calculated}}{\epsilon_{calculated}} \tag{3.4}$$

Using appropriate efficiency values from [*Narendranath et al.*, 2010], the correction factor is computed to be ≈ 0.13. This means that the Al line intensity derived from standard spectral fit is enhanced by 13%. Apart from this, charged particles around the Moon interacting with the Al filter could also produce PIXE which also enhances the Al signal and this contribution to the background was estimated to be $\approx$ 2%. Hence, we used the correction factor (ζ) as $\approx$ 15%, which is considered as an upper limit, which we applied to all Al XRF line fluxes derived from C1XS spectral fits.

3.5 C1XS Results - elemental abundances

XRF inversion algorithm *x2abundance* was used to convert the XRF line fluxes to elemental abundances. As mentioned in chapter 2, the code assumes a flat, homogeneous surface; however lunar regolith is made up of particles with mean size distribution from 40 μm to 130 μm [*McKay et al.*, 1991]. The observed XRF intensity could be affected by the particle size distribution, as the mean free path of soft x-rays is smaller than the mean particle size of lunar regolith. Laboratory experiments in [*Maruyama et al.*, 2008; *Näränen et al.*, 2008] show that XRF intensity decreases with increasing phase angles (angle between source-surface-detector) and increases with decreasing size of particles. However, this effect is expected to be small on C1XS results where the ground pixel dimensions are large (tens to hundreds of kms) and considers a large distribution of particle sizes.

The effect is further minimized with the use of flux-fractions (refer Eq. (2.4)). Due to lack of measurements of Ti & Fe, their abundances were kept frozen to the weighted average values derived from revised C1XS C3 observations. The derived abundances are to be considered as an average value over the area of observation defined by the large ground pixels and hence has limited scope to address the small scale spatial variations on the lunar surface. The derived elemental abundances along with 1 σ uncertainties are given in Table 3.3. C1XS with its good spectral resolution, observed clear, simultaneous signatures of major rock-forming elements from the Moon, including for the

TABLE 3.3: Elemental abundances (wt%) from C1XS analysis with 1 σ uncertainties

Lat , Lon	Na	Mg	Al	Si	Ca
-45.2 , 25.0	-	4^{+1}_{-1}	16^{+1}_{-1}	18^{+1}_{-1}	13^{+1}_{-1}
-30.2 , 25.0	3^{+1}_{-1}	4^{+1}_{-1}	17^{+1}_{-1}	17^{+1}_{-1}	10^{+1}_{-1}
-63.2 , -10.5	-	6^{+1}_{-1}	18^{+1}_{-1}	13^{+1}_{-1}	14^{+1}_{-1}
-53.2 , -10.5	2^{+1}_{-1}	6^{+1}_{-1}	17^{+1}_{-1}	16^{+1}_{-1}	10^{+1}_{-1}
-43.0 , -10.5	3^{+1}_{-1}	5^{+1}_{-1}	17^{+1}_{-1}	18^{+1}_{-1}	8^{+1}_{-1}
-30.7 , -10.3	-	4^{+2}_{-1}	16^{+2}_{-1}	23^{+3}_{-2}	8^{+2}_{-3}
-30.0 , -28.7	5^{+0}_{-1}	9^{+1}_{-2}	15^{+2}_{-2}	16^{+2}_{-1}	6^{+1}_{-1}
Average feldspathic meteorite compositions	0.26	3.26	14.92	20.89	11.65
AP16 (Soil & Regolith Breccia Average)	0.35	3.62	14.41	20.98	10.41
LP average (dashed box Fig. 3.3)	-	5.32	13.28	20.23	10.96

TABLE 3.4: Elemental abundances (wt%) re-derived with correction factor for C3 flare analysis with 2 σ uncertainties

Date & Time in UTC	Mg	Al	Si	Ca	Fe
05/07/09 07:12:50 - 07:13:22	6^{+1}_{-1}	15^{+1}_{-1}	21^{+1}_{-1}	8^{+1}_{-1}	6^{+2}_{-2}
05/07/09 07:13:23 - 07:13:55	6^{+1}_{-1}	15^{+1}_{-1}	19^{+1}_{-1}	8^{+1}_{-1}	8^{+2}_{-2}
05/07/09 07:13:55 - 07:14:27	6^{+1}_{-1}	14^{+1}_{-1}	21^{+1}_{-1}	8^{+1}_{-1}	7^{+2}_{-2}
05/07/09 07:14:27 - 07:15:00	6^{+1}_{-1}	13^{+1}_{-1}	19^{+1}_{-1}	9^{+1}_{-1}	9^{+1}_{-1}
05/07/09 07:15:00 - 07:15:33	3^{+1}_{-1}	15^{+2}_{-1}	18^{+3}_{-1}	8^{+2}_{-1}	12^{+1}_{-7}

first time direct evidence for the presence of enhanced sodium. Due to inadequate solar activity and reduced mission life, C1XS could not achieve its objective of global lunar elemental mapping. However, with the best available C1XS data, we have determined the elemental abundances for the sampled locations on the lunar surface. Through rigorous spectral analysis we have confirmed the unambiguous detection of XRF emission of Na from the Moon. Abundances derived for the 4^{th} and 6^{th} July data clearly exhibit

highland features with high Al and Ca abundances and low Mg abundance. The derived abundances for the 8^{th} July data with high Mg and Al clearly show components from both highland and mare regions.

3.6 Discussion on C1XS abundances

We have successfully demonstrated an independent method of deriving surface elemental abundances from remote sensing XRF spectroscopy that takes into account differences arising from lack of standard laboratory conditions. Elemental abundances derived from the LP GRS, for a large area encompassing regions observed by C1XS (see dashed box in Fig. 3.3), are compared with abundances derived from C1XS for the same regions in Fig. 3.10(a). We have applied the correction factor for the Al filter to our earlier published C3 flare data and re-derived the elemental abundances, which are also included in the plot. Fig. 3.10(a) shows that C1XS compositions along with 1σ uncertainties match well with the distribution of abundances derived from remote sensing gamma-ray observations. Results from two different independent studies in different energy bands clearly establish consistency and complementary nature of these observations. These results clearly demonstrate the capability of our inversion approach to well constrain the derived abundance values.

For comparison, we have included the average composition of lunar soils from Apollo 16 mission [*Haskin & Warren*, 1991] and the average feldspathic highland terrane composition from lunar meteorites [*Korotev et al.*, 2003] in Table 3.3. It is evident that the derived abundances of Na (> 1 wt%) are larger than what has been known so far (<1 wt%). All C1XS observed regions discussed in this thesis are on near-side lunar highland areas from where no samples have been returned. It is clear that C1XS derived abundances do not agree well with average lunar soil compositions (Apollo 16) which are studied in great detail in laboratory, at finer spatial scales. It is also evident that the elemental abundances derived from remote-sensing C1XS and LP GRS experiments with wide spatial scales agree well within the derived uncertainties. We attribute the

variation in C1XS derived abundances to reflect the average compositional diversity on lunar surface especially on lunar highlands.

According to our present understanding of highland region from the lunar returned samples and meteorite collections, there exist a strong positive correlation between Al and Ca abundances as shown in Fig. 3.10(b)(i) [*Demidova et al.*, 2007]. C1XS results also show an increase in Ca with increase in Al. However, they do not agree with the established correlation from lunar meteorite samples, which are mostly anorthite ($CaAl_2Si_2O_8$). Further, it is also found that the derived Ca abundances are lower for those intervals where Na is observed. It is expected that increase in Na abundances should correspondingly decrease Ca and Al abundances. The relation between Na and Al abundances from C1XS results (Fig. 3.10(b)(ii)) could not be well established due to limited data points with large uncertainties. However, our results seem to suggest an inverse relation between Ca and Na abundances Fig. 3.11.

3.6.1 Lunar observations & Magma Ocean Theory

Sodium (Na) is a moderately volatile element and is considered to be lost during the early formation and evolution of the Moon via the giant impact event (refer LMO theory sec. (1.2.1)). As a result, the primary highland crust of the Moon is expected to be rich in calcic plagioclase. The amount of sodium content present in the Apollo lunar samples and feldspathic lunar meteorites clearly portray this scenario. Spectral measurements from MI and SP instrument onboard SELENE [*Ohtake et al.*, 2009] and M^3 in Chandrayaan-1 [*Donaldson Hanna et al.*, 2014], indicated wide distribution of pure ferroan anorthosite (An_{94-98}) on the highland crust. This clearly supports the LMO theory and advocates single global differentiation. It should be noted that the experiment was operated in the near infra-red (NIR) region where plagioclase with minor amount of iron content exhibit a broad absorption band centered around 1.25 μm owing to the electronic transitions of minor amounts of Fe^{2+}. However, NIR spectroscopy is less sensitive to An# and hence cannot address the presence of calcic and sodic content in plagioclase feldspar.

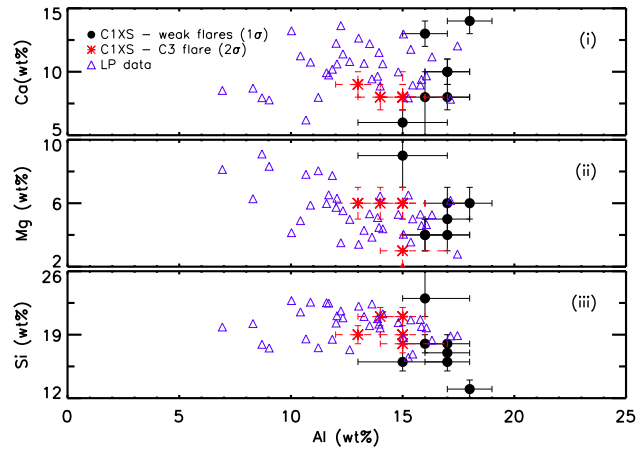

(a) Distribution of abundances from C1XS and LP

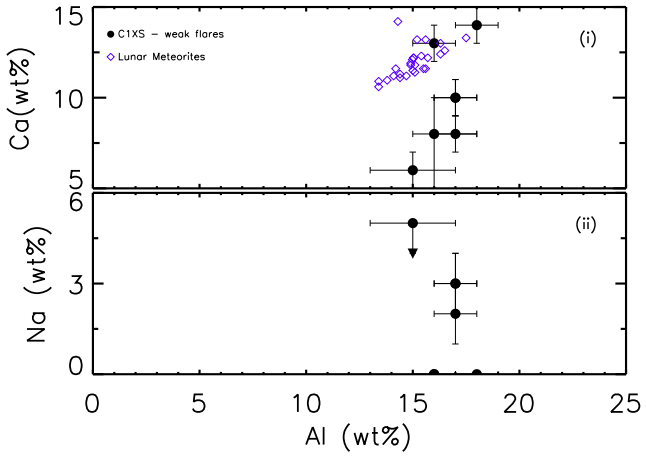

(b) C1XS abundances and Lunar Meteorite abundances

FIGURE 3.10: Comparison of C1XS abundance with (a) GRS data from Lunar Prospector [*Prettyman et al.*, 2006]. (b) Lunar Meteorite compositions ([*Demidova et al.*, 2007]). Variation of Ca and Na abundances with respect to Al (i & ii) with abundance of Ca increasing with Al which do not agree with the established correlation in lunar meteorite collections.

Thermal Infrared (TIR) spectroscopy has been extensively used in laboratory to study the variations in plagioclase minerals (An#) [*Donaldson Hanna et al.*, 2012]. Detailed analysis using the well-studied Christiansen Feature (CF) around 8μm, Diviner radiometer onboard LRO identified intermediate plagioclase compositions [*Greenhagen et al.*, 2010; *Kusuma et al.*, 2012] on the Moon (refer TIR spectroscopy sec. (1.4.1)). Fig. 3.12 shows the over-plot of C1XS observed regions on the LRO diviner CF value map. C1XS observations discussed here are likely to be dominated by the impact ejecta and disturbed regolith due to the young impact crater Tycho. It is clear that some of the regions

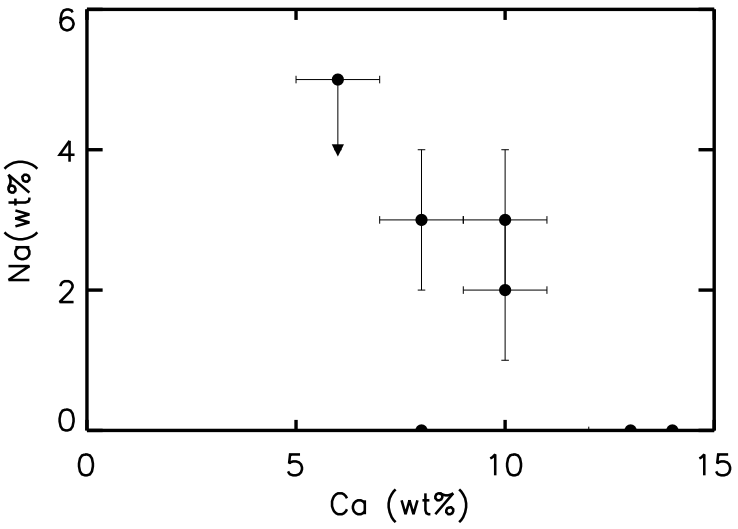

FIGURE 3.11: Relation between Ca and Na from C1XS observations

observed by C1XS were noted to have unusual mineral compositions (saturated blue regions locations on LRO image *Greenhagen et al.* [2010]). Poor spatial resolution in our x-ray results did not permit us to perform cross comparison with the Diviner CF values which was mapped with sub-km spatial resolution. Also, lack of Fe measurements due to weak flares did not permit to map the Mg content (Mg #) from our observations. The An# value derived from C1XS abundances vary between An_{55} to An_{83} which correspond to compositions such as labradorite and bytownite. C1XS results with high Na content contradict the extreme loss of volatiles by vaporization. However, there exist physical processes which do not require alkali depletion of the bulk Moon [*Nekvasil et al.*, 2013]. It was also shown by Nekvasil et al., [*Nekvasil et al.*, 2013] that the Moon can have intermediate plagioclase composition under different temperature and pressure conditions. Evidences are also seen in Diviner images showing unusual compositions over relatively young impact crater. First results from the Ultraviolet-Visible Spectrometer (UVS) onboard LADEE (The Lunar Atmosphere and Dust Environment Explorer) measured spatial and temporal variations of Na flux in the exosphere [*Colaprete et al.*, 2014]. Associations with surface compositions, meteorites etc., are being examined.

Our understanding of higher levels of sodium abundances on the lunar surface is still incomplete. Surface elemental abundances derived from limited C1XS observations raise

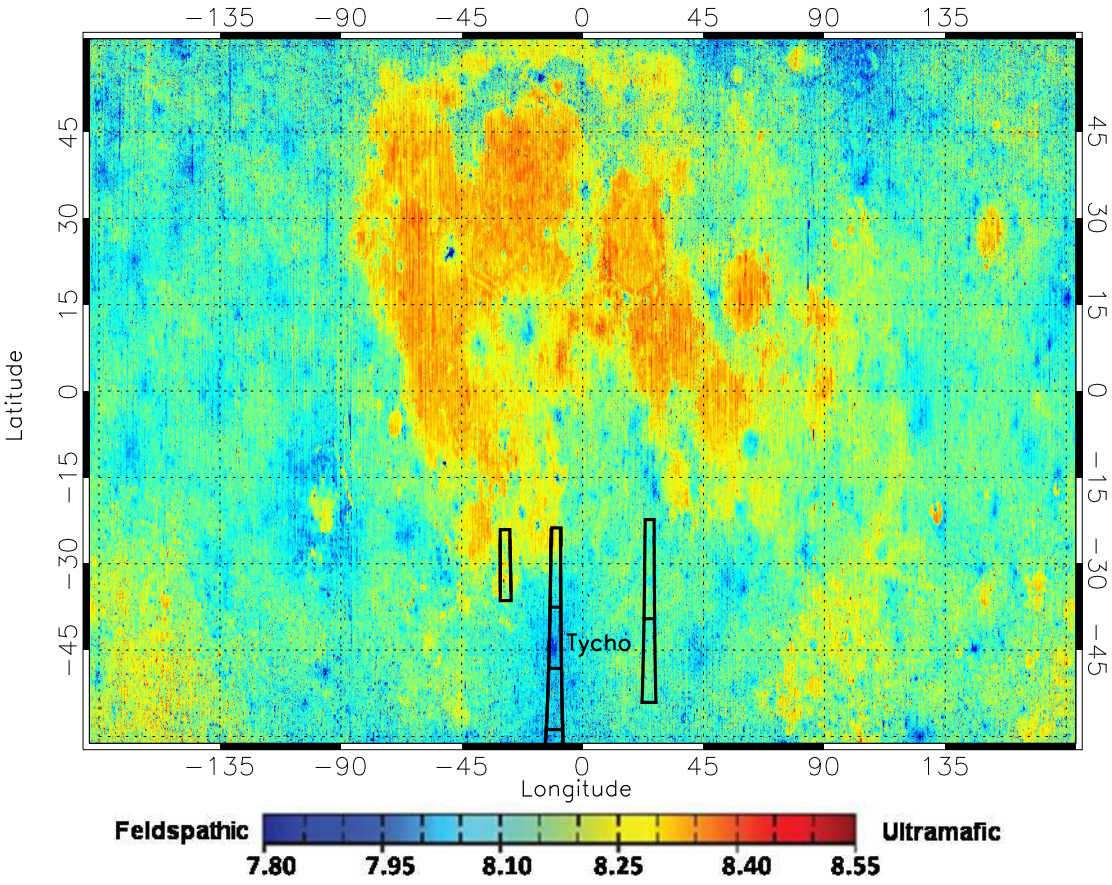

FIGURE 3.12: Track of C1XS observed region on the Moon - 4^{th}, 6^{th} and 8^{th} July 2009 plotted over the LRO Diviner radiometer Christiansen Feature (CF) value map (in μm). Ca-rich plagioclase have CF positions around 7.84 μm whereas plagioclase with Na component shift towards low CF values ($\leq$ 7.8 μm). Mafic minerals such as pyroxene, olivine show long CF values as indicated in the color map. Some of the saturated blue regions in the map with lower CF values represent unusual compositions [*Greenhagen et al.*, 2010].

the following questions :

- Can large amount of sodium be still present on the lunar surface?
- What causes the enrichment of volatile element Sodium on the lunar surface? Variable thermal cooling of early magma or secondary processing of lunar surface?
- Is the observed sodium enrichment on the lunar surface a local effect or suggestive of wide-spread enhancements?
- How are the elements Ca and Na distributed on the lunar surface?

- Compositional analysis of lunar samples, meteorites and soil does not show any relation between Ca & Na abundances. Whereas C1XS abundances suggest an anti-correlation (R = -0.89) between Ca & Na. Can loss in Ca abundance lead to enhanced Na?

To answer all these questions, good measurements of elemental abundances with finer spatial resolution for the entire lunar surface are required. Simultaneous measurements of Ca & Na abundances along with other rock-forming elements can provide more insights to the formation and thermal evolution of the Moon. To complete the science goals left behind by the C1XS experiment, an improved spectrometer is being designed for the next Indian Moon mission, Chandrayaan-2. CLASS experiment will have enhanced sensitivity from device level improvements in detectors.

3.7 Improvements in the CLASS instrument

1. Detector area : It is seen that majority of C1XS observations were made during weak solar flares where averaging was performed across multiple, adjacent ground pixels to generate a statistically significant XRF spectrum (ie., spectrum with prominent XRF lines over the background). Large area x-ray detectors provide large photon collection area which will help to generate lunar elemental maps even during weak flares, preserving the finer spatial information. CLASS instrument will be equipped with 16 x-ray detectors with each of geometric area 4cm^2, which will provide enough sensitivity even during low intensity flares (A class and above).

2. Choice of Detector : C1XS experiment used 3-phase clocked SCD (CCD-54), whereas CLASS uses 2-phase clocked SCD (CCD-236). Both the detectors have similar architecture in terms of diagonal clocking, pseudo linear readout, dead layer, field and epitaxial layers. Major difference between the two is in the pitch of the channel stop where the former had a 25 μm pitch while the latter has 100 μm pitch. The large pitch in CLASS detectors effectively reduces number of split events which mitigate low energy tailing and hence a more complete charge collection.

3. Instrument response : Interaction of x-ray photons in a Si- based detector result in different spectral features due to multiple cascade processes that happen between charge generation and charge read-out. C1XS was operated in the energy range 1 - 20 keV with low energy threshold at ≈0.8 keV. It followed different event filtering (refer sec. (3.2.2)) techniques for different event rates which further complicates the shape of the observed spectrum. Response matrix of C1XS instrument was constructed based on the calibration data derived at a few sparsely-spaced mono-energetic x-ray energies between 2.3 and 8 keV. Various spectral features seen in the observed calibration spectra were modeled empirically; each spectral component was modeled to derive energy-dependent shape interpolation throughout the entire energy range of the detector. A detailed physical model for the charge transport in x-ray detectors for CLASS will help in better understanding of the device level interactions. Physical understanding of detectors' response at all energies, especially at low energies (≈ 1 keV) and around Si K-edge (≈ 1.8 keV), will improve confidence in spectral modeling. This will allow us to determine precise elemental line fluxes and hence elemental abundances with reduced uncertainties. A physical model (discussed in chapter 4) is well suited to optimize event selection logic, maximize event recovery and hence improve capability to better model the spectral response of CLASS detectors.

3.8 Conclusion

To conclude, the C1XS experiment performed extremely well and proved its capability by observing the XRF lines of rock-forming elements from the Moon. C1XS observed simultaneous measurement of Mg, Al, Si, Ca, Ti & Fe including Na for the first time. It provided the first confirmation of enhanced Na content on the lunar surface. However, C1XS could not provide a global elemental picture of the Moon due to lack of adequate solar flare observations and short life time of the mission. The derived abundance of Na from C1XS data is larger than what has been known from earlier studies. Lunar surface compositions derived from C1XS measuring the enhanced sodium content, raised many questions regarding the evolution of the Moon. These results demand more precise Ca

and Na abundance measurements on a global scale to address the thermal evolution of the Moon. Thus study of Na abundance on the lunar surface is very important; it can be studied qualitatively and quantitatively in x-rays and also simultaneously with other rock-forming elements. With the large area detectors and detailed charge transport model for spectral response, the upcoming CLASS experiment is designed to continue precise global elemental mapping and unravel the mysteries of the Moon formation.

3.9 Summary

In this chapter, we have summarized the results from all observations made by the C1XS experiment. We extracted the first direct evidence of Na from the lunar surface and found that the derived abundance of Na is larger than what has been known from earlier studies. We also discuss specific lunar science questions raised by these results which add to the science goal of upcoming CLASS experiment. At the end of this chapter, we briefly describe device level improvements in the CLASS instrument and address the importance of charge transport model for SCDs. In the following chapter, we present the formulation of charge transport model developed for SCD along with results from validation tests using C1XS ground calibration data.

Chapter 4

Charge transport model for a Swept Charge Device (SCD)

In chapter 3, we discussed the results and scientific insights from C1XS observations and listed out possible improvements for the upcoming CLASS experiment. In this chapter, we present the algorithm and implementation of a Monte Carlo based charge transport model to simulate x-ray photon interactions and resulting charge propagation in Swept Charge Devices (SCD). The model aims to better understand device level processes and predict the nature of spectral redistribution function (SRF), when charges are collected by fixed anodes. Through comparison of simulation results with C1XS ground calibration data, we demonstrate our ability to reproduce all prominent features seen in the calibration spectra in the simulated spectra.

4.1 Introduction to X-ray CCD

Charge Coupled Devices (CCD) are essentially two dimensional x-ray sensors, which contain a Metal-Oxide-Semiconductor (MOS) structure. Its architecture consists of a heavily doped substrate, a lightly doped epitaxial layer in which a buried channel is implanted to form a p-n junction and gate electrodes with insulating layers. It also contains channel stops which are created for charge isolation using heavily doped p+

silicon along one direction. Further details on the fabrication of x-ray CCDs can be found at *Gow* [2009].

4.1.1 Buried channel potential

In n-type buried channel CCD, a p-n junction is formed with the p-type epitaxial layer. The field potential due to this p-n junction is adjusted with the MOS structure to form a resultant potential which is maximum in the buried channel beneath the Si-SiO_2 interface and above the p-n junction. A sketch of potential well profile of buried channel x-ray CCD is shown in Fig. 4.1. This device is usually operated in two modes viz.,

1. Collecting mode : A positive bias gate voltage is applied with respect to substrate voltage (V_{SS}) during which charge transfer process occur.
2. Inversion mode : Accumulation of holes at the surface of gate electrodes occur when 0V is applied to gates. This suppresses the generation of dark noise which is called 'pinning'

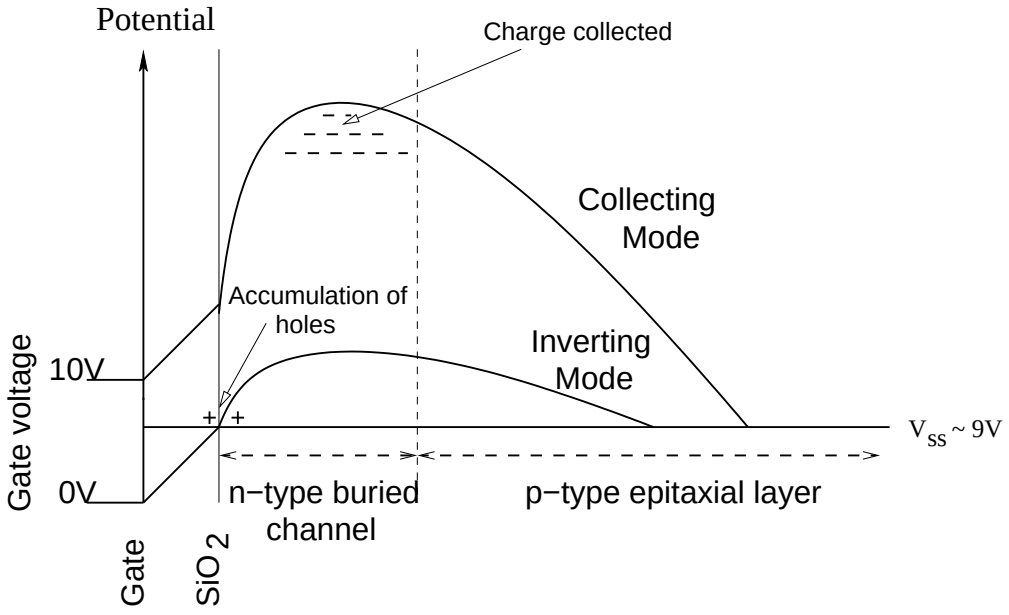

FIGURE 4.1: Buried channel potential profile of CCD (adapted from J.P.D. Gow, 2009, Phd thesis)

4.1.2 CCD structure and readout

A conventional CCD consists of electrodes which are arranged in rows and columns. Pixels are considered to be formed with two/three electrodes which are called as '*two or three phase devices*'. When exposed to photons, charges are generated and are collected in the buried channel. Charges produced in the device always reach the nearest deepest potential well. This phase is called *Collecting phase* or *Image integration*. When an exposure ends, the electrons collected in the array of pixels are transported within the device through the cyclic application of voltages to gate electrodes which enables the *readout phase*. Through parallel clocks (Iϕ1, Iϕ2), charges are shifted to the readout section of the CCD, from where charges are read out using sequential clocks (Rϕ1, Rϕ2). The resultant 2D output preserves information of photon incidence position on the device.

4.2 Principles of operation

4.2.1 X-ray interaction

When x-ray photons travel through a medium of density (ρ), it undergoes an exponential attenuation. Different processes by which interactions occur have a fixed probability per unit length in the path of its motion, which are collectively termed as absorption coefficient. The intensity of transmitted x-rays (I_{trans}) through a material of density ρ (g/cm^{-3}) and thickness t is given by :

$$I_{trans} = I_0 e^{-\mu_m(E)\rho t} \tag{4.1}$$

where I_0 is the initial x-ray intensity, μ_m (cm^2/g) is the mass absorption coefficient which depends on the energy of the photon and the material density. X-ray photons can interact with matter via three important processes viz., photoelectric effect, Rayleigh scattering and Compton scattering. Photoelectric effect is the predominant process by which soft x-ray photons interact in Si-based x-ray detectors.

4.2.2 Charge generation

In photoelectric process, energy of the incident photon is completely transferred to a bound electron and the electron is ejected out from the atom. The ejected photoelectron with large kinetic energy (hν - ϕ ; ϕ - binding energy of atomic shell) produces further ionization causing cloud of charges ie., electron-hole (e-h) pairs. The charge cloud thus generated is collected in the potential well beneath the detectors' surface. The number of e-h pairs created by an x-ray photon is related to its energy by :

$$n_{e-h} = \frac{E_{h\nu}}{\omega} \tag{4.2}$$

where $E_{h\nu}$ is the energy of incident x-ray photon; ω is the average energy required to produce an e-h pair. For Si at room temperature (300K), ω is 3.65 eV, whereas the band gap energy is 1.1 eV. The reason for ω being larger than the band gap is that, all ionization events do not yield e-h pairs. Some of the energy is transferred through lattice vibrations (thermal release), leading to phonon production. Due to transfer of energy to silicon lattice, the incident photon's energy is not completely converted to e-h pairs. As a result, the variance in the number of e-h pairs generated due to photon interaction is less than the statistically predicted Poisson variance which is described by the Fano factor [*Fano*, 1947] which is given by :

$$F = \frac{\sigma^2}{n_{e-h}} \tag{4.3}$$

$$\sigma_{Fano} = \sqrt{F_{Si}\, n_{e-h}} \tag{4.4}$$

4.2.3 Charge transportation

Charge packets collected in potential wells are transferred by applying suitable voltages to gate electrodes. Transportation of charges through manipulation of voltages is called '*clocking*'. In this way charge packets are transferred from one pixel to another. Pictorial representation of clocking in a 2 phase CCD (ie., one pixel comprises of 2 electrodes) is shown in Fig. 4.2. Transfer of charges between electrodes during clocking should ideally

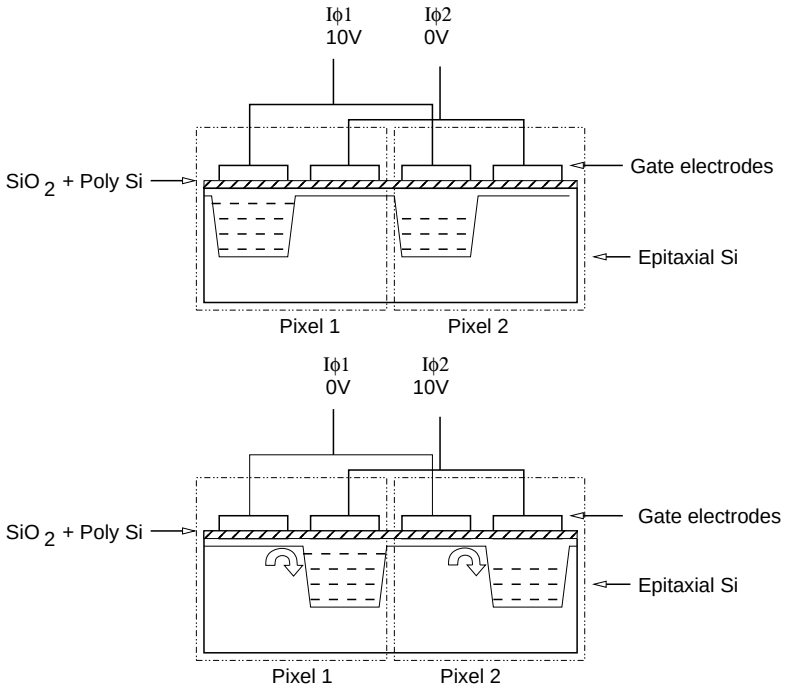

FIGURE 4.2: Schematic representation of clocking operation in a two phase CCD

be carried out perfectly with complete charge transfer. Any amount of charge loss will lead to degradation in the performance ie., in spectral and/or imaging properties of the device.

4.3 Swept Charge Devices (SCD)

A brief outline of SCD, a novel Si-based soft x-ray detector is given in sec. (3.2.1). A comparison of SCD with conventional 2D x-ray CCD is summarized in Table 4.1.

4.4 SCD structure and readout

The architecture and working principle of an SCD is similar to a conventional x-ray CCD, where clock voltages are applied for charge transportation. However, the mode of clocking and readout design is different from 2D CCDs. SCDs are in general operated in continuous clocking mode at high frequencies (≈100 kHz) [*Gow*, 2009]. The term 'pixel'

TABLE 4.1: Comparison of conventional CCD and SCD

	2D CCDs	SCDs
Collection Area(per unit)	Small	Large
Read out	2D	Pseudo linear
Clock requirement	More clocks than SCDs	Minimal clocks
Pixel size	Equal sized	Different size 'pixels'
Functionality & Spectroscopy	Imaging (with optics)	Mainly for spectroscopy
Typical operation	Long integration	Continuous readout
Temperature & spectral capability	Good resolution @ low temperature (≈-40 °C)	Good resolution @ moderate temperature (≈ -20 °C to 5 °C)

which refer to the unit of photon interaction co-ordinates on the device in conventional CCDs, is not strictly applicable for SCDs. We refer to the photon interacting region on the device as '*elements*' which are shown in Fig. 4.3. These *elements* in each electrode are analogous to pixels in 2D x-ray CCDs. In SCDs, charges collected in each *element* in different electrodes are clocked towards the central channel and then clocked down to reach the readout node (arrows in Fig. 4.4 and 4.5 indicate direction of charge flow). Charges collected from the *elements* in each electrode take same number of clocking steps to reach the readout node where they are merged to give a pseudo linear output. It is because of the design of diagonal clocking, SCDs are not position sensitive devices. We refer the combination of charges from these *elements* at the readout node as '*samples*'.

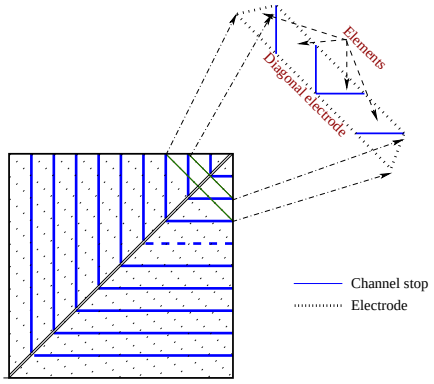

FIGURE 4.3: Representation of elements in a diagonal electrode of SCD CCD54. Filled regions in the zoomed electrode are the elements which are separated by channel stops.

4.4.1 C1XS - SCD CCD54

The structure of SCD CCD54 used in C1XS is shown in Fig. 4.4. The active area of 1.07 cm^2 contain 1725 diagonal silicon electrodes with the channel stops arranged in a herringbone structure. The pitch of the channel stops is 25 μm. CCD54 is a three phase device and require 575 clock triplets to completely flush the device. As explained above, charges generated due to photon/particle interaction will be clocked diagonally and combined at the readout node.

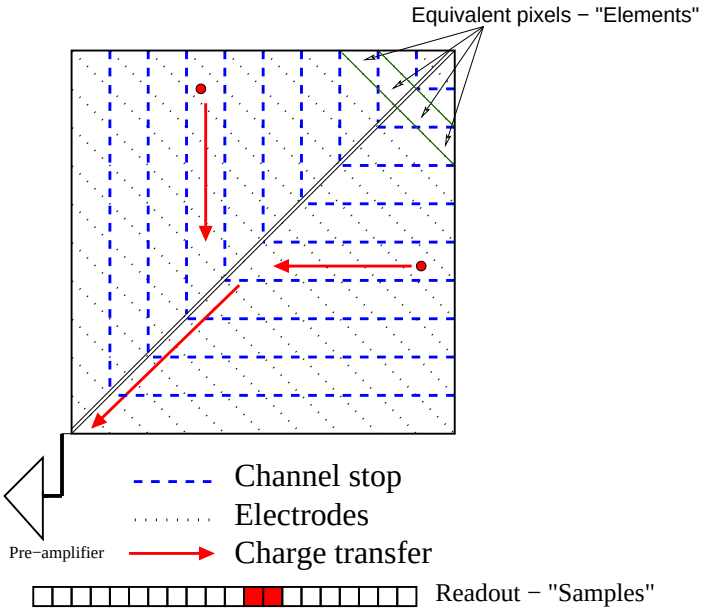

FIGURE 4.4: Schematic view of the SCD CCD54 used in C1XS

4.4.2 CLASS - SCD CCD236

The CLASS experiment uses SCD CCD236 whose structure is shown in Fig. 4.5. With quad architecture this device provides an active area of ≈ 4 cm^2. The SCD CCD236 is designed to have rectangular silicon electrodes in contrast to the diagonal electrodes in CCD54. CCD236 is a two-phase device with a pitch of 100 μm. Charge collection via diagonal clocking using the combination of two central readout channels is similar to CCD54. Further, charges collected from all four detectors are merged at the readout node to give out a single output.

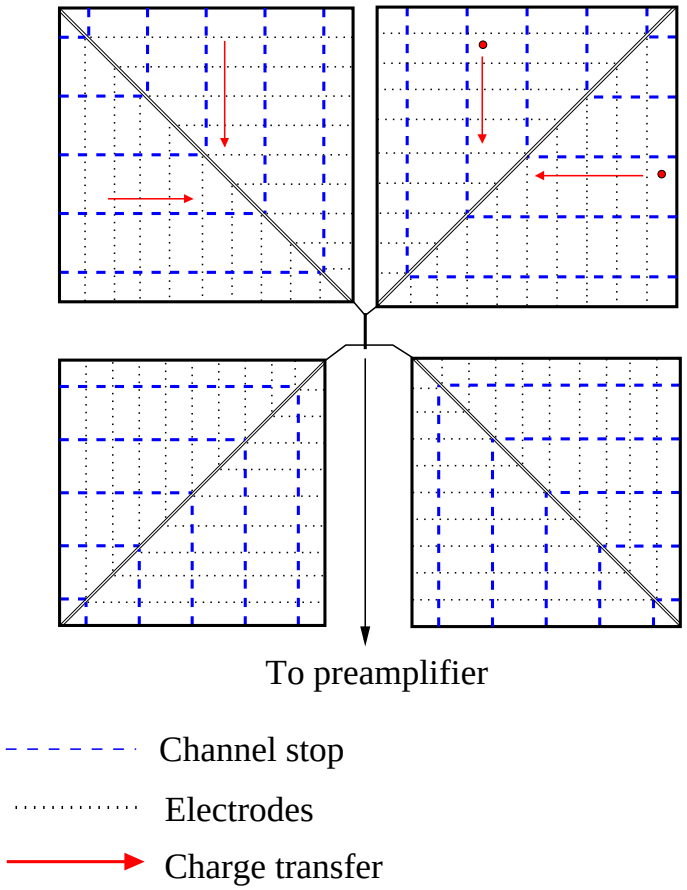

FIGURE 4.5: Schematic view of the SCD CCD236 being used in CLASS

4.4.3 Advantages of SCD

- Less number of clocks are required to readout the entire device which reduce readout complexity and power consumption
- Fast readout ($\approx$ 100 kHz per sample) offered by the electrode design with reduced number of clocks over large charge collection area minimizes dark current generation
- Dither mode clocking suppresses surface generated dark current and continuous clocking (ie., avoidance of long integration period) avoids additional dark current accumulated during long integration
- Continuous clocking allows the device to be used effectively even during higher incident x-ray flux

4.5 Motivation for charge transport model

The objective of CLASS experiment is to map the elemental abundances of elements on the surface of the Moon. Quantitative study of Na abundance on the lunar surface will be one of the prime science objectives of the CLASS instrument. X-ray detectors with good sensitivity and spectral resolution with moderate power requirement are required to spectrally resolve the closely-spaced lunar XRF lines Na (1.04 keV), Mg (1.25 keV), Al (1.48 keV) and Si (1.75 keV) and estimate line fluxes. Since elemental abundances are determined from observed XRF line fluxes, the derived line fluxes should have minimal uncertainties. Thus the accuracy of results depend on our detailed understanding of the instrument and constructing realistic detector spectral response from calibration data. A physical model incorporating the physics of transport of charges in a device whose physical structure is known, provides complementarity to the calibration data as well as enables tuning of the device operation and event selection for optimal performance.

4.5.1 Challenges in the calibration of soft x-ray detectors

1. Calibration of x-ray detectors at low energies ≤ 1 keV is challenging due to :
   - Lack of standard radioactive sources in this energy range.
   - Absorption of low-energy x-ray photons in air (need vacuum environment).
   - Discontinuities caused by absorption edges (eg., K-shell absorption edge : silicon (at 1.84 keV), oxygen (at 0.54 keV) and nitrogen (at 0.39 keV)).
   - Charge variations in energy-dependent system efficiency.
2. The steep decrease in intrinsic detection efficiency of soft x-ray detectors at these energies demand high intensity stable x-ray sources.
3. Determination of x-ray detection efficiency of the detector is straightforward, provided the beam energy and its absolute intensity are well calibrated. Usually, the x-ray beam intensity would be first calibrated using standard reference detectors (say Si-PIN or Si(Li) detectors), for which the detection efficiency is known/easier

to model. Then, using the same beam we irradiate the target detector to be calibrated to get relative efficiency with respect to the reference detector. The absolute efficiency of the target detector is determined using the known efficiency of the reference detector. However, it is not easy to get the absolute efficiency of the reference detector at these low energies. Losses in dead-layers, filters and windows of reference detector contribute to uncertainties in determining the absolute efficiency of target detectors.

The observed x-ray spectrum (in counts) is a manifestation of incident photon spectrum convolved with the spectral response of the detector. To precisely derive the amount of photons emitted by each element from the Moon, proper calibration of detection efficiency and spectral response is essential. Our aim of developing this model is to support the calibration tasks, for the forthcoming CLASS experiment, such as generation of spectral response matrices, estimation of efficiency, optimization of event selection logic and maximizing event recovery to improve the overall efficiency. Detailed physical model for the charge transport will help in better understanding the device level interactions.

4.5.2 Spectral Redistribution Function (SRF)

Interaction of an x-ray photon within a detector results in a complex cascade of energy transfers. Energy deposited by the photon gets transformed in many ways leading to various signatures in the observed energy spectrum. The distribution of all energy deposits above a noise threshold observed in a device for an incident mono-energetic photon is called the spectral redistribution function (SRF). In a SCD, charges collected from photon interactions are further processed for event recognition to obtain the pulse height spectrum. Hence, the observed SRF of SCD is a function of energy of the incident photon, the event selection logic and threshold values. This model can help in optimizing threshold values which are important to select/reject split events. It can also identify the genesis of different features seen in the observed SRF and enables quantification of different process components and in principle contribute to application-specific optimization of device configuration.

4.6 Ground calibration of the SCD in C1XS - An overview

Extensive ground calibration was carried out for all C1XS detectors. It achieved a spectral resolution of 153 eV at 5.9 keV in-orbit (as compared to 143 eV on ground). SRF of SCDs were obtained using a double-crystal monochromator in the RESIK x-ray beamline at Rutherford Appelton Laboratory (RAL), UK. The mono-energetic beam was further collimated using a rectangular slit of 1mm $\times$ 2mm dimension, illuminating only a small portion of the SCD. The following distinct mono-energies viz., 2.29 keV, 4.51 keV, 5.514 keV, 6.93 keV and 8.04 keV were chosen using different target anodes (Mo, Ti, Cr, Co, Cu) in the x-ray generator. Also measurements were carried out over a range of operating temperatures from -30 °C to 0 °C. These calibration data were then filtered using a two-threshold logic explained in chapter 3 (refer sec. (3.2.2)). The following are the prominent features seen in the filtered calibration data *photopeak, low energy shoulder, low energy tail, cut off, escape peak and low energy rise*. Further, it was also observed that these features exhibit energy dependence.

For C1XS, the spectral response matrix was constructed using the above calibration data. Spectral features were modeled empirically using appropriate mathematical functions (without any connection to physical processes). The derived parameter values were interpolated to establish a matrix covering the entire energy range. The efficiency of detectors were derived using the spectral response generated from the calibration data. As the instrument did not suffer from any degradation, the response matrix generated from the ground calibration data was adequate for in-orbit data. Further details on the ground calibration of C1XS instrument can be found at *Narendranath et al.* [2010].

4.7 Charge transport model for SCD

Here, we explain the algorithm of charge transport model developed to simulate x-ray photon interaction and charge propagation in SCDs. A flowchart explaining the algorithm is shown in Fig. 4.6. Vertical structure of the SCD modeled here is shown in Fig. 4.7 where different layers are labeled with respective dimensions. The dead

layer $\approx$ 1.5 μm thick, consists of SiO_2, Si_3N_4 and a polysilicon layer. Only a negligible fraction of x-ray photons interact in the dead-layer and a tiny fraction of it result in charge production and subsequent collection. Hence, we modeled it as a single block of SiO_2 layer from which no charges are collected. The bulk substrate is a heavily doped p+ region, where charges suffer huge losses due to recombination and hence considered to be lost. The following are the fundamental assumptions considered in the model :

- Si-based x-ray detector is assumed to be ideal, free from interstitial defects and impurities
- The electric field is assumed to be present only perpendicular to the plane of the detector
- The acceptor impurity concentration in the field-free zone is assumed to be same as in the field zone.
- The boundary between field and field-free zone is modeled with a small offset to avoid numerical divergence (at $z_0 = d_d$ refer Eq. (4.13))

4.7.1 Photon interaction & Initial charge cloud

Mono-energetic x-ray photons are allowed to illuminate the SCD at random positions (x, y) with uniform probability. Photons are considered to impinge on the SCD at normal incident angle with respect to the plane of the device. These photons travel through different layers of the detector before interaction. The distribution of depths at which interaction occur inside the SCD is computed using :

$$z_0 = \frac{1}{\mu(E)} ln(R_u) \tag{4.5}$$

where μ(E) - linear mass absorption coefficient of the material (cm^{-1}) at photon energy E, R_u - random number with uniform distribution. If the interaction depth (z_0) is greater than the thickness of a layer, then the interaction depth is re-computed for the material in the following layer. In this way, number of photons interacting in the dead-layer

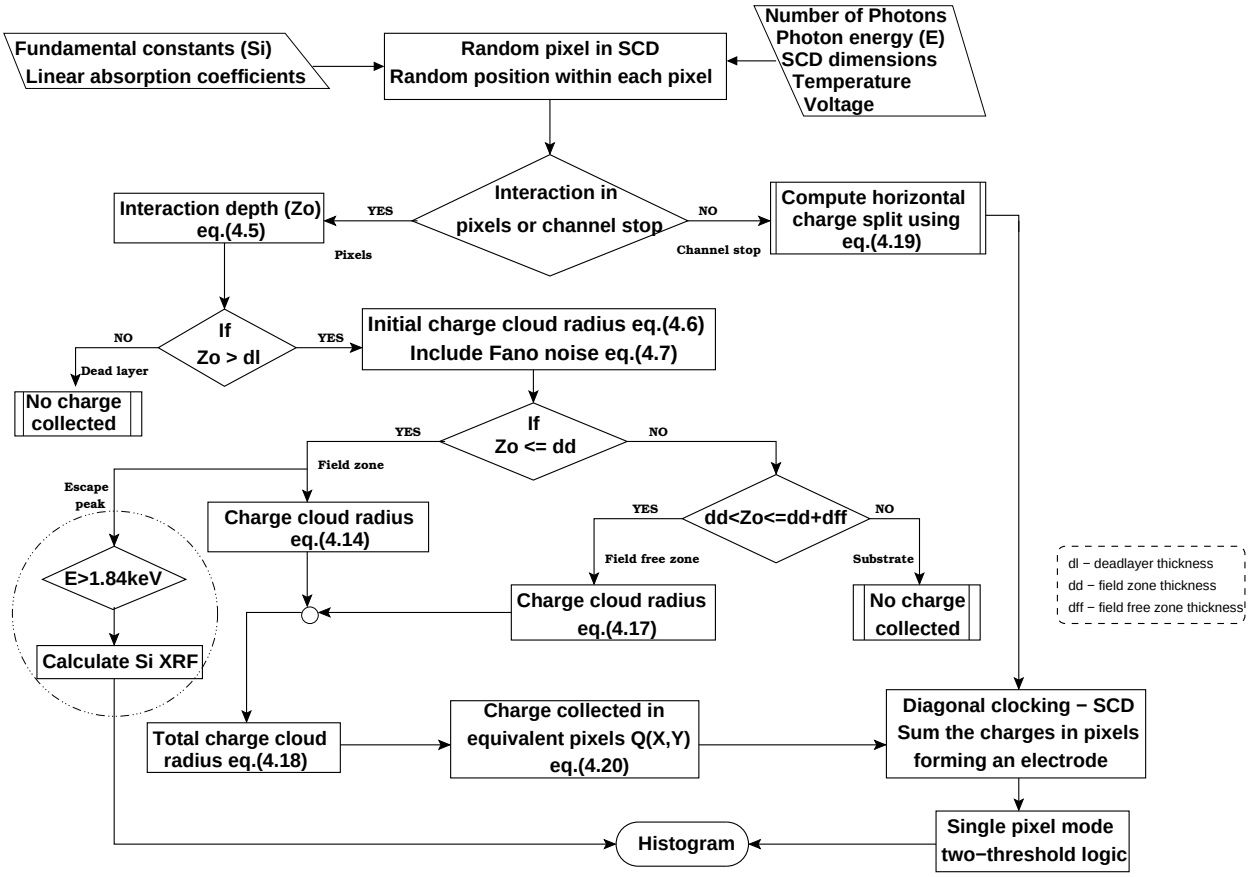

FIGURE 4.6: Flowchart of the charge transport model to simulate the SRF of the SCD. Some of the important steps involved in the model are arranged in sequence.

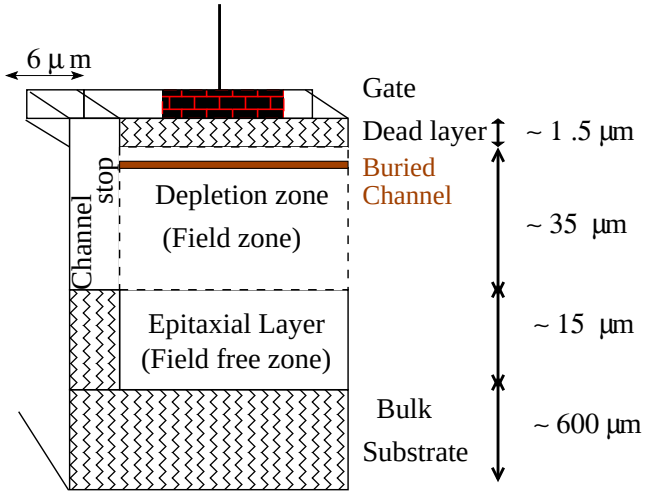

(Figure drawn not to scale)

FIGURE 4.7: Vertical structure of the SCD CCD-54 used in C1XS

and substrate layer are included in the simulation as energy loss and not stored. Soft x-ray photons interact via photoelectric process and produce a charge cloud (refer sec. (4.2.2)), which is assumed to be spherical in shape. The radial charge distribution of this spherical cloud is assumed to follow a Gaussian distribution with 1σ radius given by *Kurniawan & Ong* [2007]:

$$r_i = \begin{cases} 40.0\frac{E_{pe}^{1.75}}{\rho} & (5\ keV < E_{pe} < 25\ keV) \\ \\ 30.9\frac{E_{pe}^{1.53}}{\rho} & (E_{pe} \leq 5\ keV) \end{cases} \tag{4.6}$$

where ρ - density of the detector material (ρ = 1.86 g/cc for Si), E_{pe} - energy of the photoelectron. This represent that charges are concentrated towards the center of the sphere and falls off with radius; abruptly truncates to zero at the cloud boundary given by Eq. (4.6). While estimating the number of charges produced due to absorption of an x-ray photon, Fano noise [*Fano*, 1947; *Owens et al.*, 2002] appear, which is incorporated as :

$$E_f = E_i + R_n(0)\sqrt{F\omega E_i} \tag{4.7}$$

where E_f - photon energy with Fano noise added, $R_n(0)$ - normally distributed random number with mean 0 and variance 1, F - Fano factor and ω - average energy required to produce an e-h pair. The initial charge distribution is (Q_0) is obtained from this final energy (E_f) as :

$$Q_0 = \frac{E_f}{\omega} \tag{4.8}$$

Interaction of x-ray photons in SCDs can be broadly grouped into three viz., *Field zone interactions, Field-free zone interactions and Channel stop interactions*. The escape peak appears as a consequence of x-ray photon interaction which also needs to be incorporated.

4.7.2 Interaction in Field zone

Photons interacting at depths within the depletion zone (d_d) are termed as field zone interactions (ie.,$z_0 < d_d$). The thickness of the field zone mainly depends on the bias

voltage and doping concentration[*Howes & Morgan*, 1979]. The theoretical depletion depth from the surface of the SCD is obtained by solving the Poisson equation with appropriate boundary conditions and is given by :

$$d_d = \sqrt{\frac{2\epsilon_{Si} V_T}{qN_A}} \tag{4.9}$$

where ϵ_{Si} - the permitivity of silicon, q - charge of an electron, N_A - the acceptor impurity concentration and V_T - the channel potential derived as [*Gow*, 2009]:

$$V_T = V_{AVG} - V_{ss} \tag{4.10}$$

where V_{ss} is the substrate voltage and V_{AVG} is the average driving potential of the pixel obtained by taking the contribution of channel stop, off-electrodes in a pixel to depletion. The charge cloud produced here due to a photon interaction will experience the complete electric field and will drift towards the buried channel. Considering linear regime i.e., drift velocity $\propto$ electric field, radius of the charge cloud (r_d) at the buried channel is computed after drifting through the depletion region using the following equations :

Electric field structure :

$$E(z) = \frac{qN_a}{\epsilon_{Si}} d_d \qquad at \quad z = 0 \tag{4.11}$$

Drift velocity in depletion zone :

$$\upsilon_d = \frac{dz}{dt} = \mu E(z) = \frac{qN_a \mu}{\epsilon_{si}} (d_d - z_0) \tag{4.12}$$

$$t = \int_{z2}^{z1} \frac{dz}{\upsilon_d(z)} = \frac{\epsilon}{\mu q N_a} \; ln \, (\frac{d_d}{d_d - z_0}) \tag{4.13}$$

where μ is the electron mobility which is temperature dependent, we have used

Electron mobility [*Jacoboni et al.*, 1977]:

$$\mu = A_J T^{-\gamma} cm^2 V^{-1} s^{-1} \tag{4.14}$$

where $A_J = 1.43 \times 10^9$, $\gamma = 2.42$ and T is temperature in Kelvin. Due to random thermal motions, the charge cloud undergoes diffusion which increases the size of the cloud. The radius of the charge cloud collected at the buried channel after charge spreading can be obtained by solving time-dependent diffusion equation as given by :

Charge cloud radius in depletion zone [*Hopkinson*, 1987] :

$$r_d = \sqrt{4Dt} = \sqrt{\frac{4KT\epsilon}{q^2 N_a} \; ln\,(\frac{d_d}{d_d - z_0})} \tag{4.15}$$

The electric field structure of SCD CCD54 and CCD236 provides drift velocity which is less than the required mean thermal velocity ($\approx 10^7$ cm/s). Hence, radius of the charge cloud collected at the buried channel arising from interaction in field zone is given as :

$$r = \sqrt{r_i^2 + r_d^2} \tag{4.16}$$

4.7.3 Field-free zone interactions

In epitaxial devices, there is a field-free region between the field zone and the bulk Si substrate (p^+) layer, which does not have an electric field and exhibits a gradient in the doping concentration near to the substrate boundary. Photon interactions in this region $d_d < z_0 < d_d + d_{ff}$ are considered to be field-free zone interactions. The charge cloud produced here will not experience any acceleration but could diffuse and recombine before reaching the buried channel. Diffusion enlarges the size of the charge cloud and could cause spreading of charges across adjacent pixels. It is reasonable to assume that the recombination losses are negligible in this region due to the large carrier life time $\approx 10^{-3}$ s [*Tyagi & van Overstraeten*, 1983]. The general expression for the mean-square radius of a charge cloud reaching the interface between the field and field-free zone in epitaxial devices is given by :

Radius of charge cloud reaching the interface between field and field-free zone *Pavlov & Nousek* [1999] :

$$r_{ff} = \sqrt{2d_{ff}L\left[tanh(\frac{d_{ff}}{L}) - (1 - \frac{z_0 - d_d}{d_{ff}})tanh\left(\frac{d_{ff} - z_0 + d_d}{L}\right)\right]} \tag{4.17}$$

where d_d - depletion depth, d_{ff} - thickness of epitaxial field free zone, L = $\sqrt{D\tau_n}$ - diffusion length; τ_n - charge carrier life time ($\approx 10^{-3}$ sec). It is evident from the above equation that when a photon interacts deeper in the field-free zone, the term ($d_{ff} - z_0 + d_d$) becomes very very small and hence radius (r_{ff}) becomes very large. It is to be noted that the shape of the charge cloud in the field-free zone is non-Gaussian as investigated by [*Pavlov & Nousek*, 1999]. However, we ignore this and presume that they are Gaussian as it affects only a few high energy photon events in the field-free zone. Thus, the final radius of the charge cloud is obtained as quadrature sum of r_i, r_d, r_{ff} :

$$r = \sqrt{r_i^2 + r_d^2 + r_{ff}^2} \tag{4.18}$$

4.7.4 Channel stop interactions

Channel stops occupy considerable amount of area on the SCD CCD-54 ($\approx$ 20%). Photon interactions in channel stops can distort the shape of the observed SRF as it causes horizontal split events. We adopted the same approach followed in simulating the response of CCD in Chandra ACIS detector [*Townsley et al.*, 2002]. Photons interacting in the channel stops (p^+ layer) are assumed to split the resulting charge and are collected from the left and the right sides of the channel stop. The fraction of charges swept towards each side depends on the distance of each side from the location of interaction. Charges propagated from both edges of channel stop are found using [*Townsley et al.*, 2002]:

$$\begin{aligned} Q_{left} &= \tfrac{w_c - x_c}{w_c} Q_0 - \chi x_c + R_N(0)\alpha \tfrac{x_c}{w_c} \\ Q_{right} &= \tfrac{x_c}{w_c} Q_0 - (w_c - x_c)\chi + R_N(0)\alpha \tfrac{w_c - x_c}{w_c} \end{aligned} \tag{4.19}$$

where w_c - width of channel stop, χ - channel stop tuning loss parameter, α - channel stop tuning width parameter. It is also shown from ACIS calibration [*Townsley et al.*, 2002] that the channel stop tuning parameters χ, and α vary with incident photon energy which require precise experimental data on channel stop interactions. For simplicity, in this work we assume energy independence of these parameters.

4.7.5 Charge collection and readout

The amount of charge collected in each pixel (i, j) is obtained by integrating the Gaussian function which is given as *Pavlov & Nousek* [1999] :

$$Q_{ij}(x_0, y_0) = \frac{Q_o}{4} \left\{ \left[\text{erf}\left\{ \frac{a_{i+1}-x_0}{r} \right) - \text{erf}\left(\frac{a_i-x_0}{r} \right) \right] \left[\text{erf}\left(\frac{b_{i+1}-y_0}{r} \right) - \text{erf}\left(\frac{b_i-y_0}{r} \right) \right] \right\} \tag{4.20}$$

where 'r' will be replaced with Eq. (4.16 and 4.18) for interaction in appropriate zones respectively; a, b are pixel dimensions, x_0, y_0 are the event coordinates in the reference frame with its origin at the center of the pixel where the photon is absorbed (-a/2 $< x_0 <$ a/2, -b/2 $< y_0 <$ b/2).

In sec. (4.4) we have seen that the fundamental difference between SCD and 2D CCD, primarily lie in the diagonal clocking and readout. In our simulation, we modeled the *elements* as 2D pixels of equivalent dimensions. Charges collected in each of these equivalent pixels are computed using Eq. (4.20). Further, we incorporate the readout structure by adding the charges collected at different *elements* of each electrode in the SCD. The model hereby provides pseudo linear output for each photon interaction.

4.7.6 Escape peak computation

Photons with incident energy $E_{ph} > 1.839$ keV (ie., binding energy of Si K-atomic shell electrons) have finite probability to yield Si K-α XRF photon of energy 1.75 keV. These XRF photons travel some distance before getting absorbed in the detector. XRF photons emitted from the top few microns of the detector have a large probability to escape without being detected. In such cases, the residual charges collected form the escape peak with energy $E_{esc} = E_{ph}$ - 1.84 keV. In order to simulate the escape peak, we find the number of Si XRF photons produced from an infinitely thick Si medium which are emitted in all possible directions. Directions are assigned using uniform random numbers, where half of the photons coming out of the surface of the detector are considered to yield the escape peak feature.

4.7.7 Simulation implementation

The algorithm explained in Fig. 4.6 is implemented with a set of IDL routines (using the equations from 4.5 to 4.20). Values of some of the important detector parameters used in the model are listed in Table 4.2. Using these values, the depletion depth of the SCD CCD-54 is found to be ≈ 35 μm. Simulations are performed for many variable parameters such as temperature, photon energy, event selection logic and threshold values. A short summary of the implementation, highlighting some important steps is given below :

- Allow photons to impinge on the SCD randomly at normal incidence (ie., 0° with respect to detector normal) and obtain position coordinates (X, Y).
- Tag photons hitting channel stops and pixel regions.
- Simulate physics of photon interaction and charge propagation in field zone, field-free zone and channel stops.
- Charges collected in the *elements* of SCD are clocked diagonally, combined and readout as a linear array output.
- Apply single pixel mode event selection logic with two threshold values.
- Make histogram of the event processed output.

4.8 Simulation results - SRF components

In order to understand the spectral features seen in the observed SRF data, we considered the architecture of CCD-54. We summarize our understanding of different spectral components which are seen in the observed SRF. From our simulation, we identified the sources of origin of SRF components which are summarized in Table 4.3.

TABLE 4.2: Values of parameters used in modeling charge transport of SCD

Parameters	**Values**
Voltage (V_T for d_d computation) [*Gow*, 2009]	3.8 V
Channel stop pitch [*Gow*, 2009]	25 μm
Number of acceptor impurities (N_a) [*Gow*, 2009]	4 $\times 10^{12} cm^{-3}$
Field + Field-free zone thick [*Gow*, 2009]	50 μm
Channel stop width [*Gow*, 2009]	6 μm
Life time (τ) [*Tyagi & van Overstraeten*, 1983]	10^{-3} s
Temperature [*Narendranath*, 2011]	263 K
Number of mono-energetic photons	5 $\times$ 10^4 photons

TABLE 4.3: Identification of SRF components and its origin in the SCD - Simulation results

Interaction zone	SRF component
Channel stop	Soft shoulder, Low-energy tail
Field-free zone	Low-energy rise, Low-energy tail
Field zone	Photopeak, Soft shoulder, Low-energy tail Cutoff, Escape peak

4.8.1 SRF components - Field zone

The dominant photopeak in the SRF mainly arise from field zone interactions, where charges are collected almost completely. Interactions that occur at *'element'* boundaries and at greater depths near to the boundary of field-free zone cause charge splitting across many *'elements'*. These charges are clocked diagonally and added to produce the soft shoulder and low energy tail. Si XRF photons emitted from the top layer of the field zone have a high probability to escape and hence contribute to the escape peak. The SRF components arising due to field zone interactions are shown in Fig. 4.8(a), 4.8(b), 4.9(a) and 4.9(b).

Cutoff is observed at two places in the energy spectrum which are related to the value of threshold 1 (Th1):

- Low energy cutoff - Events below threshold 1 ie., 0.75 keV are discarded

- Soft shoulder cutoff - charges which are split at *element* boundaries lead to configurations with central event discarded (see Fig. 3.1(a)) causing a dip near the soft shoulder. The energy at which dip occurs in the spectrum depends on threshold 1 given by $E_{dip} \approx E_{ph}$ - E_{th1}.

4.8.2 SRF components - Field-free zone

Charge cloud produced due to field-free zone interactions undergoes diffusion causing charge spill over multiple *elements*. As a result, a low energy rising tail component without a photopeak is observed in the pulse height distribution as shown in Fig. 4.8(a), 4.8(b), 4.9(a) and 4.9(b). This component is negligible for low energy x-ray photons as majority of photons get absorbed above field-free zone.

4.8.3 SRF components - Channel stop

Channel stop interactions contribute partly to the soft shoulder component (near to the photopeak) and also to the low-energy tail in the SRF as shown in Fig. 4.8(a), 4.8(b), 4.9(a) and 4.9(b). Also, as mentioned we did not intend to study channel stop tuning parameters in detail in this work.

4.9 Comparison of simulation results with data

We demonstrate the performance of the model by comparing the simulated SRF with the SRF derived from C1XS ground calibration. We summarize below our understanding of different features seen in the SRF. It is clear that all the observed features arise due to interactions at different layers of the detector coupled with the threshold values and event selection logic. An overplot of simulation and calibration data which are normalized to total events is shown in Fig. 4.10(a), 4.10(b), 4.11(a) and 4.11(b). Simulation results predict all features seen in the experimentally derived SRF. High energy x-ray photons penetrate deep inside the detector before interaction, hence more interactions in the

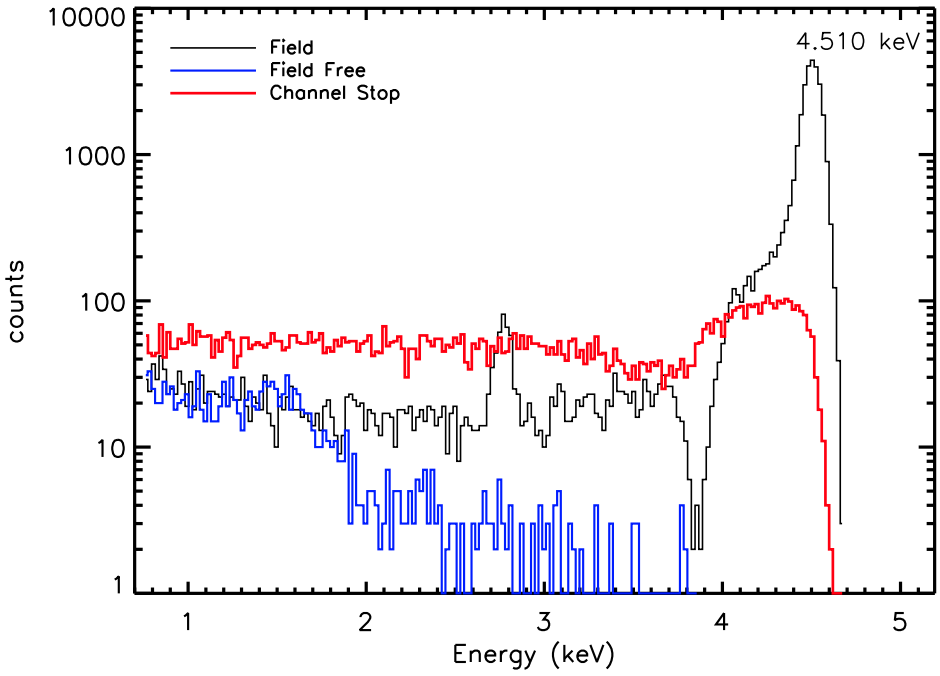

(a)

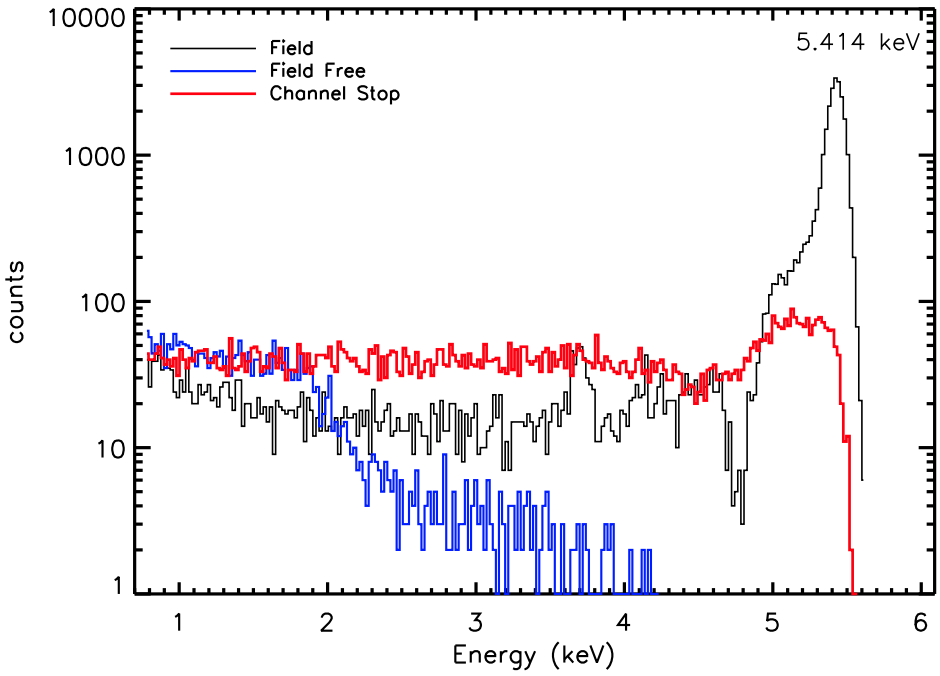

(b)

FIGURE 4.8: Simulation results showing different components of SRF for different mono-energetic photons arising from interactions at different layers of SCD

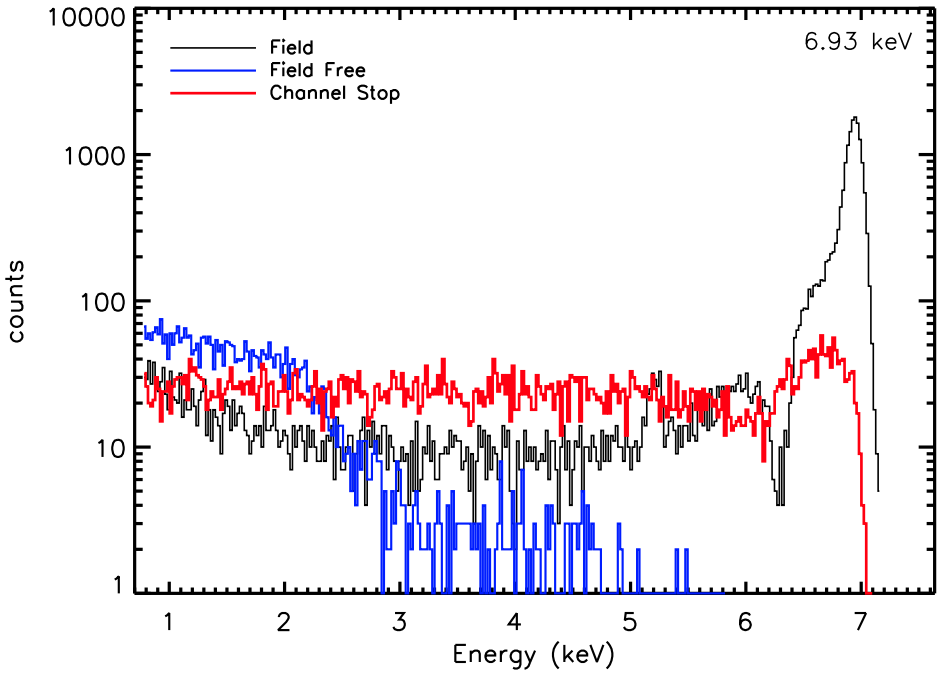

(a)

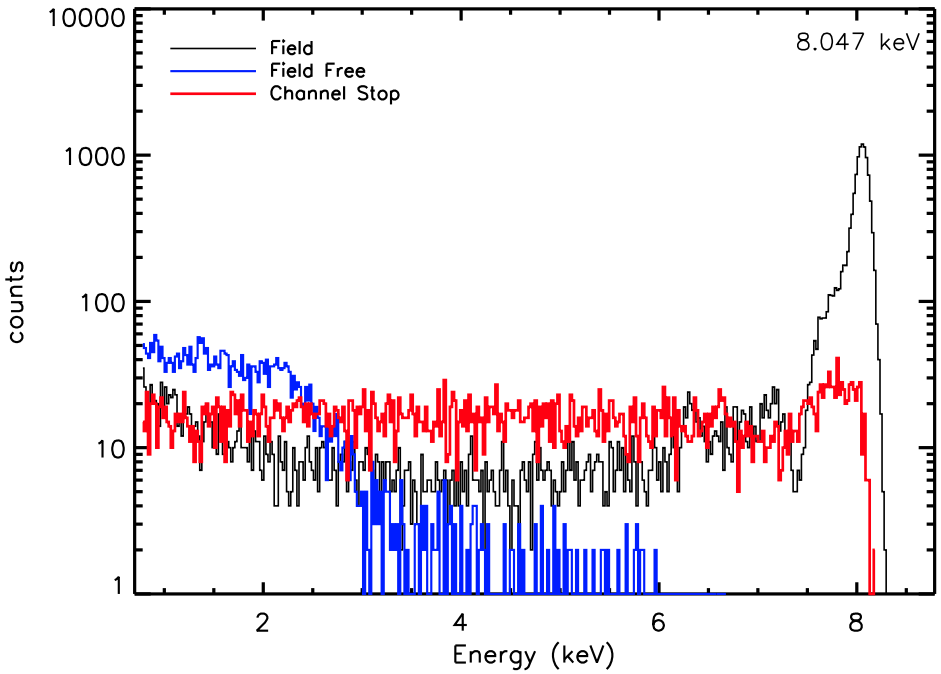

(b)

FIGURE 4.9: Simulation results showing different components of SRF for different mono-energetic photons arising from interactions at different layers of SCD

field-free zone causing more split events. The expected trend of decrease in photopeak and increase in off-peak events with increase in x-ray energies is clearly seen. Variation in the fraction of off-peak events at different energies obtained from calibration data and simulation are plotted in Fig. 4.12. A close match between the two clearly shows that the model represents the calibration data fairly well.

However, at high energies, deviations are observed in the prediction of the soft shoulder and low energy tail components. We attribute this discrepancy to incomplete modeling of energy dependence in the channel stop interactions. However, lunar surface elemental abundances derived from C1XS data discussed in this thesis are not affected by this discrepancy, as the analysis was done using system response derived from actual ground calibration data. Further, study of channel stop tuning parameters and its energy dependence in detail are required for a more precise modeling of the SRF.

4.9.1 Conclusion

We have successfully demonstrated that our model is capable of explaining the spectral redistribution function of epitaxial SCDs. With the available ground calibration data from C1XS we have validated the model and provided physical reasoning for the observed spectral features. However, simulation results show a systematic underestimation of fraction of offpeak events. This discrepancy can be mitigated by including the energy dependence of channel stop tuning parameters which are not studied in detail here. Also, interaction in dead-layer and substrate are considered to be lost which are needed to be included for very low energy and high energy x-ray photons.

4.10 Summary

This chapter described some of the physics of x-ray photon interaction in solid state detectors. Fundamental equations governing the charge generation and propagation necessary for the charge transport model are discussed. With a justification for the need of a charge transport model for the SCD, the chapter focuses on explaining the

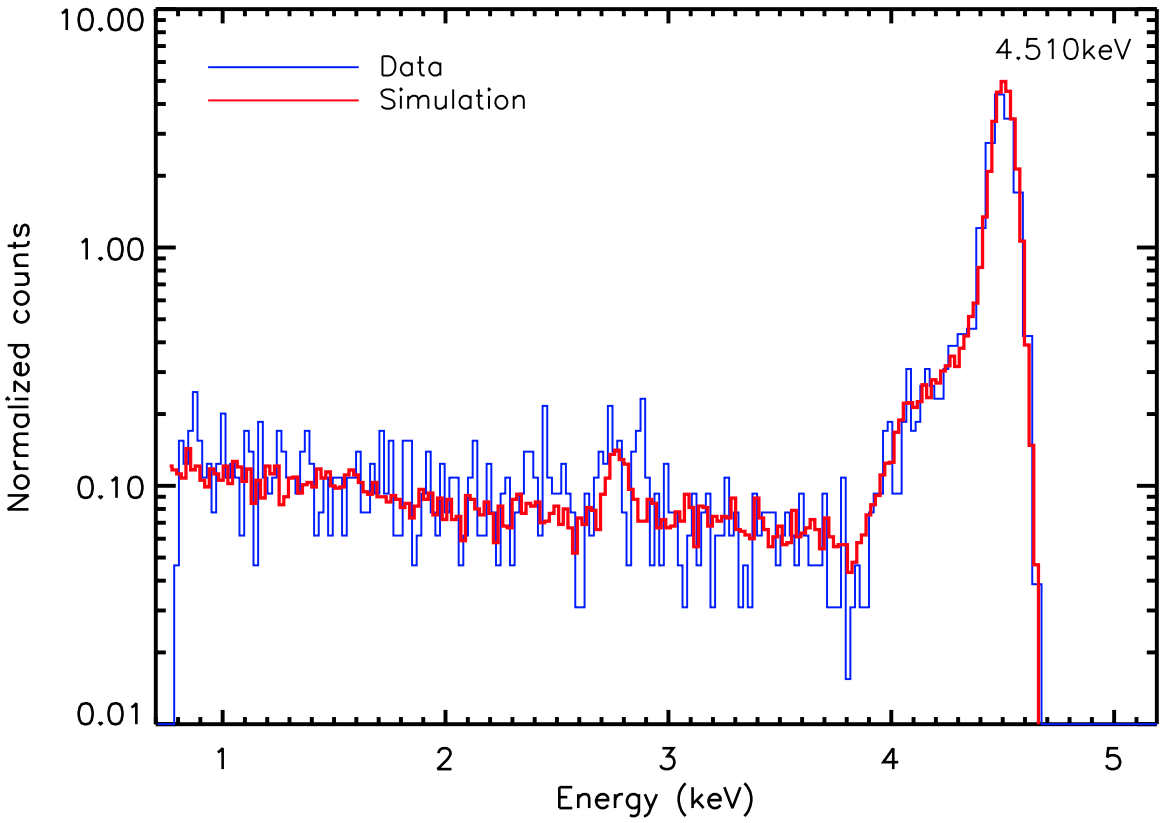

(a)

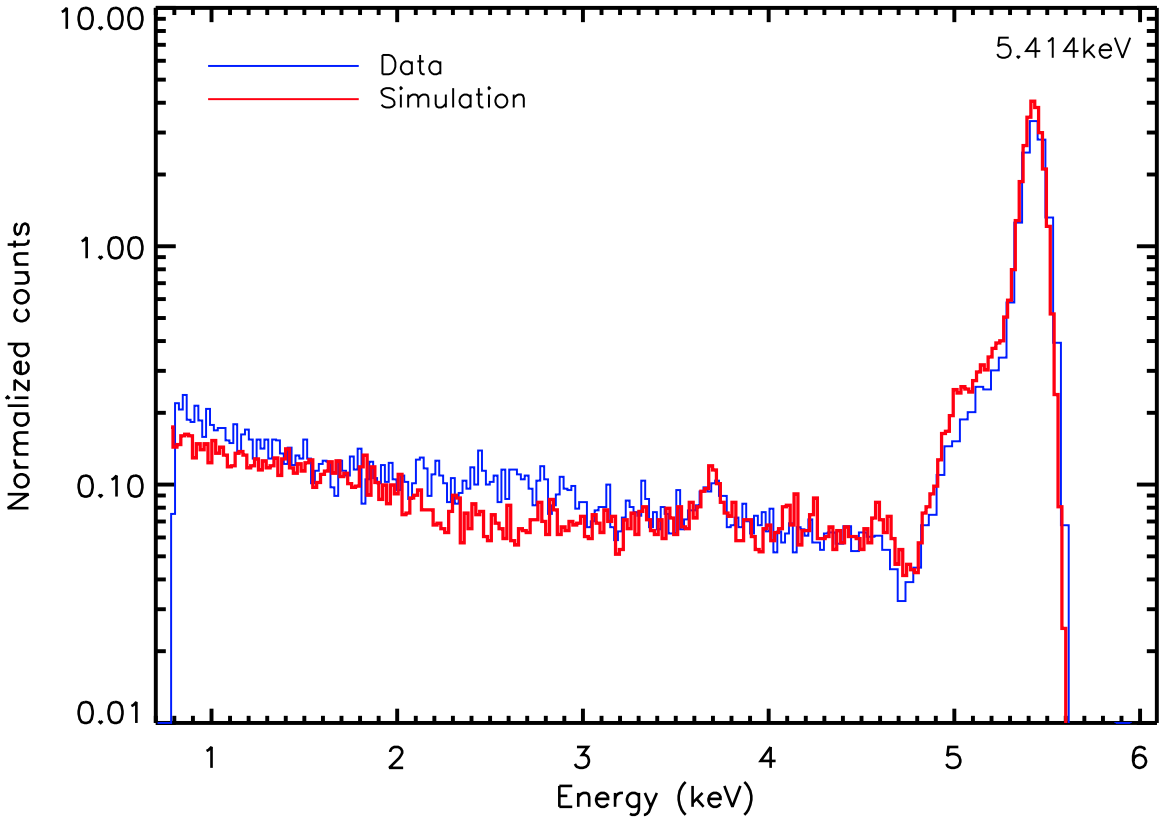

(b)

FIGURE 4.10: Simulation results showing different components of SRF for different mono-energetic photons arising from interactions at different layers of SCD

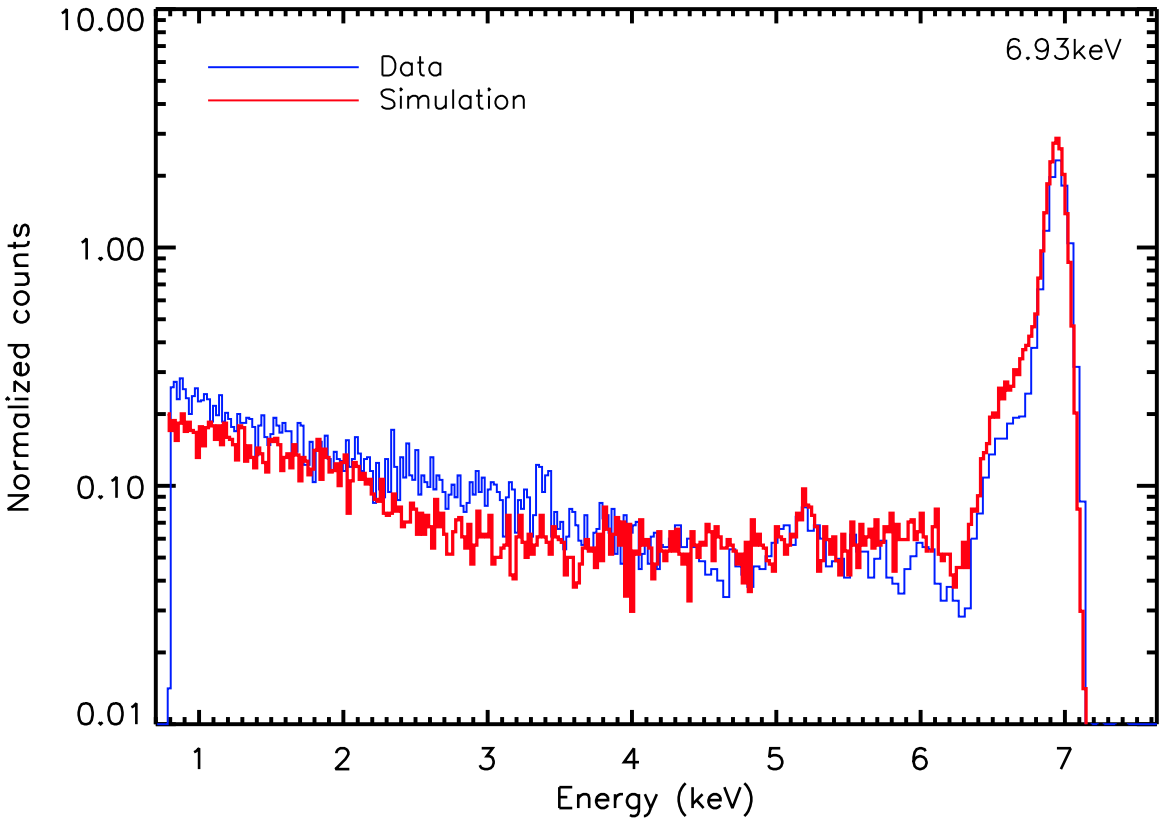

(a)

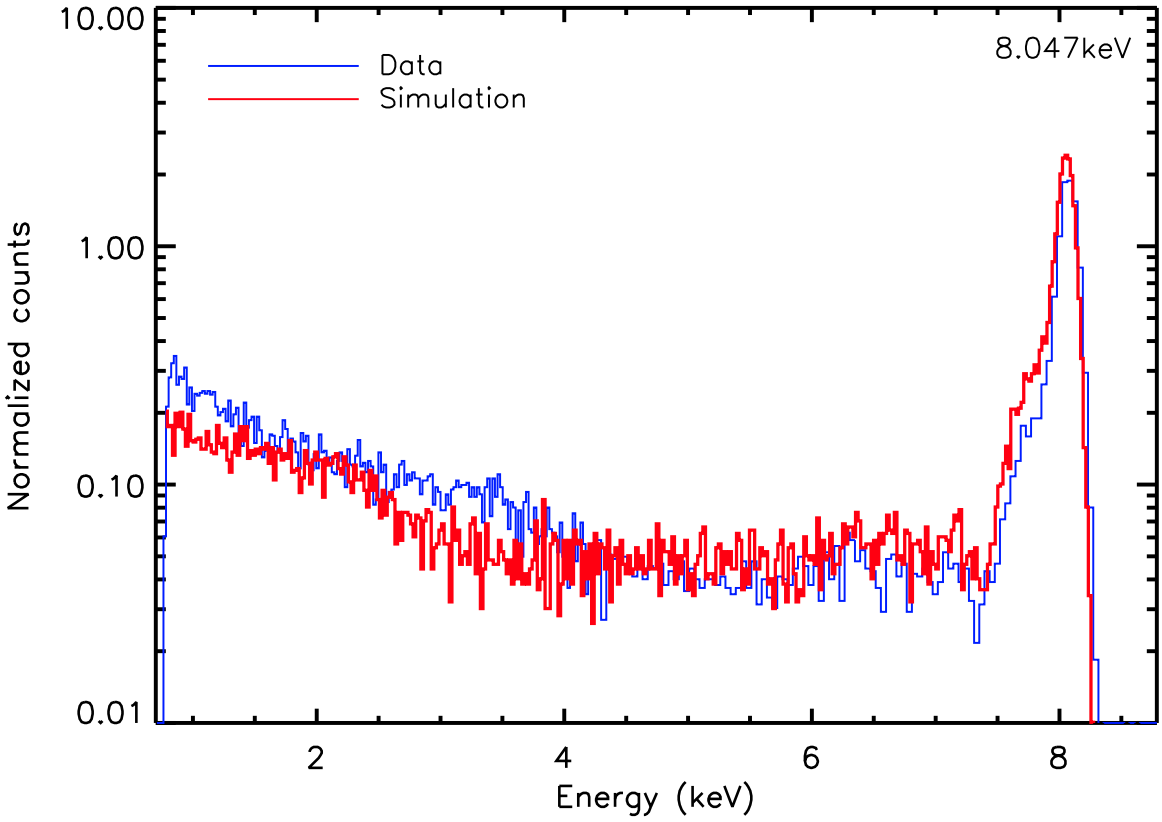

(b)

FIGURE 4.11: Simulation results showing different components of SRF for different mono-energetic photons arising from interactions at different layers of SCD

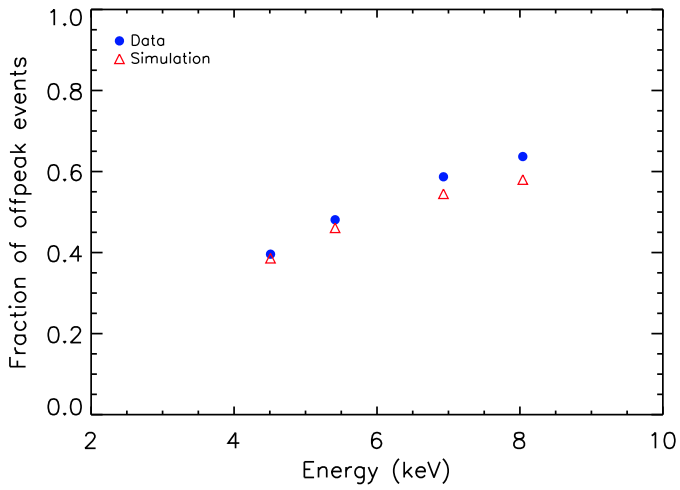

FIGURE 4.12: Fraction of Offpeak events variation with energy of the incident photon. Simulation results well reproduces the trend observed in the calibration. Systematic discrepancy is found with increase in energy which we attribute to incomplete modeling of energy-dependence in channel stop tuning parameters.

algorithm of the model which includes diagonal clocking and readout structure of the SCD. Device level interactions at different detector layers driving the SRF are studied at different energies. Finally, comparison of the simulated SCD CCD54 SRF with the SRF derived from the C1XS ground calibration data and its significance are presented. The next chapter describes the overall thesis summary along with future prospects of lunar surface elemental mapping using x-ray fluorescence technique.

Chapter 5

Thesis summary & Future directions

5.1 Major findings from the thesis work

1. The elemental abundances of Mg, Al, Si and Ca derived from the C1XS experiment agree well within the range of abundances derived from LP GRS. This shows that our new independent approach of deriving elemental abundances from remote sensing XRF experiment, yields abundance values that fall within the large range of values obtained from other remote sensing experiments. This provide validation of the inversion method while enabling new capacity to impose tighter constraints on abundance values. Thus it firmly establishes a refined method to quantitatively address absolute abundance of elements on airless planetary bodies.

2. The XRF inversion algorithm *x2abundance*, developed for the C1XS analysis, can be used for any remote sensing XRF data analysis to derive major elemental abundances ($10 < Z < 31$).

3. The first direct detection of enhanced abundances of Na from certain regions on the Moon suggests a relatively cooler lunar surface evolution than expected. However, more precise elemental maps are required to understand the global evolution of the lunar surface.

4. To answer questions raised by the C1XS experiment and to complete the global elemental mapping, the CLASS experiment is being developed for Chandrayaan-2 mission. A detailed physical model for charge transport in SCD is developed to better understand the spectral response of CLASS devices.

5.1.1 Discovery of enhanced Na and scientific implications

Our understanding of the chemical make up of the Moon, is primarily obtained from geochemical studies of returned lunar samples. These results are further augmented by findings from the analysis of lunar meteorite samples collected from different places. The LMO theory emerged from these studies (explained in chapter 1) which hypothesized that the lunar highland crust was formed as a result of crystallization from a magma ocean in its early past. It further predicts the highland crust to be dominated by plagioclase feldspar mineral. The solutions of plagioclase feldspar mineral can have a range of compositions from calcium-rich end member (anorthite) to sodium-rich end member (albite) as shown in Fig. 5.1). Terrestrial feldspars exhibit Na-rich compositions which differentiates it from the feldspar in our lunar sample collection which are mostly Ca-rich ($>An_{90}$). It is believed that the early Moon underwent loss of volatiles by vaporization due to large amount of thermal energy released during the giant collision. Mineral studies using NIR spectroscopy cannot discern the specific composition of plagioclase. The high Na abundances observed by C1XS are detected only at a very few

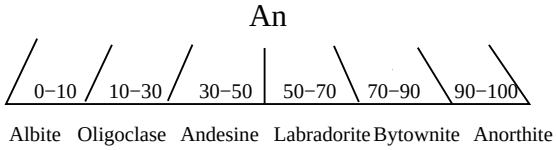

FIGURE 5.1: Plagioclase solutions indicate the sodic and calcic end members along with other intermediate plagioclase minerals which are referred by An#.

places on the lunar surface. Observational and mission limitations have resulted in very poor sampling of the lunar surface for occurrences of high Na abundance. Within the limited flare observations, due to weak flare excitation and inadequate measurements, the observed spectra often did not have Fe and Ti lines to better constrain the derived

abundances and hence left with large uncertainties. If the presence of enhanced Na is considered to be wide-spread then it could well be signature of serial magmatism, an alternative to global magma ocean where the temperatures could be relatively low. If the observation of Na is localized only in certain regions on the Moon, then it can be well considered as an extralunar material as discussed in the following section.

Recent studies on the impact processes via advanced simulations, compositional analysis of lunar meteorites, study of lunar volatiles and remote sensing observations in multiple wavelengths, clearly suggest the need for modifications in the LMO theory. Results from TIR spectroscopy using CF value suggest, indirect evidences of sodic-rich lithologies at different regions on the Moon [*Greenhagen et al.*, 2010; *Kusuma et al.*, 2012]. C1XS results showed the first direct evidence of higher Na abundance in certain regions of the Moon. This significant observation will be studied in detail by the CLASS instrument on Chandrayaan-2.

5.2 Science case for future lunar surface studies

The surface of the Moon is the biggest memory card of our solar system. Due to lack of atmospheric weathering and crustal recycling, it preserves evidence of internal/external events and processes that occurred since the formation of the solar system. It accumulates samples from a wide range of solar system bodies and are constantly bombarded with meteorites of varying sizes. As a result, it create craters, melts soil, form agglutinates, vaporize heated silicates and oxides, sprays melted rock and pulverize the bedrock. Since its formation, it is exposed to highly energetic particles from the solar wind, flare events and cosmic rays which may potentially change the crystal structure and composition. The uppermost regolith layer of the Moon and exposed rocks has the record of all these events and processes. The continuous activity of impacts and processes called ‘gardening’, destroy/overwrites certain older records.

5.2.1 Search for extralunar material on the Moon

It is believed that debris from the inner solar system are cleared on short time scales of a few million years [*Hartmann et al.*, 1999]. However, ever since its formation, the lunar regolith has been gathering external materials. This suggest that material from impacting asteroids from the past is still present on the Moon. So far three extralunar materials were found from Apollo rock and regolith samples [*McSween*, 1976] (Apollo 12 regolith), Haggerty (Apollo 15), [*Jolliff et al.*, 1993] (Apollo 16 regolith). Typically, impacts on the lunar surface occur at relative velocities in a few km/s range leading to excavation of sub-surface material. Thus the search for extralunar materials on the lunar regolith can result in important science returns of inventory of materials collected by the Moon.

The likelihood of capture of terrestrial material by the Moon is higher than other planets due to the proximity to Earth [*Crawford et al.*, 2008]. Finding terrestrial meteoroids on lunar regolith could bring more insights into the conditions of early Earth and pre-biotic chemical evolution on Earth. Prolonged repeated impacts on the lunar regolith reduce the extralunar material into fine micron-scale to sub-mm grain size. Thus relics of older impacts will be very small grains and should be distributed fairly uniformly.

5.2.2 Mapping of moderately volatile elements

The moderately volatile elements viz., Na, K, Cr, Mn are known to be minor elements (ie., < 1 wt%) on the lunar surface. Based on the chemical analysis of lunar samples and meteorites, it is widely understood that the lunar surface is depleted in moderately volatile elements relative to the Earth [*Jones & Palme*, 2000]. However, one of the significant result from C1XS was the measurement of enhanced abundances of Na in certain regions of the Moon. The basis for this observed enhancement is still not clear. Physical processes that could give rise to this enhancement eg., variable thermal cooling of magma or secondary processing of lunar surface remains equivocal. It is also to be mentioned that the measured XRF signal of Na cannot originate from deep layers of

lunar regolith (within a few μm). Hence, the possibility of extralunar materials causing this elevated Na abundances cannot be completely ruled out.

Volatile elements, such as sodium, are expected to be higher in unprocessed bodies (such as comets) which are formed in the outer regions of the protoplanetary disc. This explains the observation of Na tail in comets [*Cremonese et al.*, 1997]. Now, it is well established that sodium lines are omnipresent in meteor spectra. Due to their low excitation potential (2.1eV), Na is released from meteoroids during differential ablation [*Trigo-Rodríguez et al.*, 2004]. It is also observed that cometary meteoroids have enlarged sodium abundances compared to chondritic values [*Trigo-Rodríguez et al.*, 2004; *Trigo-RodríGuez & Llorca*, 2007]. Thus by mapping the abundance of moderately volatile elements on the lunar surface, one can identify and trace the extralunar material on the lunar regolith. In particular, a global map of Na can answer whether the bulk Moon is alkali depleted or not. This can also provide more clues on the diversity of plagioclase on the lunar highlands which is directly related to the thermal evolution of the Moon.

5.3 Design aspects for the development of an x-ray instrument for future lunar surface studies

Combined elemental mapping in x-rays and gamma-rays can help in identifying volatiles/extralunar materials on the lunar surface. For example, the moderately volatile Na can also be measured using gamma-rays, arising from nuclear reactions (say neutron radiative capture and inelastic scattering). The GRS onboard MESSENGER spacecraft demonstrated variation of Na abundances across the surface of Mercury [*Peplowski et al.*, 2014]. However, GRS experiment onboard LP did not observe any significant contribution of Na on the lunar surface [*Prettyman et al.*, 2006]. Thus mapping the compositional differences between the top and deeper layers of lunar regolith can provide more insights on the geophysical/geochemical processes. We consider the following areas where recent technological developments can improve the surface exploration of the Moon in x-rays.

1. Improving the sensitivity of x-ray experiments

2. Global elemental mapping with active x-ray sources - as a long term option

5.3.1 Increasing the instrument sensitivity for a compact planetary payload

Silicon-based x-ray CCDs have lower quantum efficiency (QE) at low energy x-rays ($\leq$ 1 keV), due to the presence of gate structures and dead-layers. It is further limited by entrance windows which are essential to stop stray optical/UV light from reaching the detector. Also careful spectral modeling is required to separate the contribution of scattered solar x-rays which include both soft x-ray lines and continuum at these energies. The following design factors can be considered to improve the sensitivity of the x-ray instrument at low energy x-rays.

5.3.2 Selection of x-ray windows

The response of Si-based CCD extends into optical and near IR wavelengths. As the Moon is very bright in optical wavelengths than at x-rays, the visible light will swamp the detector and yield excessive background which will obscure the x-ray signal. Hence, it is necessary to use suitable filters with high x-ray transmission and high optical/IR extinction. However, proper balancing is required to optimize filter thickness to achieve high optical to x-ray extinction ratio. Here, we provide an order of magnitude estimate for the number of optical photons received by an x-ray CCD orbiting around the Moon. Using this value, we discuss certain design aspects of x-ray window such as material selection and window thickness which are crucial for the transmission of soft x-rays.

5.3.2.1 Estimation of optical photon flux from the Moon

The Moon reflects light from the Sun, which emits black-body radiation corresponding to a temperature of $\approx$ 6000 K. The albedo of the Moon is $\approx$ 13%. The measured spectral irradiance of the Moon at visible/NIR wavelengths (420nm to 1000 nm) [*Cramer et al.*, 2013] clearly shows that it peaks around 600 nm with a value of 2.669 μ W m^{-2}

nm^{-1}. The average flux received on the Earth at visible wavelengths ie., from 400 nm to 750nm, from this observation [*Cramer et al.*, 2013], is given by :

$$< F(\delta\lambda) > \ \ (W/m^{-2}) \ \ = \ \ \sum \frac{dF}{d\lambda} \ d\lambda \ \approx \ 1mWm^{-2} \tag{5.1}$$

Thus the total power radiated by the Moon in this band will be $\approx 10^{14}$ W. The mean wavelength of emission in optical band is determined from :

$$< \lambda > \ \ (nm) \ \ = \ \ \sum \frac{\lambda \ \frac{dF}{d\lambda} \ d\lambda}{\frac{dF}{d\lambda} \ d\lambda} \ \approx \ 600 \ nm \tag{5.2}$$

This implies that, on average, the illuminated lunar hemisphere emits $\approx 10^{32}$ photons/sec at a mean wavelength of $\approx$ 600 nm, as measured from the measured lunar spectral irradiance. For a spacecraft orbiting the Moon at an altitude of 100 km above the lunar surface, the flux reduces as inverse square of distance ($1/r^2$) and hence will experience a flux of $\approx 10^{17}$ photons/sec/cm^2. One important quantity to be estimated is $< N_{ph} >$ which is defined as the average number of visible photons/sample as observed in the detector which is given by :

$$< N_{ph} >= \frac{F(\delta\lambda) \ [photons/sec/cm^2] \times A \ [cm^2] \times t \ [sec] \times \epsilon \ (\delta\lambda)}{Number \ of \ samples \ in \ a \ complete \ readout} \tag{5.3}$$

where $F(\delta\lambda)$ is the flux of photons at visible wavelengths, A is the area of the detector, t is the integration time, $\epsilon(\delta\lambda)$ is the efficiency of detector at visible wavelengths. For devices like CLASS SCD, with an area of 4cm^2 which is readout in 120 samples, integration time of 10^{-5} sec and efficiency $\approx$ 0.5 at 600nm, the average number of visible photons per sample $< N_{ph} >$ will be $\approx 10^{10}$ photons/sample. As a rule of thumb, the noise from stray optical photons should be less than the readout noise of the device per pixel. The readout noise of SCD is $\approx$ 10 e$^-$ rms. For a negligible optical signal we define the criteria to be $\leq$ 10% of the readout noise. Hence, acceptable noise due to interaction of visible photons should be 1 electron/sample.

5.3.2.2 Choice of x-ray window

From the above calculation it is clear that the x-ray window should be opaque at visible wavelengths with a transmission of 10^{-10} or lower. Apart from minimal optical transmission, it should have all the following properties viz., *extremely thin, made of light elements, high tolerance for radiation, high mechanical strength, and light tight*. Also, it should withstand high temperatures, vibrations and impacts.

In general, thin metal foils are opaque for frequencies from radio to middle of UV and transparent for high energy radiations (x-rays and γ-rays). They are highly reflective over the entire range of the visible spectrum. Of the metals, aluminum provides high reflectivity and the best attenuation in optical and near IR region between 400nm to 1000nm [*La Palombara et al.*, 1996; *Owens et al.*, 1994]. It has other advantages such as cost effective, availability, only one small absorption edge at 1.56 keV, thickness can be controlled with high precision. Being a low z element, Al, with low thickness is very transparent at soft x-ray wavelengths. Interaction of optical light with different medium

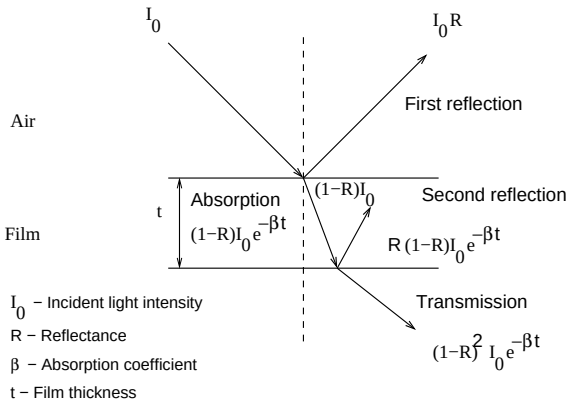

FIGURE 5.2: Transmission and absorption of optical light through a medium of thickness t with absorption coefficient (β). Reflection occurs at boundaries of different refractive indices.

leading to reflection, transmission and absorption is shown in Fig. 5.2. For an incident light beam of intensity I_0, the transmitted intensity through a specimen of thickness t and absorption coefficient β is :

$$I_T = I_0\ (1\ -\ R)^2\ e^{-\beta t} \tag{5.4}$$

where R is the reflectance. Increase in the thickness of film monotonically increases the extinction coefficient (k) which alters the absorption and transmission and hence the reflection. The refractive index (n) decreases smoothly from its initial value which is higher than that of bulk metal to a steady value equivalent to micron thickness [*Heavens*, 1960]. Using the tabulated data of optical constants by *Rakić* [1995], with extinction coefficient k=5.474 at 450nm, we determine the minimum thickness of Al window required to achieve a transmission of $\approx 10^{-10}$ at 300 to 1000nm wavelengths to be more than 0.15 μm. The soft x-ray transmission curve for 0.20 μm thick Al window is shown in Fig. 5.3. Data for soft x-ray transmission curves are obtained from the x-ray database provided by the Centre for X-ray Optics [1]. Usually, x-ray windows are prepared with

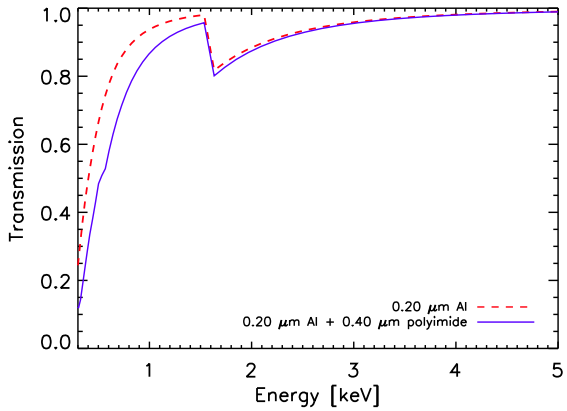

FIGURE 5.3: Transmission of soft x-rays through Al x-ray windows with and without polyimide substrate.

metal-based material deposition onto a polymer-based substrate. The combined structure form free-standing windows. However, complexity increases in handling the fragile, extremely thin, free-standing windows. Also, the additional polymer layer reduces the sensitivity of low energy x-rays as shown in Fig. 5.3. Recent improvements in technology allows direct deposition of Al x-ray filters onto the top of the x-ray detector [*Bautz et al.*, 2014; *Falcone et al.*, 2012]. In this configuration, extra x-ray absorption due to polymer layer(s) can be completely avoided. Significant reduction in the complexity, avoidance of compatibility issues in choosing polymer materials for ultra-high vacuum

[1] http://henke.lbl.gov/optical_constants/filter2.html

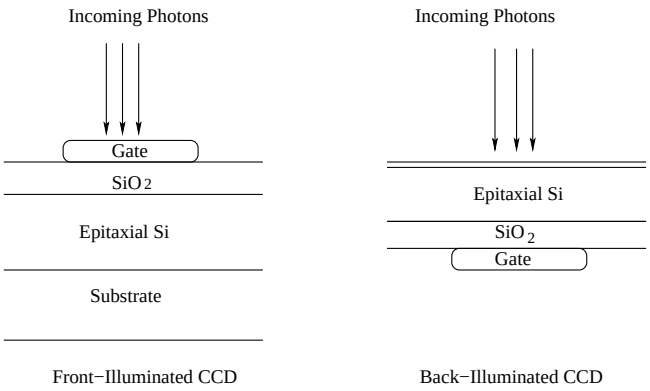

FIGURE 5.4: Representation of FI and BI x-ray CCDs

operations and sensitivity enhancement as much as 10% at 1 keV are the key merits of this configuration.

5.3.3 Improve quantum efficiency of soft x-ray detectors

Despite SCDs offer good spectral resolution with minimal temperature constraints, they have a reduced QE at low energy x-rays as they are front-illuminated (FI) devices. In FI devices, x-ray photons have to penetrate through different dead layers and gate structures before reaching the active volume of the detector. Back-illuminated (BI) CCDs are devices which are flipped with respect to the direction of incoming photons. Schematic representation of FI and BI devices are shown in Fig. 5.4. Further, BI devices are thinned during the process of fabrication and hence will have thickness of tens of microns. In contrast, FI devices have thickness which extends up to a few hundreds of microns. BI CCDs offer high QE at low energy x-rays, as the x-ray photons directly interact with the active volume of the detector without intervention of dead-layers and gate structures. A detailed comparison of QE of different generation of FI and BI x-ray sensors produced by e2V technologies is given in [*Murray et al.*, 2009]. Although BI devices provide higher QE at lower energies, they have a lower QE at energies above 7 keV. Since majority of XRF lines emitted from the lunar surface occur in the energy range from 1 to 7 keV, it can be well measured with BI devices. Thus, we propose a detector system with a suitable combination of BI x-ray CCDs with direct deposition of Al x-ray window of minimum

thickness 0.20 μm. This design can be considered for future lunar surface exploration in x-rays which will reduce the complexity and absorption losses significantly. The sensitivity of the instrument can be enhanced by around $\approx$ 20% at 1 keV in this design. It is also to be noted that the activity of developing a directly deposited Al window on BI thinned devices is under technological development program of NASA Astrophysics Division.

5.4 Lunar XRF using active x-ray source

Remote-sensing study of planetary surface chemistry using XRF technique solely depends on the solar x-ray activity, which has an eleven year periodic cycle. To coordinate lunar XRF observations in tandem with solar flares is difficult due to its unpredictable nature. Also, it takes long duration to complete global elemental mapping during which detector system can degrade/change in performance and response. The C1XS experiment suffered due to an extended solar minimum resulting in only a few solar flare events and lead to very limited utilization.

Next to the Sun, bright celestial x-ray objects (mostly binary compact objects) in our galaxy can be considered as an alternate to perform passive remote-sensing XRF observations. The soft x-ray emission from these sources are due to release of huge thermal energy during the accretion of matter from its companion star. As a result, the binary system undergo different transition phases which produce x-ray flux variations. Some of the known bright x-ray emitting sources in our galaxy are Sco X-1 (in the Scorpius constellation), Cen X-4 (in the Centaurus constellation), Sagittarius A* (at the center of the Milky way). For example, the derived x-ray luminosity of Sco X-1 during a maximum flaring phase is $\approx 10^{31}$ J/s (in 2 to 18 keV band) [*Bradshaw et al.*, 2003]. This translates to an x-ray flux of $\approx 10^{-9}$ W/m^2 which is less than the flux of A-class solar flares (ie., $<$ 10^{-8} W/m^2). To achieve an x-ray flux equal to that of a C-class solar flare, source with fluxes above 10000 crab (where 1 crab = 2.4 $\times$ 10^{-11} W/m^2) are needed. However, none of the known bright x-ray sources can produce such an x-ray flux.

Thus, space missions designed with active x-ray sources can provide an independent way to overcome this dependency. So far the usage of active x-ray sources such as radioactive

sources and x-ray tubes are limited only to make *insitu* measurements on a rover. Global lunar surface studies using active x-ray sources is very challenging and has not yet been attempted. Some of the advantages of active remote-sensing XRF are :

- Uses a controlled input spectrum
- Can better control the accuracy of elemental abundances
- Can complete the task of surface elemental mapping in a relatively short time when system performance can be designed to be stable and well calibrated

An important step towards this is to find the required incident x-ray flux to perform active remote-sensing XRF studies. With simple assumptions, we derive the first order estimates of x-ray flux needed for an active lunar XRF, which is explained in the following section.

5.4.1 Determination of x-ray flux for an onboard active x-ray source

Based on C1XS results, we assume that a minimum x-ray flux equivalent to C-class solar flares (ie., 10^{-7} W/m^2 to 10^{-6} W/m^2 in 1.55 keV to 12.4 keV), is essential to make statistically significant x-ray observations. Conventional x-ray tubes produce bremsstrahlung radiation through acceleration of electrons under a large potential (order of kV) and are allowed to bombard an anode target. At present, portable x-ray tubes can provide an x-ray flux of $\approx 10^6$ - 10^7 photons/sec. Let us assume the spectral distribution of x-ray tube to follow a modified Kramers law as given in [*Tertian & Broll*, 1984]:

$$\frac{dN}{d\lambda} \quad \alpha \quad (\frac{\lambda}{\lambda_0} \; - \; 1)^q \; \frac{1}{\lambda^2} \tag{5.5}$$

where λ is wavelength, λ_0 is short wavelength limit, q is an empirically derived quantity (q=2 is considered here based on [*Boll & de Chateaubourg*, 1999]). For simplicity, we have neglected the self-absorption and window absorption terms in Eq. (5.5) which are exponential terms with respective to mass-absorption coefficients ($\mu_{Z,\lambda}$). The mean

wavelength of this distribution can be estimated from :

$$< \lambda >= \frac{\int \lambda \ \frac{dN}{d\lambda} \ d\lambda}{\int \frac{dN}{d\lambda} \ d\lambda} \tag{5.6}$$

$$\int_{\lambda_{min}}^{\lambda_{max}} \frac{(a\lambda - 1)^2}{\lambda^2} d\lambda = a^2\lambda - 2a\, log(\lambda) - \frac{1}{\lambda} \ ; \ \int_{\lambda_{min}}^{\lambda_{max}} \frac{(a\lambda - 1)^2}{\lambda} d\lambda = \frac{1}{2}\, a\lambda\, (a\lambda{-}4) + log(\lambda)$$

The integration is performed within wavelength limits λ_{min} = 1.55 Å and λ_{max} = 8 Å, which corresponds to the GOES soft x-ray band. After applying appropriate numbers, we obtain the mean wavelength of the spectral distribution of the x-ray tube as 2.30 Å $\approx$ 5 keV. Thus, the average power of the x-ray tube with 10^7 photons/sec will be :

$$< P > \ \approx \ 10^7 \times 5 \times 10^3 \times 1.6 \times 10^{-19} \ \approx \ 10^{-9} \ W \tag{5.7}$$

Now let us assume a configuration with an x-ray tube orbiting around the Moon at an altitude of 100 km from the surface. The x-ray tube is assumed to have a small opening angle of 4° containing the entire power of 10^{-9} W. The incident x-ray beam will illuminate 64 km^2 area on the lunar surface. Thus the soft x-ray flux received by the Moon will be $\approx 10^{-17}$ W/m^2, which is 10^{10} times smaller than our requirement of C-class flare x-ray flux. Thus, to achieve an equivalent C-class flare x-ray flux, the x-ray tube should produce $\approx 10^{17}$ photons/sec. With the available technology of portable x-ray tubes, it is difficult to meet the demand of huge x-ray flux for active lunar XRF studies.

5.4.2 Discussion on other possible x-ray sources for space studies

A brief discussion on the feasibility of other possible x-ray sources that can be considered for active lunar XRF studies is given below :

X-rays from triboluminescence : It has been demonstrated by [*Camara et al.*, 2008, 2010] that x-rays are generated from peeling of pressure sensitive adhesive tapes under reduced pressure conditions through the phenomena of Triboluminescence. It is proposed that while peeling the adhesive bonds are broken and it becomes positively

charged while the polyethylene roll gets negatively charged; as a result huge electric fields ($\approx 10^6$ Vcm^{-1}) build up and give out continuum x-rays during discharge, with peaking flux up to 3×10^5 photons/sec at ≈ 15 keV [*Camara et al.*, 2008]. Although this method of x-ray production is relatively simple and cost effective, it does not provide adequate x-ray flux as required. Also, further studies are needed to understand the dependency of x-ray intensity.

Synchrotron sources : Synchrotron sources essentially consists of particle accelerator (typically electrons) in a powerful guiding magnetic field which are arranged in cyclic structures. In contrast to bremsstrahlung radiation, it can provide a well collimated beam with small angular divergence and very high intensity. Till date, synchrotron sources are the only machines on ground which can generate high intensity x-rays with peaking flux up to 10^{17} - 10^{18} photons/sec, over a wide range of energies. However, the use of synchrotron sources for active lunar XRF is far from realization.

Compact Compton x-ray sources : Compact Compton x-ray source (CCS) is the latest technology, which is a result of extensive research in miniaturizing high intense x-ray production units. CCS rely on the Inverse Compton (IC) effect, which is typically found in accreting compact objects like black hole and magnetized neutron star, to produce high intensity x-rays. The principle of IC is production of high energy photon pulses from collisional scattering of relativistic electrons with low energy photons. One of the important objective of CCS project is to obtain high intensity x-rays from a miniaturized instrument. Various design aspects of CCS using electron gun, particle accelerator and high power laser are discussed in detail in [*Jacquet*, 2014]. At present CCS are aimed to produce 10^{12} - 10^{13} photons/sec with major requirements as a MW high power laser and electron accelerators up to MeV energies, which should be superconducting devices (both electron gun and Linac). With further improvements from the emerging technology available in the neighborhood, we suggest that miniaturized CCS can potentially be considered for future active remote-sensing XRF studies.

5.5 Conclusion

In this chapter we have summarized the findings from this thesis. Science cases for future lunar surface exploration based on C1XS results are discussed in detail. An elaborate description on the possible improvements that can help future x-ray exploration of lunar surface are presented. These suggestive improvements can also be used in the exploration of other airless bodies. Further, we have explored the option of conducting active remote-sensing XRF experiments. Using the derived x-ray flux requirements we discussed the feasibility of a few active x-ray sources. Given the large constraints and unpredictability of passive remote-sensing XRF, active XRF remote-sensing needs to be explored as a future solution. It is further shown that many recent developments in the technological front shows promising results to have an active x-ray source onboard in the orbiter to make global surface studies.

Bibliography

Aarthy R.S., Sanjeevi S. et al. *Spectral Studies of Anorthosite and Meteorite*. In *Lunar and Planetary Science Conference*, *LPSC*, vol. 40, 2216 (2009).

Adler I., Gerard J. et al. *The Apollo 15 X-ray fluorescence experiment*. In *Proceedings of the third Lunar Science Conference*, *Proceedings of the Lunar Science Conference, Proceedings*, vol. 3, 2157 (1972).

Adler I., Trombka J.I. et al. *Apollo 15 and 16 Results of the Integrated Geochemical Experiment*. *Moon*, 7:487, 1973a.

Adler I., Trombka J.I. et al. *Results of the Apollo 15 and 16 X-ray experiment*. In *Lunar and Planetary Science Conference Proceedings*, *Lunar and Planetary Science Conference Proceedings*, vol. 4, 2783 (1973b).

Agostinelli S., Allison J. et al. *GEANT4 - a simulation toolkit*. *Nuclear Instruments & Methods in Physics Research A*, 506:250, 2003.

Alha L., Huovelin J. et al. *Ground calibration of the Chandrayaan-1 X-ray Solar Monitor (XSM)*. *Nuclear Instruments and Methods in Physics Research A*, 607:544, 2009.

Anbazhagan S., Sainaba N.K. et al. *Remote Sensing Study of Sittampundi Anorthosite Complex, India*. *Journal of the Indian Society of Remote Sensing*, 40:145, 2012.

Arnaud K.A. *XSPEC: The First Ten Years*. In George H. Jacoby and Jeannette Barnes, ed., *Astronomical Data Analysis Software and Systems V*, *ASP Conf.*, vol. 101, 10 (1996).

Athiray P.S., Narendranath S. et al. *Validation of methodology to derive elemental abundances from X-ray observations on Chandrayaan-1*. *Planet. & Sp. Sci.*, 75:188, 2013a.

Athiray P.S., Narendranath S. et al. *C1XS results-First measurement of enhanced sodium on the lunar surface*. *Planet. & Sp. Sci.*, 104:279, 2014.

Athiray P.S., Sudhakar M. et al. *Experimental validation of XRF inversion code for Chandrayaan-1*. *Planet. & Sp. Sci.*, 89:183, 2013b.

Ban C., Zheng Y. et al. *Research on the inversion of elemental abundances from change-2 x-ray spectrometry data*. *Chinese Journal of Geochemistry*, 33:289, 2014.

Bautz M.W., Kissel S.E. et al. *Toward Directly-Deposited Optical Blocking Filters for High-performance, Back-illuminated Imaging X-ray Detectors*. In *American Astronomical Society Meeting Abstracts #223, AAS Series*, vol. 223, 344 (2014).

Benz W., Cameron A.G.W. et al. *The origin of the moon and the single impact hypothesis. III*. *Icarus*, 81:113, 1989.

Benz W., Slattery W.L. et al. *The origin of the moon and the single-impact hypothesis. I*. *Icarus*, 66:515, 1986.

Benz W., Slattery W.L. et al. *The origin of the moon and the single-impact hypothesis. II*. *Icarus*, 71:30, 1987.

Bevington P.R. & Robinson K.D. *Data reduction and error analysis for the Physical sciences* (McGraw-Hill, 2003), 3rd ed.

Boll N. & de Chateaubourg P. *Spectral distribution from end window X-ray tubes*. In *Advances in X-ray Analysis, Denver x-ray Conference Series*, vol. 41, 393 (1999).

Bradshaw C.F., Geldzahler B.J. et al. *The X-Ray Spectral Changes of Scorpius X-1*. *Astrophys. J.*, 592:486, 2003.

Camara C.G., Escobar J.V. et al. *Correlation between nanosecond X-ray flashes and stick-slip friction in peeling tape*. *Nature*, 455:1089, 2008.

Camara C.G., Escobar J.V. et al. *Mechanically driven millimeter source of nanosecond X-ray pulses*. *Applied Physics B: Lasers and Optics*, 99:613, 2010.

Cameron A.G.W. & Benz W. *The origin of the moon and the single impact hypothesis. IV*. *Icarus*, 92:204, 1991.

Cameron A.G.W. & Ward W.R. *The Origin of the Moon*. In *Lunar and Planetary Science Conference*, *LPSC*, vol. 7, 120 (1976).

Canup R.M. *Dynamics of Lunar Formation*. , 42:441, 2004a.

Canup R.M. *Simulations of a late lunar-forming impact*. *Icarus*, 168:433, 2004b.

Canup R.M. *Lunar-forming collisions with pre-impact rotation*. *Icarus*, 196:518, 2008.

Canup R.M. *Forming a Moon with an Earth-like Composition via a Giant Impact*. *Science*, 338:1052, 2012.

Canup R.M. *Lunar conspiracies*. *Nature Geosciences*, 504:27, 2013.

Canup R.M. & Asphaug E. *Origin of the Moon in a giant impact near the end of the Earth's formation*. *Nature*, 412:708, 2001.

Clark P.E. *Correction, correlation, and theoretical consideration of lunar X-ray fluorescence intensity ratios*. Ph.D. thesis, Maryland Univ., College Park., 1979.

Colaprete A., Elphic R.C. et al. *Overview of the LADEE Ultraviolet-Visible Spectrometer: Design, Operations, and Initial Results*. In *Lunar and Planetary Science Conference*, *LPSC*, vol. 45, 2566 (2014).

Cramer C.E., Lykke K.R. et al. *Precise Measurement of Lunar Spectral Irradiance at Visible Wavelengths*. *Journal of Research of the National Institute of Standards and Technology*, 118:396, 2013.

Crawford I.A., Baldwin E.C. et al. *On the Survivability and Detectability of Terrestrial Meteorites on the Moon*. *Astrobiology*, 8:242, 2008.

Cremonese G., Boehnhardt H. et al. *Neutral Sodium from Comet Hale-Bopp: A Third Type of Tail*. *Astrophys. J. Lett.*, 490:L199, 1997.

Criss J.W. & Birks L.S. *Calculation methods for fluorescent X-ray Spectrometry: Empirical coefficients vs fundamental parameters*. *Anal. Chem.*, 40:1080, 1968.

Ćuk M. & Stewart S.T. *Making the Moon from a Fast-Spinning Earth: A Giant Impact Followed by Resonant Despinning*. *Science*, 338:1047, 2012.

Demidova S.I., Nazarov M.A. et al. *Chemical composition of lunar meteorites and the lunar crust*. *Petrology*, 15:386, 2007.

Dere K.P., Landi E. et al. *CHIANTI - an atomic database for emission lines*. *Astron. Astrophys. Suppl.*, 125:149, 1997.

Donaldson Hanna K.L., Cheek L.C. et al. *Global assessment of pure crystalline plagioclase across the Moon and implications for the evolution of the primary crust*. *Journal of Geophysical Research (Planets)*, 119:1516, 2014.

Donaldson Hanna K.L., Thomas I.R. et al. *Laboratory emissivity measurements of the plagioclase solid solution series under varying environmental conditions*. *Journal of Geophysical Research (Planets)*, 117:E11004, 2012.

Elkins-Tanton L. *The Earth and the Moon*. The Solar System Series (Infobase Publishing, 2006). ISBN 9781438107271.

Falcone A.D., Prieskorn Z. et al. *Recent progress on developments and characterization of hybrid CMOS x-ray detectors*. In *SPIE Conference Series*, vol. 8453, 84530E (2012).

Fano U. *Ionization Yield of Radiations. II. The Fluctuations of the Number of Ions*. *Physical Review*, 72:26, 1947.

Feldman W.C., Maurice S. et al. *Fluxes of Fast and Epithermal Neutrons from Lunar Prospector: Evidence for Water Ice at the Lunar Poles*. *Science*, 281:1496, 1998.

Fernndez J.E. *Rayleigh and compton scattering contributions to x-ray fluorescence intensity*. *X-Ray Spectrometry*, 21:57, 1992.

Fitoussi C. & Bourdon B. *Silicon Isotope Evidence Against an Enstatite Chondrite Earth*. *Science*, 335:1477, 2012.

Franchi I.A., Wright I.P. et al. *The oxygen-isotopic composition of Earth and Mars*. *Meteoritics & Planetary Science*, 34:657, 1999.

Gow J. *Radiation Damage Analysis of the Swept Charge Device for the C1XS Instrument*. Ph.D. thesis, Brunel Univ., UK., 2009.

Grande M., Browning R. et al. *The D-CIXS X-ray mapping spectrometer on SMART-1*. *Planet. & Sp. Sci.*, 51:427, 2003.

Grande M., Maddison B.J. et al. *The C1XS X-ray Spectrometer on Chandrayaan-1*. *Planet. & Sp. Sci.*, 57:717, 2009.

Greenhagen B.T., Lucey P.G. et al. *Global Silicate Mineralogy of the Moon from the Diviner Lunar Radiometer*. *Science*, 329:1507, 2010.

Hall D., Holland A. et al. *Simulating and reproducing instrument background for x-ray CCD spectrometers in space*. In *SPIE Conference Series*, vol. 7021, 70211Y (2008).

Hartmann W.K. & Davis D.R. *Satellite-sized planetesimals and lunar origin*. *Icarus*, 24:504, 1975.

Hartmann W.K., Farinella P. et al. *Reviewing the Yarkovsky effect: New light on the delivery of stone and iron meteorites from the asteroid belt*. *Meteoritics and Planetary Science*, 34:161, 1999.

Haskin L. & Warren P. *Lunar chemistry*. In G.H. Heiken, D.T. Vaniman & B.M. French, eds., *Lunar sourcebook - A user's guide to the moon* (1991).

Heavens O.S. *Optical properties of thin films*. *Reports on Progress in Physics*, 23:1, 1960.

Herwartz D., Pack A. et al. *Identification of the giant impactor Theia in lunar rocks*. *Science*, 344:1146, 2014.

Hopkinson G.R. *Analytic modeling of charge diffusion in charge-coupled-device imagers*. *Optical Engineering*, 26:766, 1987.

Howe C.J., Drummond D. et al. *Chandrayaan-1 X-ray Spectrometer (C1XS) - Instrument design and technical details*. *Planet. & Sp. Sci.*, 57:735, 2009.

Howes M.J. & Morgan D.V. *Charge-coupled devices and systems* (Chichester, Sussex, England and New York, Wiley-Interscience, 1979).

Jacoboni C., Canali C. et al. *A review of some charge transport properties of silicon*. *Solid State Electronics*, 20:77, 1977.

Jacquet M. *High intensity compact Compton X-ray sources: Challenges and potential of applications*. *Nuclear Instruments and Methods in Physics Research B*, 331:1, 2014.

Jaumann R., Hiesinger H. et al. *Geology, geochemistry, and geophysics of the Moon: Status of current understanding*. *Planet. & Sp. Sci.*, 74:15, 2012.

Jenkins R., Gould R.W. et al. *Quantitative X-ray Spectrometry* (M. Dekker, New york, 1995), 2nd ed.

Jolliff B.L., Korotev R.L. et al. *An iridium-rich iron micrometeorite with silicate inclusions from the Moon*. In *Lunar and Planetary Science Conference*, *Lunar and Planetary Inst. Technical Report*, vol. 24, 729 (1993).

Jones J.H. & Palme H. *Geochemical Constraints on the Origin of the Earth and Moon*. In R.M. Canup, K. Righter & et al., eds., *Origin of the Earth and Moon*, 197 (2000).

Korotev R.L., Jolliff B.L. et al. *Feldspathic lunar meteorites and their implications for compositional remote sensing of the lunar surface and the composition of the lunar crust*. *Geochemica Acta*, 67:4895, 2003.

Kramers H.A. *On the theory of X-ray absorption and of the continuous X-ray spectrum*. *Philosophical Magazine*, 46:836, 1923.

Kurniawan O. & Ong V.K.S. *Investigation of Range-energy Relationships for Low-energy Electron Beams in Silicon and Gallium Nitride*. *Scanning*, 29:280, 2007.

Kusuma K.N., Sebastian N. et al. *Geochemical and mineralogical analysis of Gruithuisen region on Moon using M3 and DIVINER images*. *Planet. & Sp. Sci.*, 67:46, 2012.

La Palombara N., Musso C. et al. *The Filters for EPIC: Optimized Design*. *Astrophys. Space Sci.*, 239:281, 1996.

Landi E., Del Zanna G. et al. *CHIANTI-An Atomic Database for Emission Lines. VII. New Data for X-Rays and Other Improvements*. *Astrophys. J.*, 162:261, 2006.

Lawrence D.J., Feldman W.C. et al. *Global Elemental Maps of the Moon: The Lunar Prospector Gamma-Ray Spectrometer*. *Science*, 281:1484, 1998.

Lawrence D.J., Feldman W.C. et al. *Iron abundances on the lunar surface as measured by the Lunar Prospector gamma-ray and neutron spectrometers*. *Journal of Geophysical Research (Planets)*, 107:5130, 2002.

Lodders K. & Fegley B. *Chemistry of the Solar System* (Ingram Pub Services, 2011). ISBN 9780854041282.

Longstaff A. *Astrobiology: An Introduction*. Series in Astronomy and Astrophysics (CRC Press, 2014). ISBN 9781498728454.

Lowe B.G., Holland A.D. et al. *The swept charge device, a novel CCD-based EDX detector: first results*. *Nuclear Instruments & Methods in Physics Research A*, 458:568, 2001.

Lucey P.G. *Mineral maps of the Moon*. *Geophysical Res. Letters*, 31:L08701, 2004.

Lugmair G. & Shukolyukov A. *Early solar system timescales according to 53mn-53cr systematics*. *Geochimica et Cosmochimica Acta*, 62:2863, 1998.

Markowicz A.A. *X-ray physics*. In Grieken, R. V. and Markowicz, A., ed., *Handbook of X-ray Spectroscopy* (M. Dekker, New york, 2002), 2nd ed.

Maruyama Y., Ogawa K. et al. *Laboratory experiments of particle size effect in X-ray fluorescence and implications to remote X-ray spectrometry of lunar regolith surface*. *Earth Planets & Space*, 60:293, 2008.

McKay D.S., G. Heiken et al. *Lunar regolith*. In G.H. Heiken, D.T. Vaniman & B.M. French, eds., *Lunar sourcebook - A user's guide to the moon* (1991).

McSween Jr. H.Y. *A new type of chondritic meteorite found in lunar soil*. *Earth and Planetary Science Letters*, 31:193, 1976.

Melosh H.J. & Kipp M.E. *Giant Impact Theory of the Moon's Origin: First 3-D Hydrocode Results*. In *Lunar and Planetary Science Conference*, *Lunar and Planetary Science Conference*, vol. 20, 685 (1989).

Metzger A.E. *Composition of the Moon as determined from orbit by gamma-ray spectroscopy*. In C. M. Pieters and P. A. J. Englert, ed., *Remote Geochemical Analysis: Elemental and Mineralogical Composition* (Cambridge Univ. Press, 1993).

Murray N.J., Holland A.D. et al. *The X-ray quantum efficiency measurement of high resistivity CCDs*. *Nuclear Instruments and Methods in Physics Research A*, 604:180, 2009.

Näränen J., Parviainen H. et al. *Laboratory studies into the effect of regolith on planetary X-ray fluorescence spectroscopy*. *Icarus*, 198:408, 2008.

Narendranath S. *X-ray studies of the Moon*. Ph.D. thesis, Univ., of Calicut, Kerala, India., 2011.

Narendranath S., Athiray P.S. et al. *Lunar X-ray fluorescence observations by the Chandrayaan-1 X-ray Spectrometer (C1XS): Results from the nearside southern highlands*. *Icarus*, 214:53, 2011.

Narendranath S., Sreekumar P. et al. *Calibration of the C1XS instrument on Chandrayaan-1*. *Nuclear Instruments and Methods in Physics Research A*, 621:344, 2010.

Nekvasil H., Coraor A.E. et al. *Alkali Depletion of the Bulk Moon, is it Required?* In *Lunar and Planetary Science Conference*, *LPSC*, vol. 44, 2830 (2013).

Nittler L.R., Starr R.D. et al. *X-ray fluorescence measurements of the surface elemental composition of asteroid 433 Eros*. *Meteoritics and Planetary Science*, 36:1673, 2001.

Nozette S., Lichtenberg C.L. et al. *The Clementine Bistatic Radar Experiment*. *Science*, 274:1495, 1996.

Ohtake M., Matsunaga T. et al. *The global distribution of pure anorthosite on the Moon*. *Nature*, 461:236, 2009.

Okada T., Shiraishi H. et al. *X-Ray Fluorescence Spectrometer (XRS) on Kaguya: Current Status and Results*. In *Lunar and Planetary Science Conference*, *LPSC*, vol. 40, 1897 (2009).

Owens A., Fraser G.W. et al. *On the experimental determination of the Fano factor in Si at soft X-ray wavelengths*. *Nuclear Instruments and Methods in Physics Research A*, 491:437, 2002.

Owens A., McCarthy K.J. et al. *Designing thin-film optical filters for soft x-ray astronomical telescopes*. In R.B. Hoover & A.B. Walker, eds., *Multilayer and Grazing Incidence X-Ray/EUV Optics II, SPIE Conference Series*, vol. 2011, 438 (1994).

Pack A. & Herwartz D. *The triple oxygen isotope composition of the Earth mantle and understanding $\Delta O17$ variations in terrestrial rocks and minerals*. *Earth & Planetary Science Letters*, 294:345, 2014.

Pahlevan K. & Stevenson D.J. *Equilibration in the aftermath of the lunar-forming giant impact*. *Earth & Planetary Science Letters*, 262:438, 2007.

Pavlov G.G. & Nousek J.A. *Charge diffusion in CCD X-ray detectors*. *Nuclear Instruments and Methods in Physics Research A*, 428:348, 1999.

Peplowski P.N., Evans L.G. et al. *Enhanced sodium abundance in Mercury's north polar region revealed by the MESSENGER Gamma-Ray Spectrometer*. *Icarus*, 228:86, 2014.

Pieters C.M. *Lunar materials from the visible to mid-infrared : The effects of space weathering*. In Lawrence A. Taylor, Gregory A. Snyder, Clive R. Neal, W. Gary Ernst, ed., *Planetary Petrology and Geochemistry: The Lawrence A. Taylor 60th Birthday volume* (Bellwether Publishing Ltd.,, Geological Society of America, 1999).

Pieters C.M., Besse S. et al. *Mg-spinel lithology: A new rock type on the lunar farside*. *Journal of Geophysical Research (Planets)*, 116:E00G08, 2011.

Pieters C.M., Goswami J.N. et al. *Character and Spatial Distribution of OH/H_2O on the Surface of the Moon Seen by M^3 on Chandrayaan-1*. *Science*, 326:568, 2009.

Prakash A. *Magnetospheric protons and electrons encountered by the moon in the plasma sheet*. *Moon*, 14:71, 1975.

Press W.H., P. F.B. et al. *Numerical recipes in C: The art of Scientific computing* (Cambridge University Press, 1988), 1st ed.

Prettyman T.H., Hagerty J.J. et al. *Elemental composition of the lunar surface: Analysis of gamma ray spectroscopy data from Lunar Prospector*. *Journal of Geophysical Research (Planets)*, 111:E12007, 2006.

Rakić A.D. *Algorithm for the determination of intrinsic optical constants of metal films: application to aluminum*. *Applied Optics*, 34:4755, 1995.

Ray C.S., Reis S.T. et al. *JSC-1A lunar soil simulant: Characterization, glass formation, and selected glass properties*. *Journal of Non Crystalline Solids*, 356:2369, 2010.

Rousseau M. & Boivin J. *The fundamental algorithm: A natural extension of the Sherman equation*. *The Rigaku*, 15:13, 1998.

Sherman J. *The theoretical derivation of fluorescent X-ray intensities from mixtures*. *Spectrochimica Acta*, 7:283, 1955.

Shirai K., Okada T. et al. *Instrumentation and performance evaluation of the XRS on SELENE orbiter*. *Earth, Planets, and Space*, 60:277, 2008.

Shiraiwa T. & Fujino N. *Theoretical Calculation of Fluorescent X-Ray Intensities in Fluorescent X-Ray Spectrochemical Analysis.* *Japanese Journal of Applied Physics*, 5:886, 1966.

Shiraiwa T. & Fujino N. *Theoretical Calculation of Fluorescent X-Ray Intensities of Nickel-Iron-Chromium Ternary Alloys*. *Bulletin of the Chemical Society of Japan*, 40:2289, 1967.

SMART-1 Team, Swinyard B.M. et al. *X-ray fluorescence observations of the moon by SMART-1/D-CIXS and the first detection of Ti Kα from the lunar surface*. *Planet. & Sp. Sci.*, 57:744, 2009.

Starr R.D., Schriver D. et al. *MESSENGER detection of electron-induced X-ray fluorescence from Mercury's surface*. *Journal of Geophysical Research (Planets)*, 117:E00L02, 2012.

Swinyard B., Kellett B. et al. *C1XS Spectral Analysis Method*. In *Workshop X-ray Fluorescence Spectroscopy in Planetary Remote Sensing*, *ESA Special Publication*, vol. 687, 5 (2010).

Taylor S.R. *Planetary science: A lunar perspective* (Lunar and Planetary Institute, Houston, TX, 1982).

Tertian R. & Broll N. *Spectral intensity distributions from x-ray tubes. Calculated versus experimental evaluations*. *X-Ray Spectrometry*, 13:134, 1984.

Touboul M., Kleine T. et al. *Late formation and prolonged differentiation of the Moon inferred from W isotopes in lunar metals*. *Nature*, 450:1206, 2007.

Townsley L.K., Broos P.S. et al. *Simulating CCDs for the Chandra Advanced CCD Imaging Spectrometer*. *Nuclear Instruments and Methods in Physics Research A*, 486:716, 2002.

Trigo-RodríGuez J.M. & Llorca J. *On the sodium overabundance in cometary meteoroids*. *Advances in Space Research*, 39:517, 2007.

Trigo-Rodríguez J.M., Llorca J. et al. *Chemical abundances determined from meteor spectra - II. Evidence for enlarged sodium abundances in meteoroids*. *Mon. Not. Roy. Astron. Soc.*, 348:802, 2004.

Tyagi M.S. & van Overstraeten R. *Minority carrier recombination in heavily-doped silicon*. *Solid State Electronics*, 26:577, 1983.

Warren P.H. *The magma ocean concept and lunar evolution*. *Annual Review of Earth & Planetary Sciences*, 13:201, 1985.

Weider S.Z., Kellett B.J. et al. *The Chandrayaan-1 X-ray Spectrometer: First results*. *Planet. & Sp. Sci.*, 60:217, 2012.

Wiechert U., Halliday A.N. et al. *Oxygen Isotopes and the Moon-Forming Giant Impact*. *Science*, 294:345, 2001.

Wood J.A. *Moon over Mauna Loa - A review of hypotheses of formation of earth's moon*. In W.K. Hartmann, R.J. Phillips & G.J. Taylor, eds., *Origin of the Moon*, 17 (1986).

Yamashita N., Gasnault O. et al. *The global distribution of calcium on the Moon: Implications for high-Ca pyroxene in the eastern mare region*. *Earth & Planetary Science Letters*, 353:93, 2012.

Yamashita N., Hasebe N. et al. *Complexities of gamma-ray line intensities from the lunar surface*. *Earth, Planets, and Space*, 60:313, 2008.

Zhang liyan N., Gasnault O. et al. *Background deduction of the Chang'E-1 gamma-ray spectrometer*. *Chinese J. Geochem.Earth & Planetary Science Letters*, 31:234, 2012.

List of Publications

Peer Reviewed Journals - Published work

- C1XS results - First measurement of enhanced Sodium on the Lunar surface - **P.S. Athiray**, S. Narendranath, P. Sreekumar, M. Grande; *2014, Planetary & Space Science, 104, 279*

- Experimental validation of XRF inversion code for Chandrayaan-1
  -**P.S. Athiray**, M. Sudhakar, M.K. Tiwari, S. Narendranath, G.S. Lodha, S.K. Deb, P. Sreekumar, S.K. Dash ; *2013, Planetary & Space Science, 89, 183*

- Validation of methodology to derive elemental abundances from X-ray observations on Chandrayaan-1
  -**P.S. Athiray**, S. Narendranath, P. Sreekumar, S.K. Dash, B.R.S. Babu ; *2013, Planetary & Space Science, 75, 188*

- Lunar X-ray fluorescence observations by the Chandrayaan-1 X-ray Spectrometer (C1XS): Results from the nearside southern highlands
  -S. Narendranath, **P.S. Athiray**, P. Sreekumar, B.J. Kellett, L. Alha, C.J. Howe, K.H. Joy, M. Grande, J. Huovelin, I.A. Crawford and the C1XS team ; *2011, Icarus, 214, 53*

- Mapping lunar surface chemistry: new prospects with the Chandrayaan-2 Large Area Soft x-ray Spectrometer (CLASS)
  -S. Narendranath, **P.S. Athiray**, P. Sreekumar, V. Radhakrishna and the CLASS team ; *2013, Arxiv, 1305.6218*

- Elemental Abundances in the Solar Corona as Measured by the X-ray Solar Monitor Onboard Chandrayaan-1
  -S. Narendranath, P. Sreekumar, L. Alha, K. Sankarasubramanian, J. Huovelin, **P.S. Athiray** ; *2014, Solar Physics, 289, 1585*

- The Chandrayaan-1 X-ray Spectrometer: First results
  - S.Z. Weider, B.J. Kellett, B.M. Swinyard, I.A. Crawford, K.H. Joy, M. Grande,

C.J. Howe, J. Huovelin, S. Narendranath, L. Alha, M. Anand, **P.S. Athiray**, N. Bhandari, J.A. Carter, A.C. Cook and the C1XS team ; *2012, Planetary & Space Science, 60, 217*

International Conference Proceedings

- Direct Evidence of Enhanced Sodium Content on the Moon Around Tycho Region: C1XS Observations
  - **P.S. Athiray**, K. N. Kusuma, S. Narendranath, P. Sreekumar
  2014, Proceedings, 45th Lunar and Planetary Science Conference, 1777, p.1857

- Observations of the Geotail While in Lunar Orbit by the Chandrayaan-1 X-Ray Spectrometer(C1XS)
  - S. Narendranath, S. Tadeppalli, **P. S. Athiray**, A. Misra, P. Sreekumar
  2014, Proceedings, 45th Lunar and Planetary Science Conference, 1777, p.2199

- Lunar X-Ray Fluorescence (XRF) observations with C1XS during weak solar flares
  - **P.S. Athiray**, S. Narendranath, P. Sreekumar
  2013, Proceedings, ASI Conf. Series, 9, p.108

- Modeling charge transport in swept charge devices for x-ray spectroscopy
  - **P.S. Athiray**, S. Narendranath, P. Sreekumar, J. Gow, V. Radhakrishna, B. R. S. Babu
  2012, Proceedings, SPIE Conf. Series, 8453, p.84532L

- The Chandrayaan-2 Large Area Soft X-Ray Spectrometer (CLASS)
  - V. Radhakrishna, S. Narendranath,A. Tyagi, M. Bug, U. Unnikrishnan, R. Kulkarni, C. V. Sreekantha, Kumar, G. Balaji, **P. S. Athiray**, M. Sudhakar, C. V. Chetty, M. R. Thyagaraj, C. Howe, J. Gow, P. Sreekumar
  2011, Proceedings, 42nd Lunar and Planetary Science Conference, 1608, p.1708

- Charged particle detection using swept charge devices
  - U. Unnikrishnan, M. Sudhakar, A. Tyagi, M. Bug, V. Radhakrishna, **P. S. Athiray**,
  2011, Proceedings, ASI Conf. Series, 3, p.163